Study of Electronic Properties of 122 Iron Pnictide through Structural, Carrier-doping, and Impurity-scattering Effects

Tatsuya Kobayashi

January 30, 2016

Contents

List of Figures

List of Tables

Part I

Introduction

1.1 Iron-based superconductor (FeSC)

Iron-based superconductor (FeSC) is a new family of high-temperature superconductor discovered in 2008 [1]. The maximum superconducting transition temperature T_c reaches 55 K in SmFeAs(O,F) of a bulk crystal [2] and above 65 K in FeSe thin film [3]. These T_c values are the records of the transition temperature after cuprate superconductors discovered in 1986 [4]. FeSC attracts attention not only in term of certain applications due to its T_c and relatively high H_{c2}, but also the fundamental mechanism which induces such a high transition temperature. Elucidating the superconducting mechanism in FeSC should give us a route to higher T_c materials and a deeper understanding of condensed matter physics in strongly correlated materials.

1.2 Crystal structure and magnetic order of FeSC

Many types of FeSC have been discovered to date, and all of them are layered materials composed of conductive and blocking layers. In this thesis, I focus on the series of $A\mathrm{Fe_2As_2}$ (A=Ba, Sr, Eu, and Ca), which are easy to grow single crystals. I briefly review the experimental and theoretical studies of FeSC here. There are a lot of useful review articles have been published. [5, 6, 7, 8, 9] $A\mathrm{Fe_2As_2}$ at room temperature has tetragonal $\mathrm{ThCr_2Si_2}$-type (space group of $I4/mmm$) crystal structure as shown in Fig. 1.1 [10]. With decreasing temperature, the crystal shows a structural transition at T_s and the crystal structure changes from tetragonal to orthorhombic lattice with longer a and shorter b axes along the tetragonal [110] and [1$\bar{1}$0] directions, respectively.

At magnetic transition temperature T_AF usually below the T_s, the magnetic structure changes from paramagnetic to long-range magnetic ordered state [11]. The magnetic state is collinear antiferromagnetic state, or spin-density-wave state, with magnetic moment aligned antiferromagnetic along a-axis and ferromagnetic along b-axis, respectively, as shown in Fig. 1.2. This phase is so-called the antiferromagnetic-orthorhombic (AFO) phase. T_AF is coincide with T_s in the parent compound, such as $\mathrm{BaFe_2As_2}$, and they are separated with Co-doping [12] while are not separated with K and P-doping [13, 14].

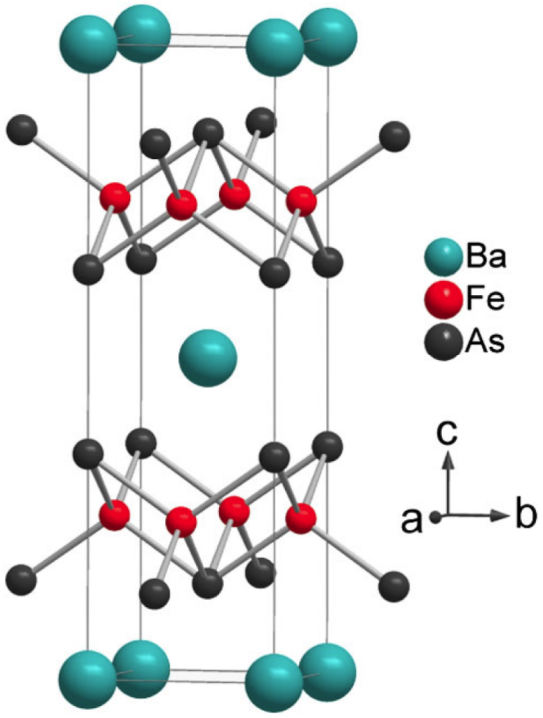

Figure 1.1: The crystal structure of $BaFe_2As_2$ [10].

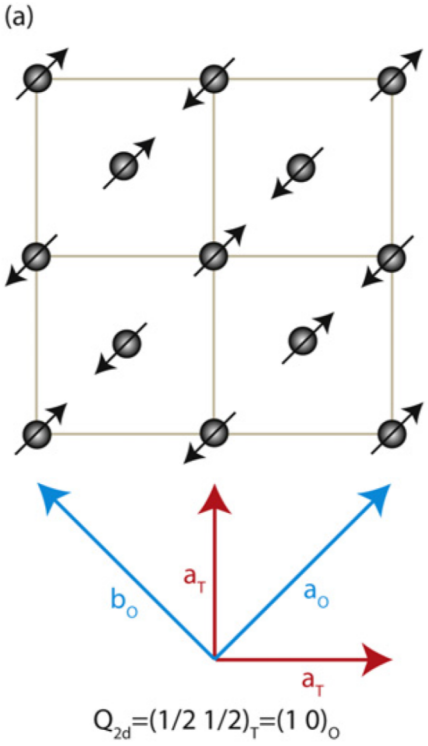

Figure 1.2: The crystal and magnetic structures of the $BaFe_2As_2$ in the antiferromagnetic-orthorhombic (AFO) phase [11]. The arrows mark the ordered moment directions of Fe in the AFO state. The a_T, b_T, and a_O, b_O show the principal crystal axes of the tetragonal and orthorhombic crystal structures, respectively.

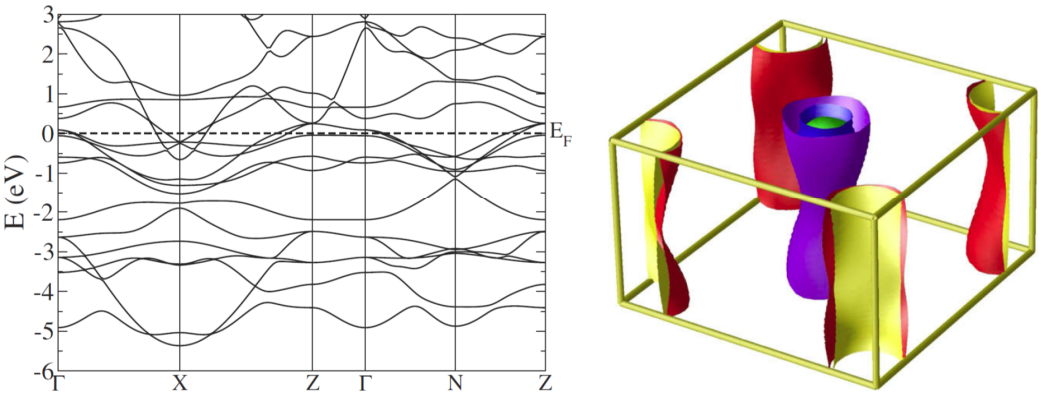

Figure 1.3: The calculated band structure of $BaFe_2As_2$ (left) [15] and the Fermi surface of the nonmagnetic $BaFe_2As_2$ for 10% electron-doping (Co doping, virtual crystal approximation) (right) [16].

1.2.1 Electronic structure

It is important to know the band structure of the material for understanding its physical property. The calculated band structure of $BaFe_2As_2$ in nonmagnetic state displays that five orbitals (d_{xy,yz,zx,z^2,x^2-y^2}) derived from Fe exist around Fermi energy (E_F) [15], shown in Fig. 1.3. This is in contrast to the cuprates where the Fermi surface consists of a single $d_{x^2-y^2}$ orbital. Figure 1.3 also shows the calculated Fermi surface of $BaFe_2As_2$ in nonmagnetic state [16]. There are two or more hole-like Fermi surfaces at the center of Brillouin zone (BZ), Γ point $\vec{k} = (0, 0)$, and two electron-like Fermi surfaces exist around M point $\vec{k} = (\pi, \pi)$. These Fermi surfaces are indeed observed by an angle resolved photo emission spectroscopy (ARPES) [17] and a quantum oscillation measurement [18]. Due to the cylindrical shape of the Fermi surfaces, a nesting between hole and electron Fermi surfaces can occurs and a spin-density-wave state appears at low temperatures. Below T_{AF}, the band structure is reconstructed due to the long-range magnetic order, and the reconstructed Fermi surface appears [19] as shown in Fig. 1.4.

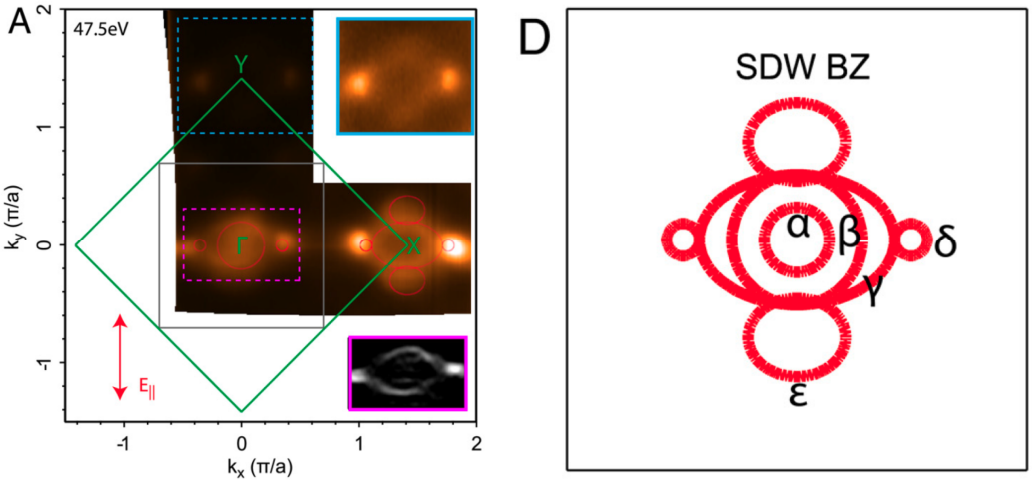

Figure 1.4: The observed reconstructed Fermi surface in the SDW phase (left) and a summary of measured Fermi surface outlines in the reconstructed SDW BZ (right) [19].

1.3 Phase diagram of FeSC

The structural and magnetic phase diagrams of electron-doped $Ba(Fe_{1-x}Co_x)_2As_2$ and hole-doped $(Ba_{1-x}K_x)Fe_2As_2$ are shown in Fig. 1.5 [20, 8]. The phase diagram of hole and electron-doped cuprates is also shown for the comparison in Fig 1.5. In both doped cases, the T_s and T_{AF} are suppressed with doping, and superconductivity emerges. In the underdoped region, the superconducting phase and the AFO phase coexists. After the superconducting transition temperature T_c reaches maximum, T_c decreases with further doping and goes to zero in the overdoped region. These phase diagrams are similar to that of the cuprates where electron or hole doping is necessary to suppress the antiferromagnetic order of parent compound and to induce superconductivity. In contrast to cuprates as shown in Fig. 1.5, superconductivity can emerge without carrier doping by applying a physical or a chemical pressure in iron pnictides [21, 22]. As shown in Fig. 1.6, the AFO phase suppressed by a hydrostatic pressure or isovalent substitution (Ru for Fe and P for As), and superconducting dome emerges in the phase diagram. These pressure dependence of the phase diagram is similar to that of carrier doping dependence, indicating that they share a common super-

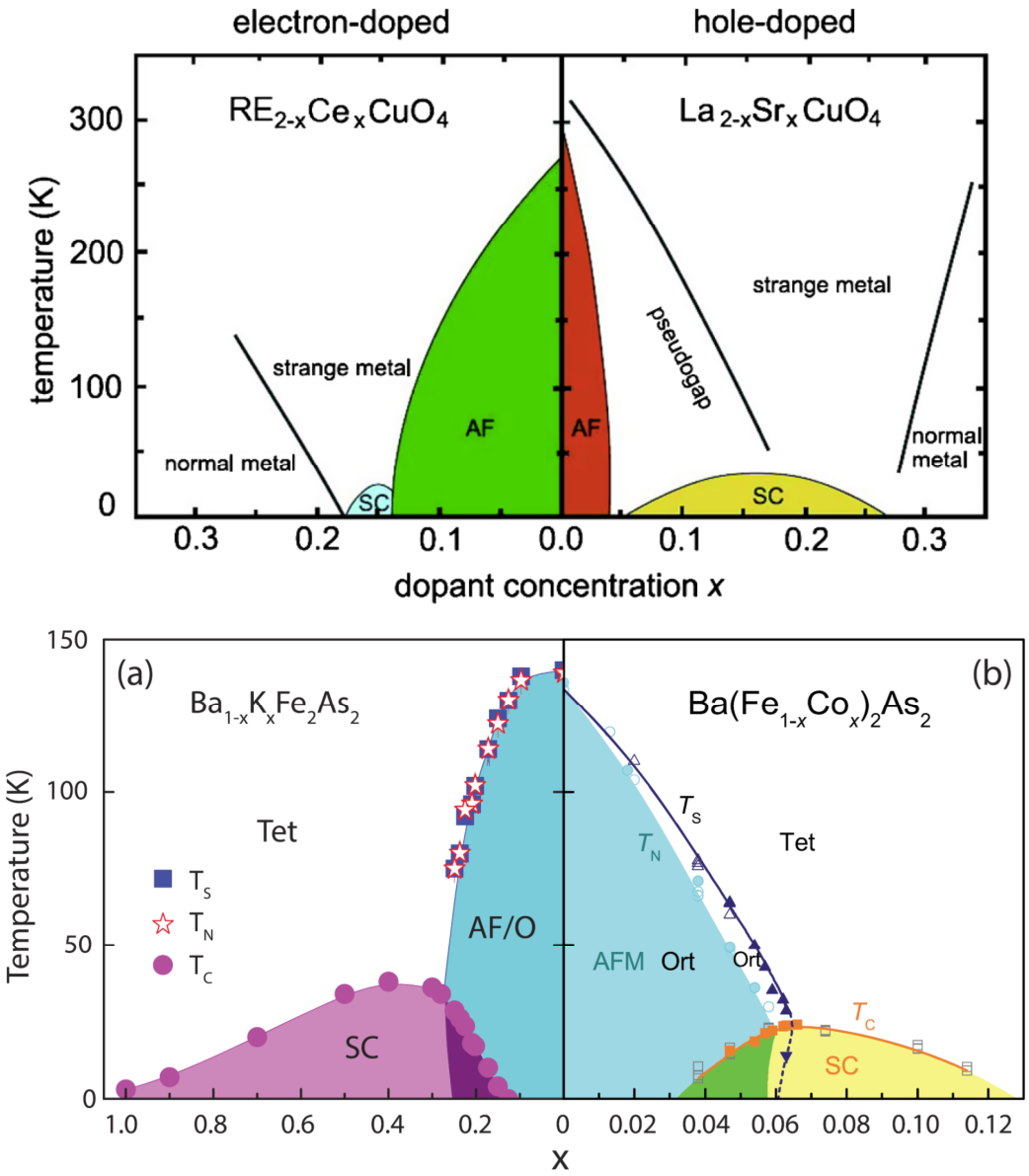

Figure 1.5: The electronic phase diagrams of hole/electron-doped cuprates [20] and those of electron-doped $Ba(Fe_{1-x}Co_x)_2As_2$ and hole-doped $(Ba_{1-x}K_x)Fe_2As_2$ [8].

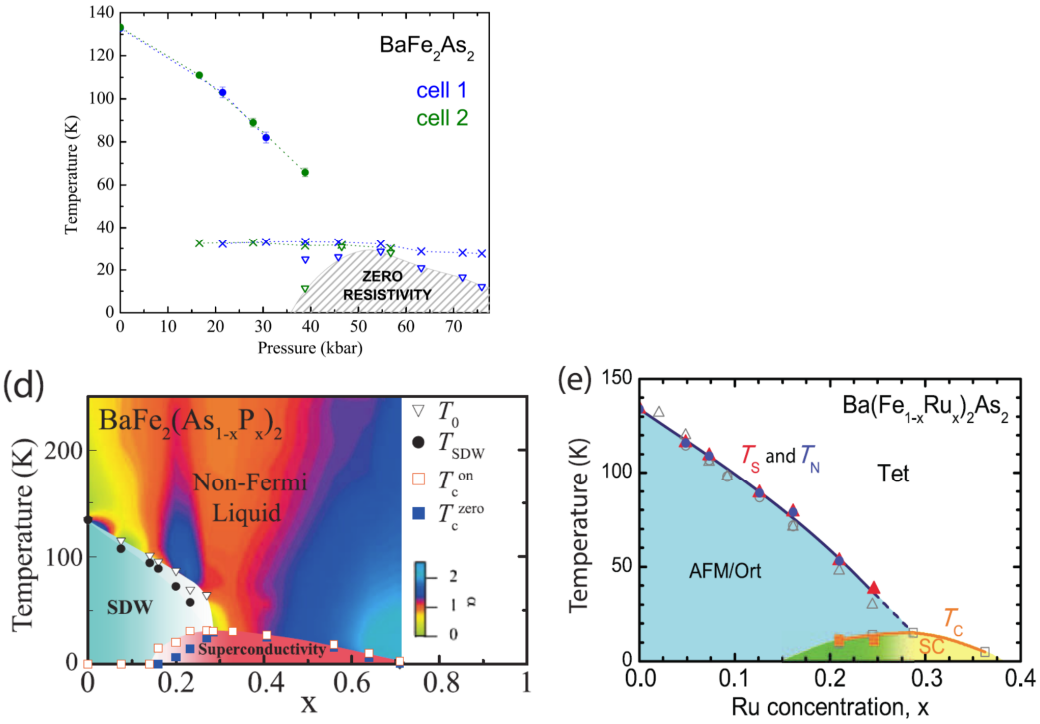

Figure 1.6: The structural and magnetic phase diagrams of $BaFe_2As_2$ under physical pressure (upper left) [22] and P-substituted $BaFe_2As_2$ (lower left) [23] and Ru-substituted $BaFe_2As_2$ (lower right) [21].

conducting mechanism. The situation is different in Cr and Mn-substituted $BaFe_2As_2$ (Cr and Mn-Ba122) [24, 25]. Cr and Mn substitution is expected to induce superconductivity because it is nominally hole doping as in K-substituted $BaFe_2As_2$. Cr and Mn substitution actually suppresses the AFO phase [Fig. 1.8(a)] but superconductivity does not appear. Instead of superconducting phase, another magnetic phase emerges in Cr and Mn-Ba122. In Cr-Ba122, G-type antiferromagnetic phase [Fig. 1.8(b)] appears in the overdoped side while tetragonal-SDW phase [Fig. 1.8(a)] appears in Mn-Ba122, as shown in Fig. 1.7.

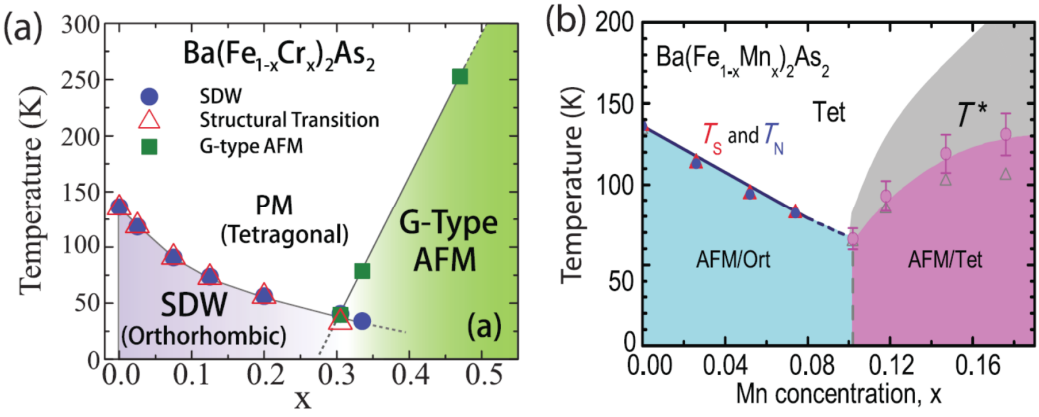

Figure 1.7: The structural and magnetic phase diagrams of Cr and Mn-substituted $BaFe_2As_2$ [24, 25].

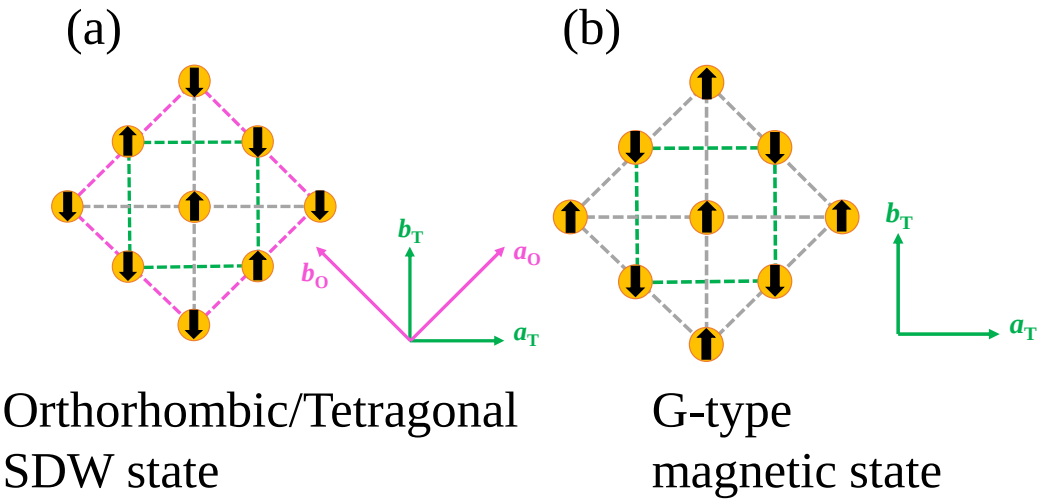

Figure 1.8: The schematic pictures of (a) orthorhombic/tetragonal-SDW, and (b) G-type magnetic structure. Circles and arrows on them represent Fe atoms and spin of Fe, respectively. The lattice constants a_O and b_O is different ($a_O > b_O$) in the orthorhombic-SDW state, while a_O and b_O is same in the tetragonal-SDW state.

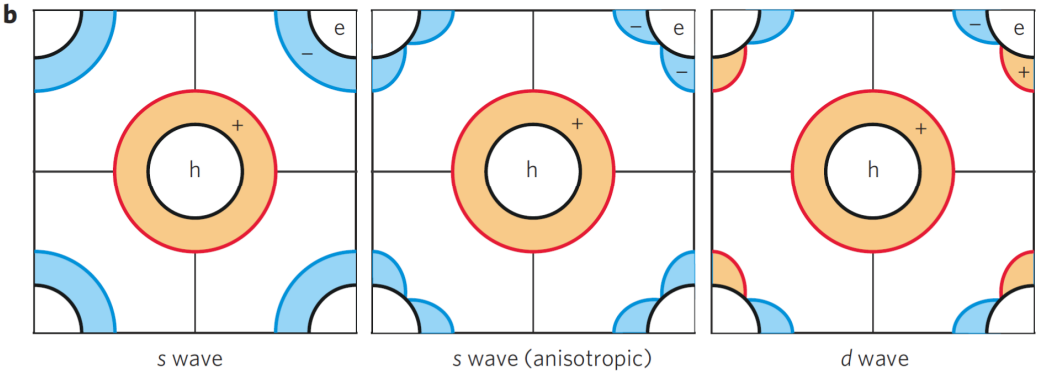

Figure 1.9: The proposed multiband pairing gap symmetries, drawn as shaded regions on hole (red) and electron (blue) pockets, are shown for an $s_{\pm}$ structure with isotropic gaps (left) and anisotropic gaps with accidental nodes on the electron pocket (middle), and for a d-wave symmetry (right) [5].

1.4 Superconducting property

1.4.1 Superconducting gap symmetry

In FeSC, it is assumed that a Cooper pair is mediated by a spin-fluctuation because superconducting phase exists close to magnetically ordered phase as in the case of cuprates [7]. In contrast to d-wave superconducting paring symmetry in cuprates, sign-reversed s-wave ($s_{\pm}$-wave) paring symmetry is theoretically predicted in FeSC, where an order parameter changes its sign between hole and electron Fermi surfaces, as shown in Fig. 1.9 [5]. On the other hand, based on the robustness of T_c against the impurity scattering, sign-preversed s-wave (s_{++}-wave) pairing mechanism mediated by an orbital-fluctuation is also proposed [26].

Superconducting properties are intensively studied by nuclear magnetic resonance (NMR) [27], specific heat [28], thermal conductivity [29], penetration depth [30], optical [31], scanning-tunneling-microscopy/spectroscopy (STM/STS) [32], neutron diffraction [33], and ARPES measurement [34]. They found that most of FeSC has an isotropic s-wave like gap structure while some materials, such as $BaFe_2(As_{1-x}P_x)_2$ [35], $Ba(Fe_{1-x}Ru_x)_2As_2$ [36] and KFe_2As_2 [37], have a gap node where the superconducting gap size goes

to zero at a part of the Fermi surfaces.

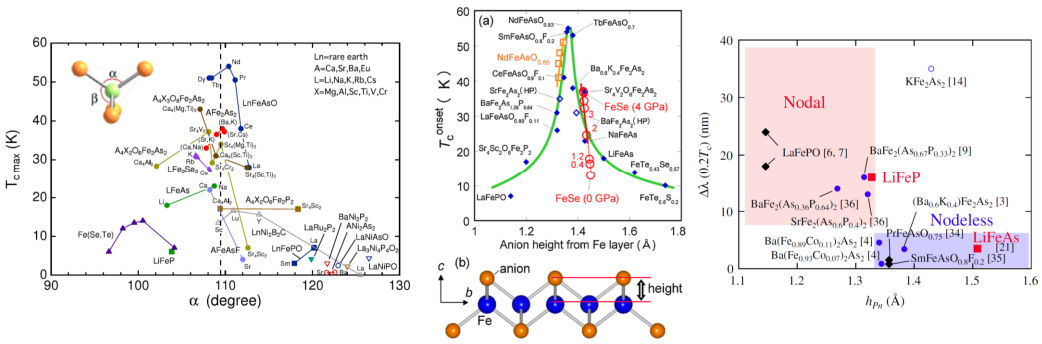

Figure 1.10: Maximum T_c for each system vs. bond angle α (left) [38], pnictogen height dependence of T_c for the typical Fe-based superconductors (center) [39], and pnictogen height dependence of $\Delta\lambda(T)$ at $T = 0.2T_c$ (right) [40].

1.4.2 Relationship between T_c and Crystal structure

It is required to elucidate the relationship between the superconducting property and the crystal structure in FeSC for enhancing the T_c and revealing the mechanism. The relationship between T_c and As-Fe-As bond angle (α) and a pnictogen height from Fe-plane (h_{Pn}) have been pointed out by Lee *et al.* [38] and Mizuguchi *et al.* [39], respectively, as shown in Fig. 1.10. Their findings suggest that T_c is optimized when $\alpha = 109.47°$ and $h_{Pn} = 1.38$ Å where $FeAs_4$-tetrahedron is a regular shape.

On the other hand, the relation between h_{Pn} and the superconducting gap structure has been pointed out by Hashimoto *et al.* [40], indicating that the gap structure change from a full gap to a nodal gap at $h_{Pn} = 1.32$ Å, as shown in Fig. 1.10.

They compared the different FeSC family compounds which has different carrier doping level and crystal structure because they focus on how a local structure around Fe site affect the superconducting property. Therefore how the lattice constants, such as a, c-axes, are related to the electronic structure and the phase diagram is not well addressed.

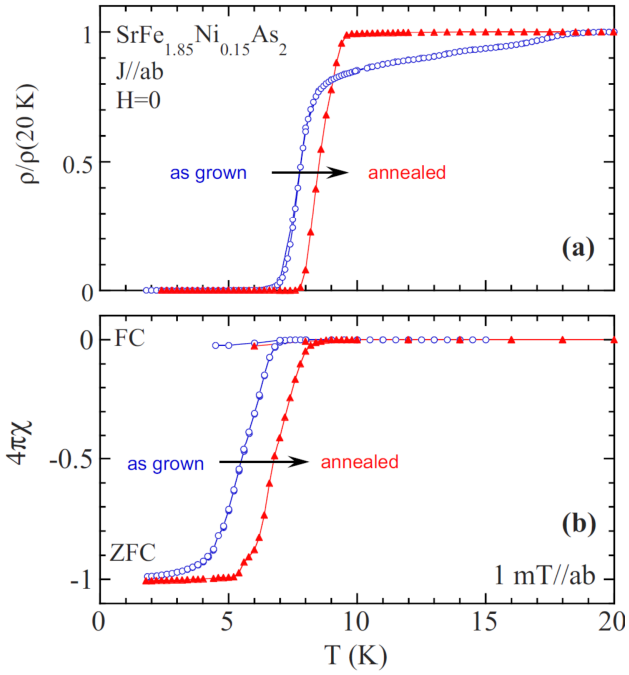

Figure 1.11: The post-annealing effect on the resistivity and magnetic susceptibility of $Sr(Fe_{2-x}Ni_x)_2As_2$ [41].

1.4.3 Post-annealing effect on superconducting properties

In FeSC, the as-grown single crystals contains amounts of disorders, lattice dislocations, or defects inside it. Considering that the introduction of point defects into FeSC leads to the suppression of T_c [42], these disorders would be harmful to the superconducting property. Actually, it is reported that the post-annealing treatment of the as-grown crystals results in the reduction of the residual resistivity and the enhancement of T_c as shown in Fig. 1.11 [41]. Although the post-annealing treatment improves the superconducting properties, it is not unclear what happens inside the single crystal before and after the post-annealing treatment. Therefore it is required to investigate the post-annealing effect on the details of the single crystal, such as the crystal structure.

1.5 Normal state property

FeSC has interesting property not only in the superconducting phase but also in the normal state above T_c. Here I overview the unusual electronic property in the normal state in terms of an electronic anisotropy and an optical property.

1.5.1 Electronic anisotropy

One of the most anomalous electronic property in the normal state is the electronic anisotropy observed in the AFO and paramagnetic-orthorhombic phase [43, 44]. Chu *et al*. found that the in-plane resistivity shows significant anisotropy in the AFO phase at low temperatures in the detwwined $Ba(Fe_{1-x}Co_x)_2As_2$ [45]. The resistivity along the longer a-axis with an antiferromagnetic spin arrangement (ρ_a) is smaller than that along the shorter b-axis with a ferromagnetic spin arrangement (ρ_b), as shown in Fig. 1.12. This observed anisotropy ($\rho_b > \rho_a$) is counterintuitive because both of the larger orbitals overlap due to a smaller lattice constant and smaller spin-fluctuation scattering due to a ferromagnetic spin arrangement, which should give a smaller resistivity in the b-direction ($\rho_b < \rho_a$). In addition to AFO phase, the in-plane resistivity anisotropy is already observed well above T_s. This is unexpected because the original C_4-symmetry in crystal and magnetic state should be broken below the temperature of the structural and antiferromagnetic transition both of which lowering the C_4-symmetry to C_2-symmetry.

The related anomalous anisotropy is observed by ARPES [19], elastoresistance [46], x-ray linear dichroism [47], optical [48], thermoelectric power [49], scanning-tunneling-microscopy/spectroscopy (STM/STS) [50, 51, 52], neutron diffraction [53], x-ray diffraction [54] and magnetic torque measurement [55] in various FeSC, but the mechanism and the relation to the superconductivity are still remains unclear [56].

1.5.2 Optical property

Optical spectrum is a bulk-sensitive and useful energy-resolved probe for investigating the charge excitations and dynamics of relevant carriers [58, 59]. A typical spectrum of optical conductivity of parent compounds of FeSC is

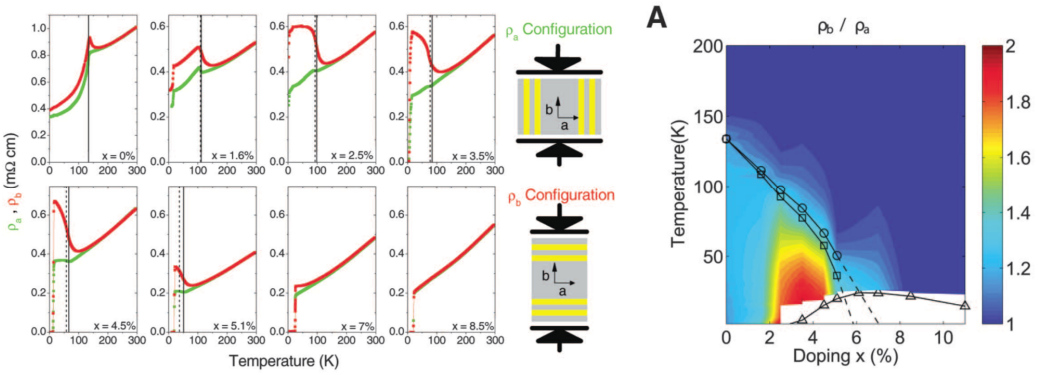

Figure 1.12: (Left panel) Temperature dependence of the in-plane resistivity ρ_a (green) and ρ_b (red) of $Ba(Fe_{1-x}Co_x)_2As_2$ for Co concentrations from $x = 0$ to 0.085. Solid and dashed vertical lines mark critical temperatures for the structural and magnetic phase transitions T_s and T_{AF}, respectively. (Right panel) Evolution of the in-plane resistivity anisotropy as a function of temperature and doping, expressed in terms of the resistivity ratio ρ_b/ρ_a [45].

shown in Fig. 1.13 [57]. In the paramagnetic-tetragonal (PT) phase, low-energy region is dominated by a coherent and an incoherent Drude components, which reflect that FeSC is a multi-band system. The coherent component is considered as an electron-type carrier and the incoherent one is attributed to a hole-type carrier [60, 61]. In the AFO phase, SDW gap like feature is observed around $1000\,\mathrm{cm}^{-1}$ but the Drude component is still observed. This suggests that the SDW gap opens at a part of Fermi surfaces, which is consistent with a metallic behavior below T_{AF} observed by a resistivity measurement. The observed features of optical conductivity both in PT and AFO phases are well reproduced by theoretical calculations based on dynamical mean field theory (DMFT) taking account of sizable Hund's-coupling correlation between quasiparticles [57].

1.6 Aim of this study

Despite intensive experimental and theoretical works on FeSC, the origin of superconducting mechanism and normal states, such as an electronic

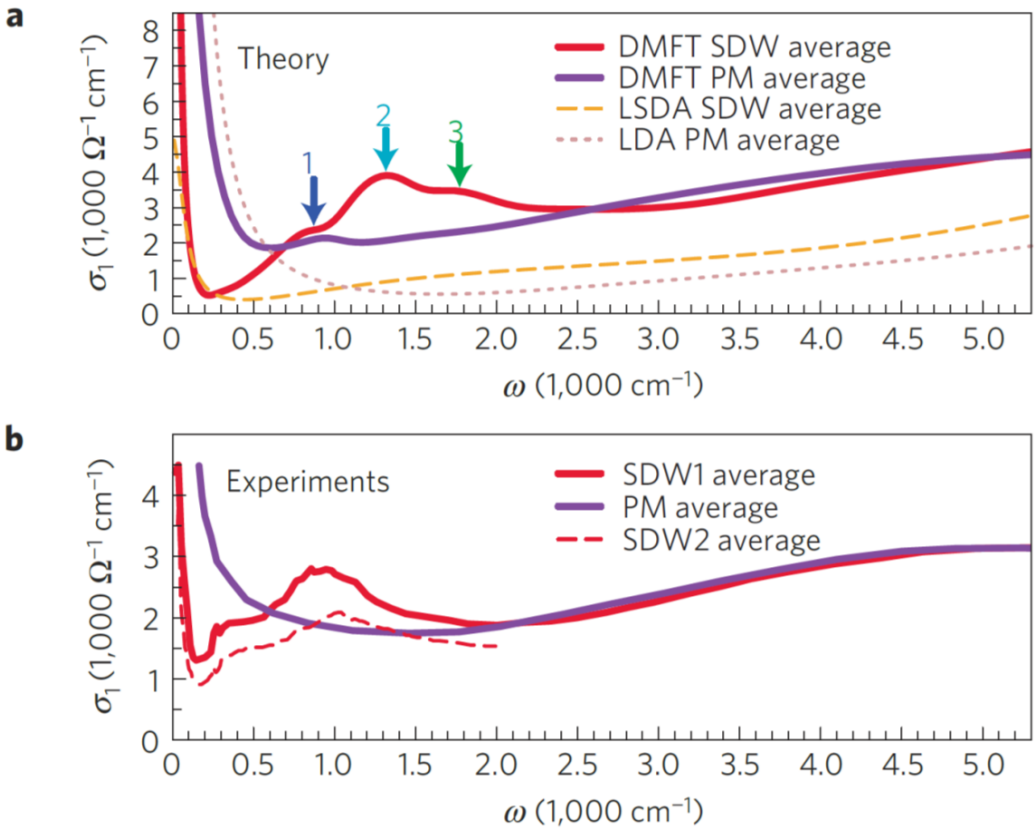

Figure 1.13: Calculated and experimental optical conductivity of $BaFe_2As_2$ [57].

anisotropy are still unsettled. In this thesis, I studied the following problem.

1) The relationship between the crystal structure and T_c is are proposed by several studies, but it remains open question how the structural change affects the electronic structure and how the T_c correlates with Fermi surface topology. In this thesis, I studied $SrFe_2(As_{1-x}P_x)_2$ comparing with $BaFe_2(As_{1-x}P_x)_2$ to reveal how the difference of the crystal structure is connected with the electronic structure and superconducting properties.

2) The electronic anisotropy is a key issue to understand the normal and superconducting properties in FeSC. This anisotropy cannot be explained by the structural anisotropy, indicating that spin/orbital degree of freedom play an important role for the anisotropy and they should be related with the superconducting mechanism. In particular, the origin of the resistivity anisotropy both in the AFO and nematic phase is still controversial. To answer this question, I studied the in-plane resistivity anisotropy of Cr, Mn, and Co-Ba122 systems. Comparing these systems, I studied how the impurity scattering and carrier doping affect the in-plane resistivity anisotropy, and demonstrated the importance of the Fermi surface topology for the anisotropy.

3) In the optical study of FeSC, parent and superconducting compounds have been mainly investigated. In this thesis, I focus on the effect of carrier doping and impurity scattering on the charge dynamics of Cr, Mn, and Co-Ba122 in PT and AFO phase. These compounds share the common magnetostructural phase but shows the different phase diagrams, where superconducting phase emerges in Co-Ba122 but not in Cr and Mn-Ba122. The charge dynamics of these compounds is expected to give ingredients for the emergence of superconductivity in FeSC.

The part III and the part IV of this thesis are based on the published work [7, 9, 15] and [4], respectively.

Part II

Experimental methods

2.1 Single crystal growth

2.1.1 $SrFe_2(As_{1-x}P_x)_2$

Single crystals of $SrFe_2(As_{1-x}P_x)_2$ (P-Sr122) except for $x = 0$ and $x = 1$ were grown from a stoichiometric mixture of Sr, FeAs, and FeP powder. FeAs was prepared by reating Fe powder and As grains at 850 °C for 15 h in a evacuated quartz tube. FeP was prepared by reating Fe powder and P powder at 700 °C for 15 h in a evacuated quartz tube.

Sr, FeAs, and FeP were mixed in the atomic ratio $1{:}2(1-x){:}2x$, placed in an alumina crucible, sealed in a silica tube with Ar gas of 0.2 bar at room temperature. It was heated up to 1300 °C, was kept for 12 h, and then slowly was cooled down to 1050 °C at a rate of 2 °C/h.

$SrFe_2As_2$ ($x = 0$) was grown by FeAs-flux method. Sr and FeAs were mixed in the atomic ratio 1:4, placed in an alumina crucible, sealed in a silica tube with Ar gas of 0.2 bar at room temperature. It was heated up to 1200 °C, was kept for 12 h, and then was slowly cooled down to 1050 °C at a rate of 2 °C/h.

$SrFe_2P_2$ ($x = 1$) was grown by Sn-flux method. Sr, FeP, and Sn were mixed in the atomic ratio 1:2:20, placed in an alumina crucible, sealed in a silica tube with Ar gas of 0.2 bar at room temperature. It was heated up to 1300 °C, was kept for 12 h, and then was slowly cooled down to 600 °C at a rate of 5 °C/h. The Sn-flux was removed by a centrifuge.

For the comparison, I grew single crystals of $BaFe_2(As_{1-x}P_x)_2$ (P-Ba122) ($x = 0.20$ and 0.25) by Ba_2As_3/Ba_2P_3 flux method described in ref. [62].

The compositions of the obtained crystals were determined with an electron probe microanalyzer (EPMA) for P-Sr122 and a scanning electron microscope/energy dispersive x-ray spectroscopy (SEM-EDX) for P-Ba122.

2.1.2 $Ba(Fe_{1-x}TM_x)_2As_2$ (TM=Cr, Mn, and Co)

Single crystals of $Ba(Fe_{1-x}TM_x)_2As_2$ (TM=Cr, Mn, and Co) were grown by a self-flux method. MnAs was prepared by reating Mn powder and As grains at 850 °C for 15 h in a evacuated double sealed quartz tube, because it reacts with a quartz tube. Particularly, it is necessary to pay attention to the synthesis of CrAs. If the same synthesis condition for FeAs is adopted, the quartz tube is exploded during the heating. To avoid this problem, less amount of mixture of Cr and As (∼3g) was loaded into a quartz tube, and

the tube was heated to 850 °C for 48 h and kept for 15 h at the temperature.

Ba, FeAs, and TMAs were mixed in the atomic ratio $1{:}4(1-x){:}4x$, placed in an alumina crucible, and sealed in a quartz tube. The tube was heated to 1200 °C, kept at that temperature for 10 h, and cooled to 1000 °C at a rate of 2 °C/h. The compositions of the grown crystals were determined by SEM-EDX analysis.

2.1.3 Post annealing treatment

Single crystals of $SrFe_2(As_{1-x}P_x)_2$ and $Ba(Fe_{1-x}TM_x)_2As_2$ (TM=Cr, Mn, and Co) were sealed in an evacuated silica tube, and annealed at 500 °C and at 800 °C for several days days, respectively.

2.2 Transport measurement

2.2.1 Resistivity measurement

A standard four-probe method was used for a resistivity measurement of twined and detwinned single crystals.

2.2.2 Hall coefficient measurement

The Hall resistivity, ρ_{xy}, was measured with the electric current along the ab-plane and the magnetic field applied along the c-axis. The measurement was performed in the magnetic field up to 7 T at various temperatures using twinned crystals. The Hall coefficient, R_H, was determined by the polynomial fitting of the Hall resistivity with $\rho_{xy} = R_H H + aH^3$, where H is the magnetic field.

2.2.3 Resistivity measurement with detwinned crystal

Below the structural transition temperature, T_s, the crystal tends to form structural twins, which prevent the measurement of the in-plane anisotropy of iron-pnictide. To measure the in-plane anisotropy of the resistivity, a single domain crystal is required. I detwinned the single crystals by applying a uniaxial pressure along [110] direction in the tetragonal lattice. The measurements of the in-plane resistivity along both a and b-axes of the orthorhombic lattice were performed on detwinned samples by a standard four-probe

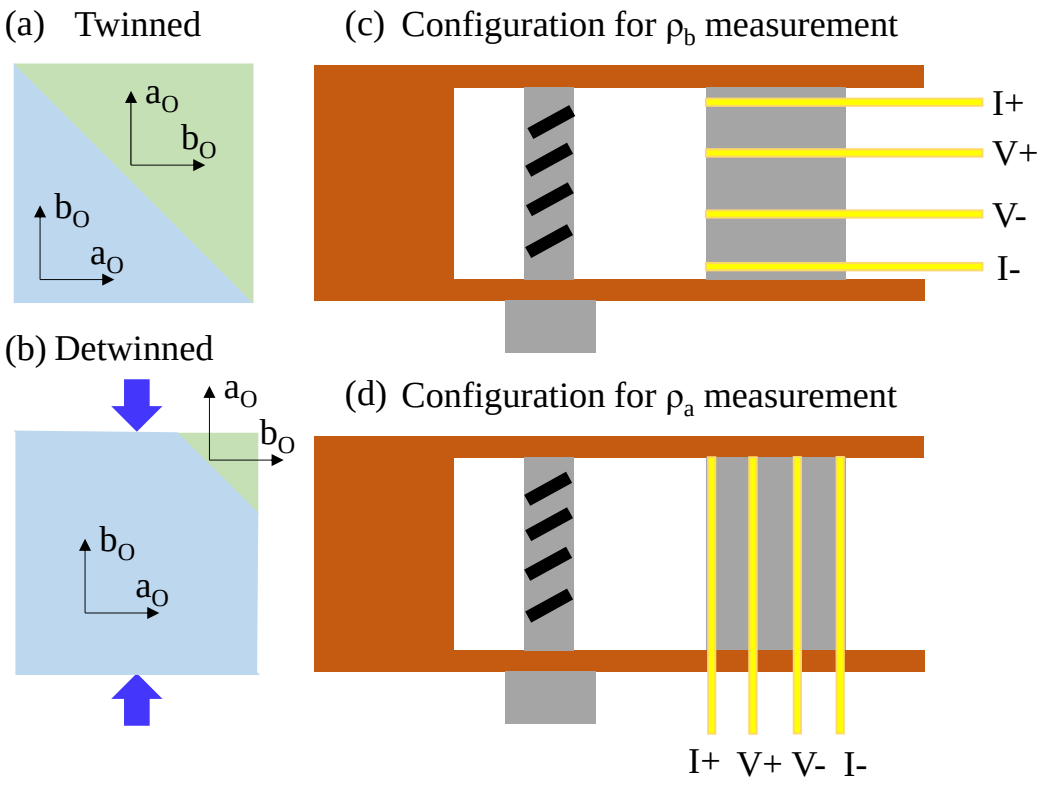

Figure 2.14: Schematic picture of a twinned (a) and a detwinned (b) crystals. Two sets of domains have the same population for the twinned crystal, whereas one set of domains have a dominant population for the detwinned crystal. (c) and (d) show a schematic picture of a four-probe measurement of the detwinned crystal on the detwinning device, respectively.

method. I repeated the resistivity measurements with increasing pressure and confirmed the saturation of the anisotropy. A schematic picture of the measurement method are shown in Fig. 2.14.

2.3 Magnetization

Magnetization measurements from 1.8 K to 300 K were performed using a Quantum Design magnetic property measurement system (MPMS). Zero-field-cooled (ZFC) and field-cooled (FC) data were taken at 10 Oe for superconducting samples.

2.4 X-ray diffraction measurement

The x-ray diffraction experiment of single crystals for determining lattice constants was performed using 4 circle crystal x-ray diffractometer. The x-ray diffraction experiment for single crystals structural analysis was carried out using the x-ray with 15 keV at BL-8A of the Photon Factory, KEK in Japan. In order to determine the atomic positions of $SrFe_2(As_{0.65}P_{0.35})_2$, I used those of $SrFe_2As_2$ as starting parameters and refined them by the least-squares method using Rigaku CRYSTALSTRUCTURE.

2.5 Specific heat measurement

Specific heat was measured by a relaxation technique down to 1.8 K in a magnetic field up to 14 T using a Quantum Design physical properties measurement system (PPMS).

2.6 Optical measurement

The optical reflectivity $R(\omega)$ was measured on the ab plane of the mechanically polished samples using 0.3-μm grain-size Al_2O_3 powder and lapping film sheets. The measurement was performed at various temperatures in the frequency range 50-20000 cm^{-1} by a Fourier transform infrared spectrometer at our laboratory, and in the frequency range 20000-320000 cm^{-1} at UVSOR facility, Okazaki, Japan at room temperature. Below the frequency range

$50\,\mathrm{cm}^{-1}$, Hagen-Rubens formula ($R \propto 1-\alpha\sqrt{\omega}$) was used to extrapolate. At higher energy region (above $320000\,\mathrm{cm}^{-1}$), an extrapolation of $R \propto \omega^{-4}$ had been used.

The optical conductivity was obtained by using Kramers-Kronig relation (KK-relation). The complex reflectivity $\hat{r}(\omega)$ can be given as follows.

$$\hat{r}(\omega) = \frac{1-\sqrt{\hat{\epsilon}(\omega)}}{1+\sqrt{\hat{\epsilon}(\omega)}} = \sqrt{R(\omega)}exp(i\theta(\omega)) \tag{2.1}$$

Here $\hat{\epsilon}(\omega)$ is the complex dielectric function, and $\theta(\omega)$ is the phase. $\hat{\epsilon}(\omega)$ is given as follows.

$$\hat{\epsilon}(\omega) = \epsilon_1(\omega) + i\epsilon_2(\omega) \tag{2.2}$$

$$\epsilon_1(\omega) - 1 = \frac{2}{\pi}P\int_0^\infty \frac{\omega'\epsilon_2(\omega')}{\omega'^2-\omega^2}d\omega' \tag{2.3}$$

$$\epsilon_2(\omega) = -\frac{2\omega}{\pi}P\int_0^\infty \frac{\epsilon_1(\omega')}{\omega'^2-\omega^2}d\omega' \tag{2.4}$$

$R(\omega)$ is experimentally measured, then I can calculate the phase $\theta(\omega)$ with KK-relation as follows.

$$\theta(\omega) = -\frac{2\omega}{\pi}P\int_0^\infty \frac{ln\sqrt{R(\omega')}}{\omega'^2-\omega^2}d\omega' \tag{2.5}$$

Once I have the real and imaginary part of the complex reflectivity, I can obtain the complex dielectric function.

The complex optical conductivity $\hat{\sigma}(\omega) = \sigma_1(\omega) + i\sigma_2(\omega)$ is obtained with dielectric functions as follows.

$$\sigma_1(\omega) = \frac{\omega\epsilon_2(\omega)}{4\pi} \tag{2.6}$$

$$\sigma_2(\omega) = \frac{\omega(1-\epsilon_1(\omega))}{4\pi} \tag{2.7}$$

Drude-Lorentz model for the dielectric function $\hat{\epsilon}(\omega)$ was used to describe the optical conductivity.

$$\hat{\epsilon}(\omega) = \epsilon_\infty + \sum_j \frac{\omega_{p,D;j}^2}{\omega^2 + i\omega/\tau_{D,j}} + \sum_k \frac{\Omega_k^2}{\omega_k^2 - \omega^2 - i\omega\gamma_k} \tag{2.8}$$

Here ϵ_∞ is the real part of the dielectric function at a high frequency, $\omega_{p,D;j}^2 = 4\pi n_j e^2/m_j^*$ and $1/\tau_{D,j}$ are the square of the plasma frequency and scattering rate for Drude carrier in the jth Fermi surface, respectively. n_j and m_j^* are the carrier density and carrier mass for the carrier in the jth Fermi surface, respectively. ω_k, γ_k, and Ω_k are the position, width, and strength of the kth vibration or excitation, respectively.

Part III

Electronic phase diagram and superconducting property of $\mathbf{SrFe_2(As_{1-x}P_x)_2}$

3.1 Introduction

Most of iron-based superconductors (FeSC) are layered materials composed of conductive and blocking layers [6]. The electronic band calculations have revealed that a two-dimensional conductive layer results in multiple Fermi surfaces consisting of disconnected cylindrical hole and electron pockets [7]. It is theoretically proposed that the nesting between those pockets induces spin density wave in the parent compounds and spin fluctuations that mediate Cooper pairing in the superconducting ones. The superconductivity mediated by spin fluctuations leads to the superconducting state with $s_{\pm}$-wave symmetry where the gaps on the different Fermi surfaces have the different sign [63]. On the other hand, considering the robustness of T_c to the impurity effect, s_{++}-wave superconducting gap symmetry is also proposed based on the superconducting mechanism mediated by the orbital fluctuations where the gaps on the different Fermi surfaces have the same sign [26].

$A\mathrm{Fe_2As_2}$ (A=Ba, Sr, Eu, and Ca), one of the parent compounds of FeSC, exhibits the magnetostructural transition from the paramagnetic-tetragonal (PT) phase to the antiferromagnetic-orthorhombic (AFO) one below the transition temperature T_{AFO} [6]. Carrier doping by chemical substitution and physical pressure suppresses the magnetostructural phase transition and induces superconductivity. Another means of inducing superconductivity is the application of chemical pressure by the isovalent substitution of As for P. In particular, $\mathrm{BaFe_2(As_{1-x}P_x)_2}$ (P-Ba122) attracts much attention in terms of the nodal superconducting gap and magnetic quantum criticality [23].

According to previous studies of $A\mathrm{Fe_2(As_{1-x}P_x)_2}$ (P-A122, A=Ba, Eu, and Ca) with single crystals [23, 64, 65], as the lattice constants are reduced (Ba>Eu>Ca), superconductivity is induced with a smaller amount of P-substitution, and the optimal superconducting transition temperature $T_{c,optimal}$ decreases. In these systems, it was confirmed that the decrease in the anisotropy ratio of lattice constants (c/a) makes the Fermi surface more three-dimensional, namely, the electronic anisotropy is reduced [18, 66]. In this work, I use c/a as a measure of the structural and electronic dimensionalities. The observed tendency in P-A122 implies that the anisotropy of the crystal structure and the resultant Fermi surface topology play an essential role in the superconductivity of FeSC. It supports the theoretical model in which the Fermi surface nesting is crucial. In contrast to P-A122 (A=Ba, Eu, and Ca), the related compound $\mathrm{SrFe_2(As_{1-x}P_x)_2}$ (P-Sr122) has not been

studied in detail. An early study of polycrystalline P-Sr122 showed the electronic phase diagram up to $x \leqq 0.40$, but the compound with $x \geqq 0.40$ was not obtained [67]. To clarify the relationship between the crystal structure and the superconductivity in FeSC, it is important to determine whether or not P-Sr122 follows the tendency mentioned above.

On the other hand, it has been reported that the postannealing treatment sometimes improves the sample quality and induces a marked changes in the electronic properties of FeSC [68]. Therefore, the postannealing treatment is necessary to reveal the intrinsic electronic properties of FeSC.

In this work, I performed a systematic study of the single crystal x-ray diffraction, magnetic susceptibility, electric resistivity and Hall resistivity of single crystals of P-Sr122 with $0 \leqq x \leqq 1$ before and after postannealing treatment. I succeeded in growing single crystals of P-Sr122 with $0 \leqq x \leqq 1$ for the first time and in establishing its complete electronic phase diagram. Single crystal structure analysis revealed that annealed crystal had the better bond angle and/or pnictogen height. It was found that the postannealing treatment resulted in the reduction in the residual resistivity in the AFO phase and the enhancement of T_c in the superconducting phase, which enlarges the T_c dome in the phase diagram. The optimal T_c reaches 33 K, which is the highest among those of P-A122 (A=Ba, Sr, Eu, and Ca). The obtained phase diagram is similar to that of P-Ba122 despite the large difference in lattice constants.

In addition, I performed specific heat measurement of an as-grown and annealed $SrFe_2(As_{0.65}P_{0.35})_2$ single crystals. The as grown crystal has T_c=26 K, while the annealed crystals has T_c=33 K which is higher than optimal P-Ba122 (T_c=31K) [23]. I observed that a magnetic field dependence of the residual electronic specific term $\gamma_r(H)$ of the as-grown crystal was sub-linear dependence, while the annealed crystal showed smaller residual term and H-linear field dependence. I attributed the reason of higher T_c to the change from dirty to clean limit state due to smaller impurity or inhomogeneity and ideal crystal structure realized by annealing.

3.2 Annealing effect

To determine the best annealing conditions, I annealed the crystals at various temperatures for various durations. At first, I annealed the crystals of $SrFe_2(As_{0.65}P_{0.35})_2$ for 2 days at different temperatures. Figure 3.15(a) shows

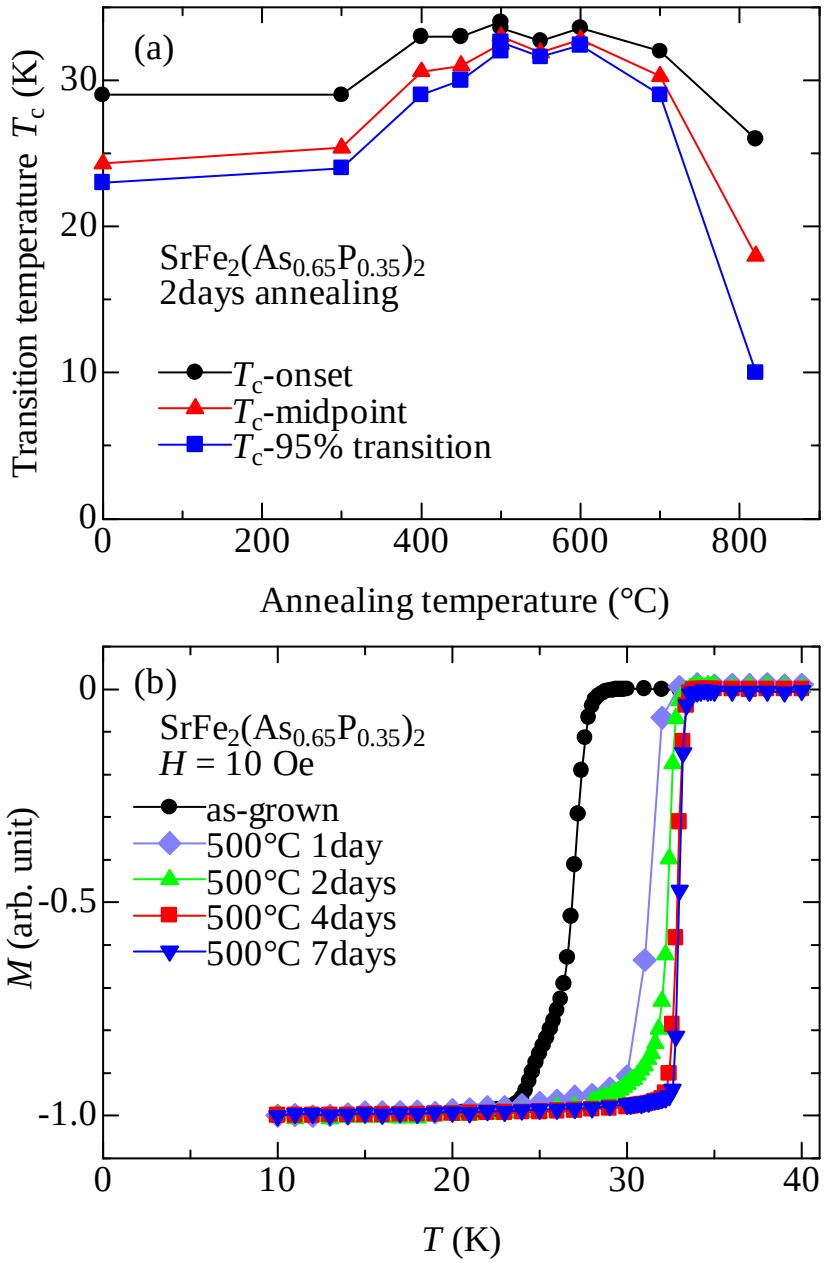

Figure 3.15: (a) Annealing temperature dependence of T_c for $x = 0.35$. (b) Annealing time dependence of the magnetization M for $x = 0.35$ at magnetic field $H = 10\,\mathrm{Oe}$ applied along c-axis.

the annealing temperature dependence of T_c determined from the magnetization M. I found that the annealing treatment at 500 °C gives the highest T_c among all the examined temperatures. The annealing treatment at 800 °C damaged the sample and strongly suppressed T_c. Next, fixing the temperature at 500 °C I annealed the crystals for various durations. The onset T_c reached 33 K after 4 days of postannealing, and did not change even when they were annealed for longer durations, as shown in Fig. 3.15(b). It is noted that the postannealing time depends on the sample size. The crystals for the specific heat measurement was $3 \times 3 \times 0.1\text{mm}^3$ size and annealed in an evacuated silica tube for 2 weeks at 500 °C, while the crystals for other measurements were $1 \times 1 \times 0.1\,\text{mm}^3$ and annealed for 1 week.

3.3 Structural analysis

Figure 3.16(a) shows the P-content determined by EPMA. I use nominal x values hereafter because the actual compositions x' are nearly the same as the nominal ones ($x' = 0.979 \times x$). It is noted that the compositions are not changed by the post-annealing treatment. Figure 3.16(b) shows the P-content dependences of the lattice parameters for the as-grown crystals. The lattice constants a and c decrease monotonically as the P-content x increases. The anisotropy ratio c/a and the unit cell volume V also decrease with increasing x, as shown in Fig. 3.16(c). These results suggest that P-substitution causes a chemical pressure.

The c/a of $SrFe_2As_2$ is largest ($\sim$ 3.15) among P-Sr122 but is smaller than that of $BaFe_2P_2$, which is the smallest ($\sim$ 3.24) among P-Ba122. This indicates that the crystal structure of P-Sr122 is less anisotropic than that of P-Ba122. Actually, the photoemission measurement revealed that the Fermi surface topology of $SrFe_2(As_{0.65}P_{0.35})_2$ is more three-dimensional than that of P-Ba122 as well as the crystal structure [66].

Figure 3.16(d) shows the P-content dependences of the pnictogen height (h_{Pn}) for P-Sr122 and P-Ba122. Despite the substantial differences in lattice parameters, h_{Pn} and its doping dependence are similar in both systems.

Table 3.1 shows the annealing effect on the crystal structure measured by the single crystal x-ray diffraction measurement at KEK. In the analysis, I adjusted the coordinate z of As/P simultaneously. The structural analysis clearly demonstrates that the annealed crystal has the shorter a-axis and longer c-axis than the as-grown crystal. In addition, the z position of As/P

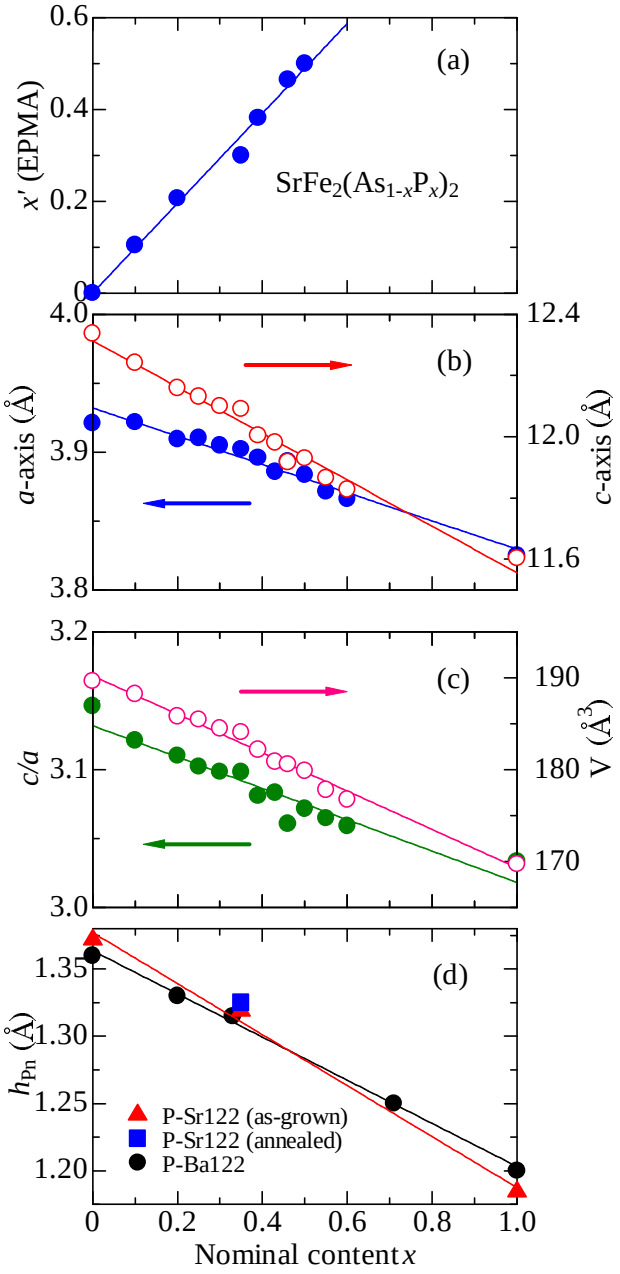

Figure 3.16: P-content dependences of (a) actual compositions determined by EPMA in single crystals of $SrFe_2(As_{1-x}P_x)_2$, (b) a- and c-axes lattice constants, (c) anisotropy ratio c/a and unit cell volume (V), and (d) pnictogen height h_{Pn}. The data for $x = 0$, 1.0 and P-Ba122 in (d) are cited from Refs. [23, 67], respectively. The solid lines in (a), (b), (c), and (d) are visual guides.

Compound	as-grown	annealed
Space group	$I4/mmm$	$I4/mmm$
a (Å)	3.8983(14)	3.8963(6)
c (Å)	12.064(4)	12.092(2)
V (Å^3)	183.33(11)	183.57(5)
Sr	(0, 0, 0)	(0, 0, 0)
Fe	(1/2, 0, 1/4)	(1/2, 0, 1/4)
As/P	(0, 0, z)	(0, 0, z)
	z=0.35931(6)	z=0.35956(5)
h_{Pn}(Å)	1.319(1)	1.325(1)
Bond lengths and angles		
Sr-As(Å)	3.2372(7)	3.2364(3)
Sr-Fe(Å)	3.5910(9)	3.5964(4)
Fe-As/P(Å)	2.3533(4)	2.3559(3)
Fe-Fe(Å)	2.7565(7)	2.7551(3)
As-Fe-As(deg.)	108.301(10)×4	108.434(8)×4
	111.84(2)×2	111.566(17)×2
Isotropic atomic displacement parameter		
Sr	0.601(10)	0.776(11)
Fe	0.330(12)	0.486(11)
As	0.451(8)	0.575(10)
P	3.2(3)	2.84(19)
Number of reflections	211	219
(I>2.00σ(I))		
Good of fitness	3.315	6.018

Table 3.1: Refined lattice constants, atomic positions, bond lengths, and angles at room temperature for the as-grown and annealed single crystals from the least square refinement of single crystal x-ray diffraction profile. h_{Pn} was calculated from $h_{\mathrm{Pn}} = (z - 0.25) \times c$. The reliability are R_1 $(I > 2.00\sigma(I)) = 6.61\%, 5.16\%$ and wR_2 $(I > 2.00\sigma(I)) = 10.17\%, 8.15\%$ for the as-grown and annealed crystals, respectively. Number of reflections is number of diffraction peaks used for analysis.

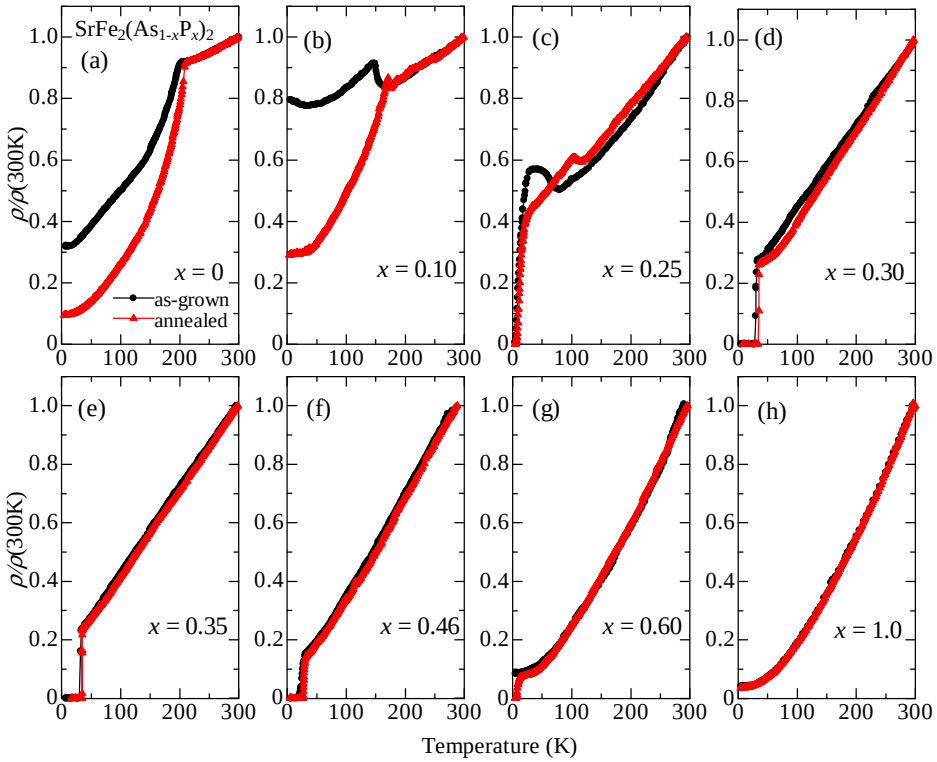

Figure 3.17: (a)-(h) Temperature dependence of the resistivity before and after annealing for $0 \leqq x \leqq 1$. The absolute value of $\rho(300\,\mathrm{K})$ decreases from $0.29\,\mathrm{m\Omega{\cdot}cm}$ for $x = 0$ to 0.22 for $x = 0.35$ and 0.030 for $x = 1$. The solid lines are visual guides.

also increases, leading to a higher pnictogen height h_{Pn} and a smaller As-Fe-As bond angle. In FeSC, it has been pointed out that T_c is correlated with the pnictogen height and/or the As-Fe-As bond angle [38, 39]. Considering that T_c sharply changes around $h_{\mathrm{Pn}} \sim 1.33$ Å[39], a tiny extension of h_{Pn} in $SrFe_2(As_{0.65}P_{0.35})_2$ (~ 1.32 Å) can result in an enhancement of T_c.

3.4 Transport measurement

In Figs. 3.17(a)-3.17(h), I show the temperature dependence of resistivity $\rho(T)$ for $0 \leqq x \leqq 1$. The data are normalized by the value at room tem-

perature, since there was no change in $\rho(300K)$ by the postannealing within a measurement accuracy. For $x = 0$, although the as-grown crystal showed an anomaly due to the magnetostructural transition at 197 K, the annealed crystal exhibited a sharper transition at 204 K, which is consistent with the magnetic susceptibility measurement in Fig. 3.21. The residual resistivity ratio (RRR) $\rho_{300\mathrm{K}}/\rho_{4.2\mathrm{K}}$ is also changed from 3 to 10 after the postannealing. The annealing treatment clearly reduced the residual resistivity, indicating that the impurity or disorder within the crystals was removed by this treatment. This behavior is consistent with the theoretical calculation that the impurity scattering reduces the magnetic transition temperature [69]. Also, for $x = 0.10$ and 0.25, the residual resistivity clearly decreases and T_{AFO} is increased after the annealing treatment [Figs. 3.17(b) and 3.17(c)]. For $x \geqq 0.35$, at which the magnetostructural transition completely disappears, the reduction in the residual resistivity was smaller than that for $x \leqq 0.30$. These indicate that the transport property is more sensitive to the annealing treatment in the AFO phase than in the PT phase.

For $x = 0.35$, the T-linear behavior of resistivity is observed, which suggests a non-Fermi liquid state due to a strong spin fluctuation. Actually, at this composition, $(T_1T)^{-1}$ is strongly enhanced at low temperatures, where T_1 is the spin-lattice relaxation rate in nuclear magnetic resonance (NMR) [70, 71]. With further P-doping, $\rho(T)$ changed to the Fermi-liquid-like T^2 dependence. Moreover, the enhancement of $(T_1T)^{-1}$ was not observed at $x = 0.50$. These results suggest that a two-dimensional antiferromagnetic quantum critical point exists at approximately $x = 0.35$ in P-Sr122. Similar quantum critical behaviors were also reported in the P-Ba122 [23] and P-Eu122 [49], indicating that such a quantum criticality is a common feature in P-doped 122 system.

On the other hand, the unusual annealing effect is found in the underdoped region. Figures 3.18 show $\rho(T)$ of P-Sr122 with $x = 0.28$ and P-Ba122 with $x = 0.20$ for the as-grown and annealed crystals. The measurement was performed on the same crystals before and after annealing. In both systems, T_{AFO} increases by the post-annealing treatment, while T_c estimated from the onset and the zero-resistivity temperature decreases in contrast to the overdoped crystals shown in Figs. 3.17. The smaller normalized $\rho(T)$ above T_c in the annealed crystals than in the as-grown one suggests that disorders in the crystals are reduced by the annealing treatment. These results indicate that T_c in the coexistence region of AFO/SC phase and pure SC phase show a different response to disorders both in P-Sr122 and P-Ba122.

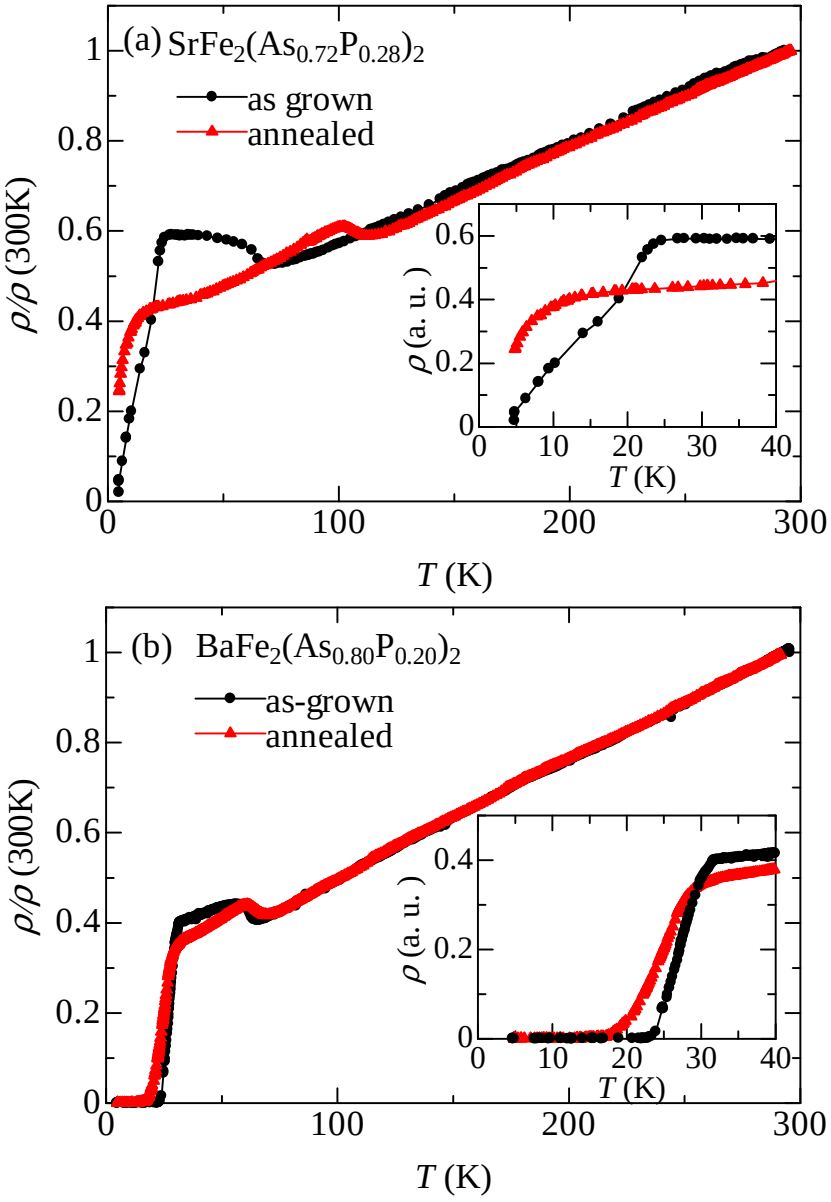

Figure 3.18: (a)-(b) Temperature dependence of resistivity before (black circles) and after annealing (red triangles) for P-Sr122 with $x = 0.28$ and P-Ba122 with $x = 0.20$ respectively. The inset shows ρ around T_c.

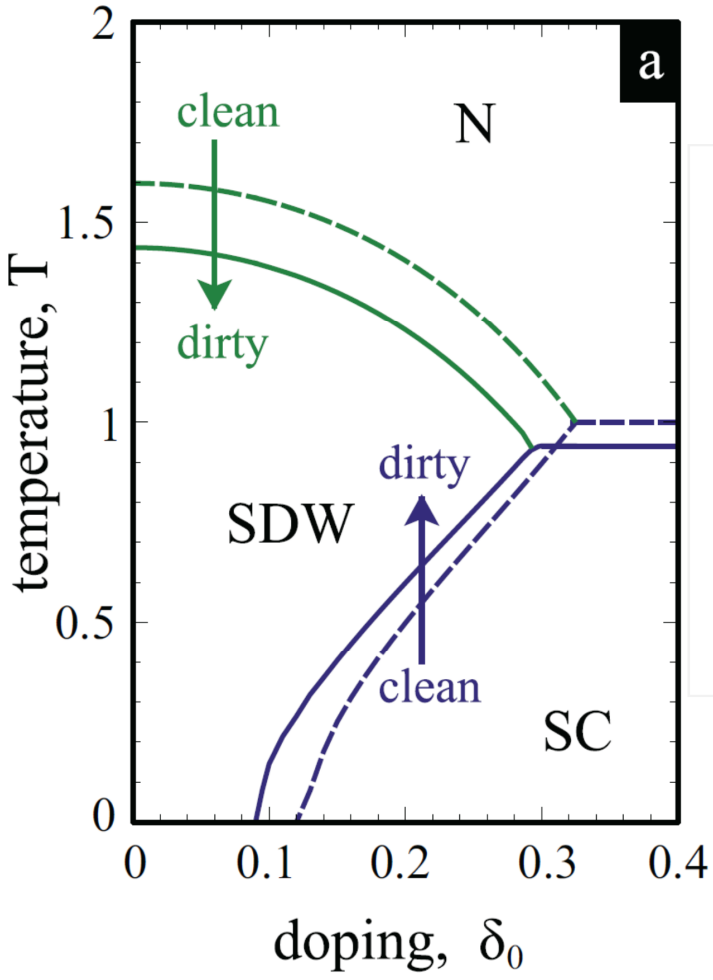

Figure 3.19: Temperatures of normal (N)-to-SDW, SDW-to-SC, and N-to-SC phase transitions as functions of doping for the clean and dirty cases (dashed and solid lines, respectively). The figure is cited from Ref. [69].

The different response of T_c to disorders in the underdoped and the overdoped region has been predicted by the theory based on $s_\pm$ SC state [69] as shown in Fig. 3.19. According to this theory, the different response derive from two competing effects of the direct pair-breaking by impurities, which reduces T_c, and the suppression of the coexisting antiferromagnetic order parameter, which increases T_c. Thus my observation is consistent with the theoretical prediction of $s_\pm$ SC state.

It is noted that $\rho(T)$ of $x = 0.30$ shows a different behavior from that of $x = 0.28$, where the postannealing treatment results in increasing both $T_{\rm AFO}$ and T_c as shown in Fig. 3.17(d). One possible reason of this result is due to the measurement of the different crystals before and after the postannealing treatment. Another reason is that the response of $T_{\rm AFO}$ and T_c to disorder depends on the parameter sets of intraband/interband scattering rates and the strength of disorder [69].

To obtain further information on the electronic state, I studied the Hall effect in P-Sr122 with $x = 0$ and 0.35. Figure 3.20 shows the magnetic field dependence of the Hall resistivity $\rho_{xy}(H)$ and the temperature dependence of the Hall coefficient $R_{\rm H}(T)$ for $x = 0$ and 0.35. $R_{\rm H}(T)$ was estimated by polynomial fitting with $\rho_{xy} = R_{\rm H}H + \alpha H^3$. For $x = 0$ [Figs. 3.20(a) and 3.20(b)], the absolute value of $\rho_{xy}(H)$ decreases and deviates from the H-linear dependence below $T_{\rm AFO}$ after the annealing treatment. A similar result was reported in a previous study of the annealed $BaFe_2As_2$ [68]. However, the H dependence of ρ_{xy} is weaker in the annealed $SrFe_2As_2$ than in the annealed $BaFe_2As_2$. This may be caused by the smaller RRR of the annealed $SrFe_2As_2$ (RRR$\sim$10) than of the annealed $BaFe_2As_2$ (RRR$\sim$ 30) [68]. In Figs. 3.20(c) and 3.20(d) for $x = 0.35$, $\rho_{xy}(H)$ shows an H-linear dependence and little change with postannealing, which is consistent with the annealing effect on $\rho(T)$ shown in Fig. 3.17.

In Fig. 3.20(e), the estimated $R_{\rm H}(T)$ value for $x = 0$ and 0.35 are plotted. For $SrFe_2As_2$, $R_{\rm H}(300\,{\rm K})$ is negative, indicating that the dominant carriers are electrons. At approximately $T_{\rm AFO}(\sim 200\,{\rm K})$, $R_{\rm H}(T)$ changes its sign. Such a sign change of $R_{\rm H}$ is absent in $BaFe_2As_2$ where $R_{\rm H}(T)$ abruptly decreases at $T_{\rm AFO}$ [72], while it was present in $EuFe_2As_2$ and $CaFe_2As_2$ [73, 74]. Such a behavior may be ascribed to the presence of the Dirac fermion [75], which was observed in $SrFe_2As_2$ by quantum oscillation measurement [76]. $R_{\rm H}(T)$ markedly decreases below $T_{\rm AFO}$, and the absolute value of $R_{\rm H}(T)$ at the lowest temperature is 24 times larger than that at room temperature, indicating that the carrier reduction is caused by the reconstruction of

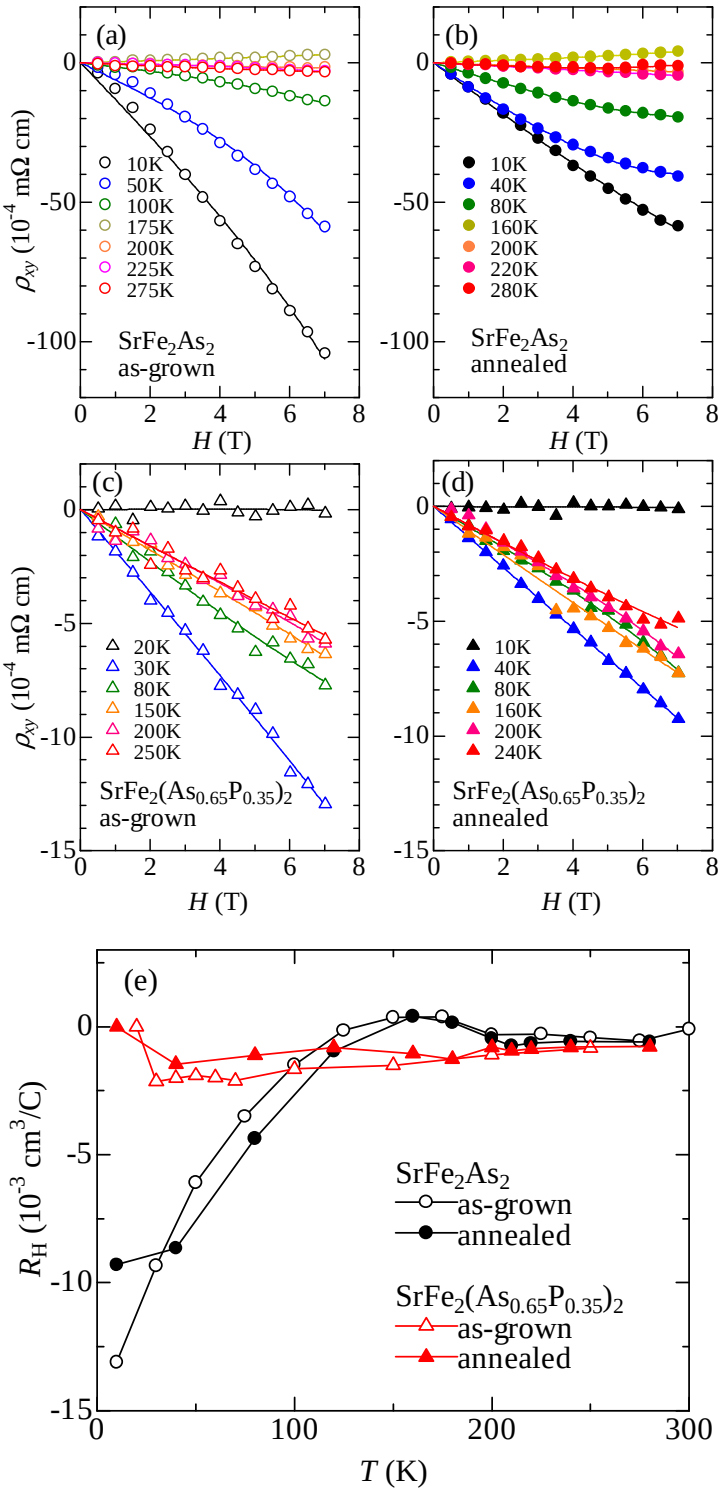

Figure 3.20: (a)-(d) Magnetic field (H) dependence of the Hall resistivity (ρ_{xy}) of as-grown and annealed single crystals for $x = 0$ and 0.35, respectively. The solid lines indicate the fitting results by the formula $\rho_{xy} = R_H H + aH^3$. (e) Temperature dependence of Hall coefficient R_H of as-grown (open symbols) and annealed (closed ones) single crystals for $x = 0$ (circles) and 0.35 (triangles), respectively. The solid lines are visual guides.

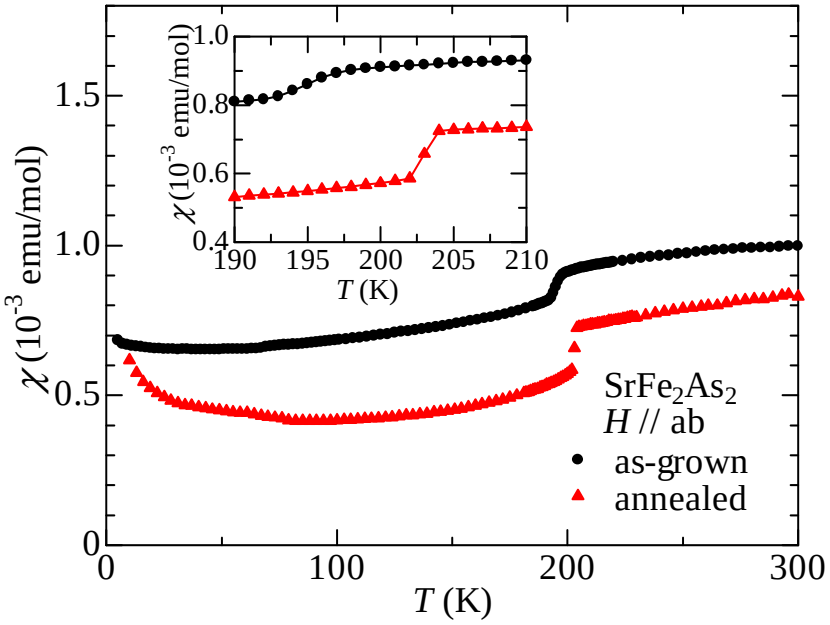

Figure 3.21: Temperature dependence of the magnetic susceptibility χ before and after annealing for $x = 0$. The inset shows χ around T_{AFO}.

the Fermi surfaces in the AFO phase. Although the carrier concentration is reduced, the resistivity shows a sharp decreases at T_{AFO} and maintains a metallic behavior, as shown in Fig. 3.17. This reflects the multicarrier nature of iron pnictides. For $x = 0.35$, although the magnetostructural transition completely disappears, the absolute value of $R_{\mathrm{H}}(T)$ is slightly enhanced by a factor of 2 as the temperature decreases. This may be caused by the multi-band effect [72] or the vertex correction due to antiferromagnetic fluctuation [77].

3.5 Magnetic susceptibility measurement

Figure 3.22 shows the temperature dependence of the magnetic susceptibility $\chi(T)$ of as-grown and annealed $SrFe_2As_2$. The antiferromagnetic transition occurred at $T_{\mathrm{AFO}} = 197\,\mathrm{K}$ in the as-grown crystal as reported previously [78]. After the annealing treatment, T_{AFO} was raised up to 204 K and the transition got sharper as displayed in the inset.

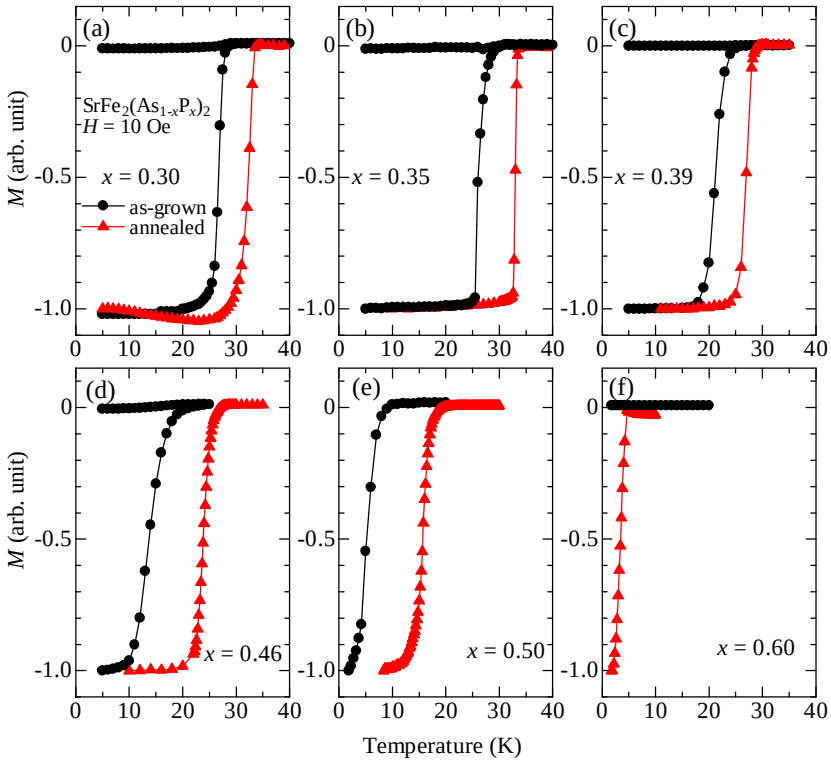

Figure 3.22: (a)-(f) Temperature dependence of magnetization M before and after annealing for $x = 0.30$, 0.35, 0.39, 0.46, 0.50, and 0.60 in magnetic field $H = 10\,\mathrm{Oe}$, respectively.

The annealing effect on T_c was examined by magnetization M measurement for $SrFe_2(As_{1-x}P_x)_2$ ($0.30 \leqq x \leqq 0.60$), as displayed in Fig. 3.22. The value of M is normalized by the absolute value at the lowest measured temperature. T_c clearly increased by the postannealing treatment for all the compositions shown here. For $x = 0.30$ and 0.35, T_c reached 33 K that is the highest value of T_c among those of P-A122 (A =Ba, Sr, Ca and Eu) [23, 64, 65, 62]. For $x = 0.39, 0.46$ and 0.50, T_c increased nearly 10 K by post-annealing. More surprisingly, for $x = 0.60$, the annealed crystal showed a superconducting transition at 5 K, while the as-grown one did not exhibit a diamagnetic signal down to 1.8 K. I emphasizes that these behaviors cannot be due to the variation of P-contents x because the observed change of lattice constants by the post-annealing treatment is not different from that of the x dependence of lattice constants.

3.6 Electronic phase diagram

The electronic phase diagram obtained from the susceptibility and resistivity measurements is shown in Fig. 3.23. Roughly speaking, this is the same as the general phase diagram observed in AFe_2As_2 compounds. Namely, with P-substitution, the magnetostructural transition is gradually suppressed and completely disappears at $x = 0.35$, while the superconductivity emerges above $x = 0.25$. For the as-grown crystals, $T_{c,optimal} = 26$ K and the superconductivity disappears above $x = 0.60$. When the crystals are postannealed, $T_{\rm AFO}$ increases and the superconducting dome is enlarged. For $x = 0.35$, the optimal T_c is enhanced to 33 K by postannealing. The obtained optimal T_c is as high as that of the physical-pressure-induced superconductivity in $SrFe_2As_2$ and higher than that (30 K) of $BaFe_2As_2$ [79, 22]. This means that the chemically and physically pressured Sr122 has a higher optimal T_c than of Ba122. In the annealed sample with $x = 0.60$, both zero resistivity and a diamagnetic signal were observed at approximately 5 K, while the as-grown crystal showed no superconductivity signature down to 1.8 K. The results indicate that the superconducting region is widened beyond $x = 0.60$ by the annealing treatment.

The phase diagram for the as-grown crystals shows a smaller superconducting dome than that of P-Ba122. This seems to be ascribed to the more three-dimensional structure and the Fermi surface topology in P-Sr122 than in P-Ba122. However, after the postannealing treatment, the obtained T_c

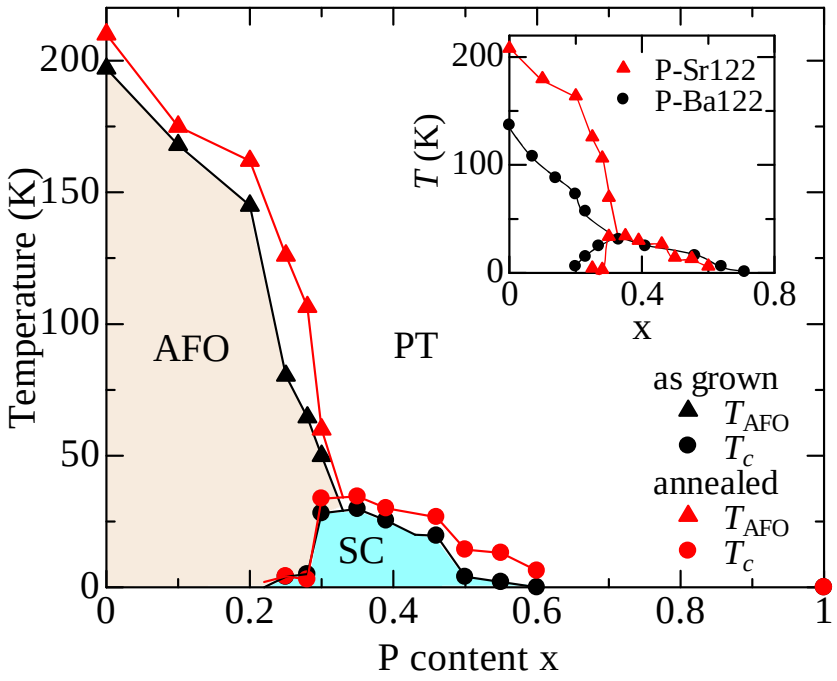

Figure 3.23: Phase diagram obtained from the as-grown and annealed single crystals of $SrFe_2(As_{1-x}P_x)_2$. T_{AFO} is defined as the temperature at which resistivity shows an anomaly due to the phase transition to the AFO state. T_c is defined as the temperature of zero resistivity. The inset compares the phase diagrams of annealed P-Sr122 and P-Ba122 systems. The data of P-Ba122 is cited from previous study by Nakakjima *et al.* [62].

dome is enlarged and very similar to that of P-Ba122, despite the large difference in the a and c-axes lattice constants. This is in contrast to the case of P-A122 (A=Eu and Ca). The recent photoemission measurement has revealed that the hole Fermi surface with the d_{z^2} orbital character is strongly warped along the k_z-direction in P-Sr122 [66]. The more three-dimensional electronic state realized in P-Sr122 should result in the worse Fermi surface nesting than that in P-Ba122, and thus a lower T_c if the nesting condition is crucial for superconductivity. Nevertheless, the optimal T_c of P-Sr122 is nearly the same or even slightly higher than that of P-Ba122. This indicates that T_c is rather insensitive to the crystal structural anisotropy c/a and the dimensionality of the electronic structure.

In contrast to the large difference in the lattice constants, the pnictogen heights are nearly the same in the optimal doped P-Sr122 and P-Ba122 ($x \sim 0.3$), $h_{\mathrm{Pn}} \sim 1.32$ Å[23] as shown in Fig. 3.16(d). In FeSC, it is well known that the pnictogen height and As-Fe-As bond angle correlate with T_c [38, 39]. I found that the postannealed P-Sr122 has a longer pnictogen height and cleaner electronic state than the as-grown one. The close relationship between the superconductivity and the pnictogen height has been explained by the theory based on antiferromagnetic fluctuation mechanism [80]. This theory predicts that the reduction in the a and c-axes lattice constants generally decreases T_c, while the elongation of h_{Pn} enhances it. This difference comes from that the h_{Pn} affects the appearance of the Fermi surface around (π, π) in the unfolded Brillouin zone, while the lattice constant a and c relate with the electron correlation within d_{XZ}/d_{YZ} and $d_{X^2-Y^2}$ orbitals, respectively. The change of different structural parameters affects the spin fluctuation in a different manner, resulting in a different response of T_c. The present results demonstrate that the latter factor (h_{Pn}) is more important than the former (a and c) for superconductivity, which gives some constraints on the theory of superconductivity in FeSC.

3.7 Specific heat in superconducting state

To obtain more information of SC phase, I performed the specific heat measurement. In Fig. 3.24(a), I plotted the temperature dependence of specific heat $C(T)$ divided by T. In order to subtract a phonon contribution, I used the phonon specific heat of non-superconducting $SrFe_2As_2$ and $SrFe_2P_2$. The phonon terms of specific heat for these end members

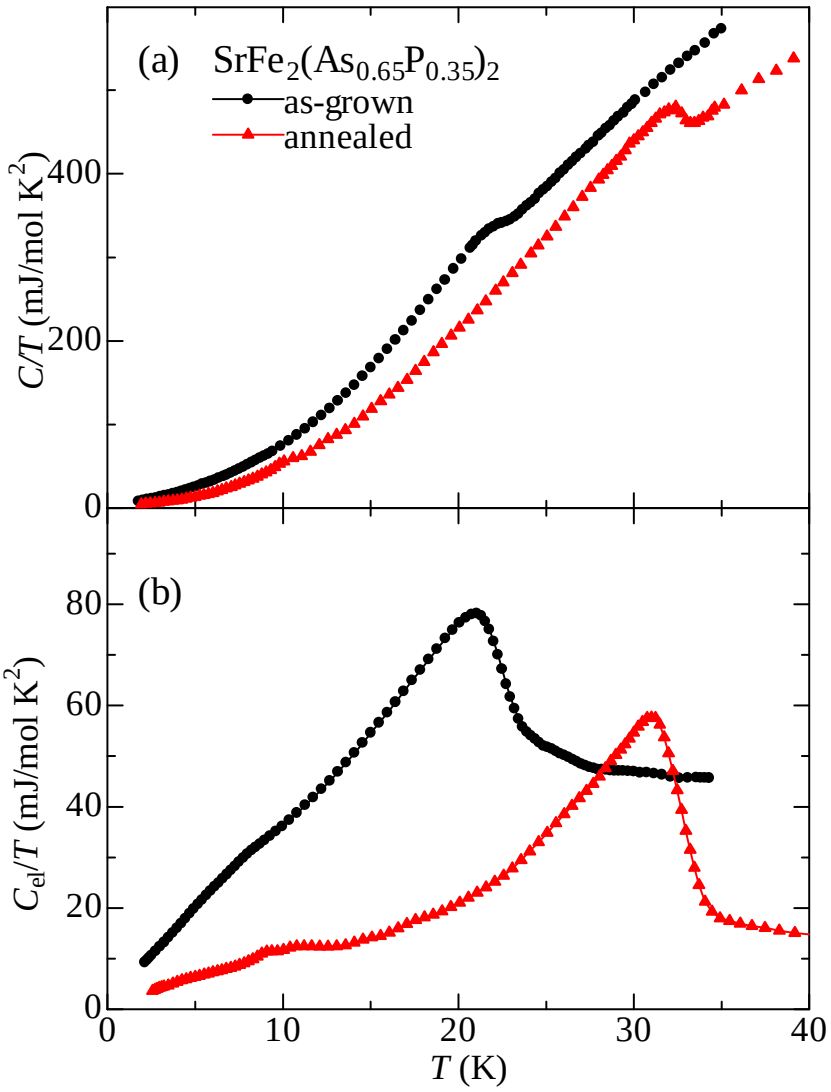

Figure 3.24: (a) The temperature dependence of C/T for the as-grown (black circles) and the annealed (red triangles) $SrFe_2(As_{0.65}P_{0.35})_2$. (b) The temperature dependence of C_{el}/T for as-grown and annealed crystals.

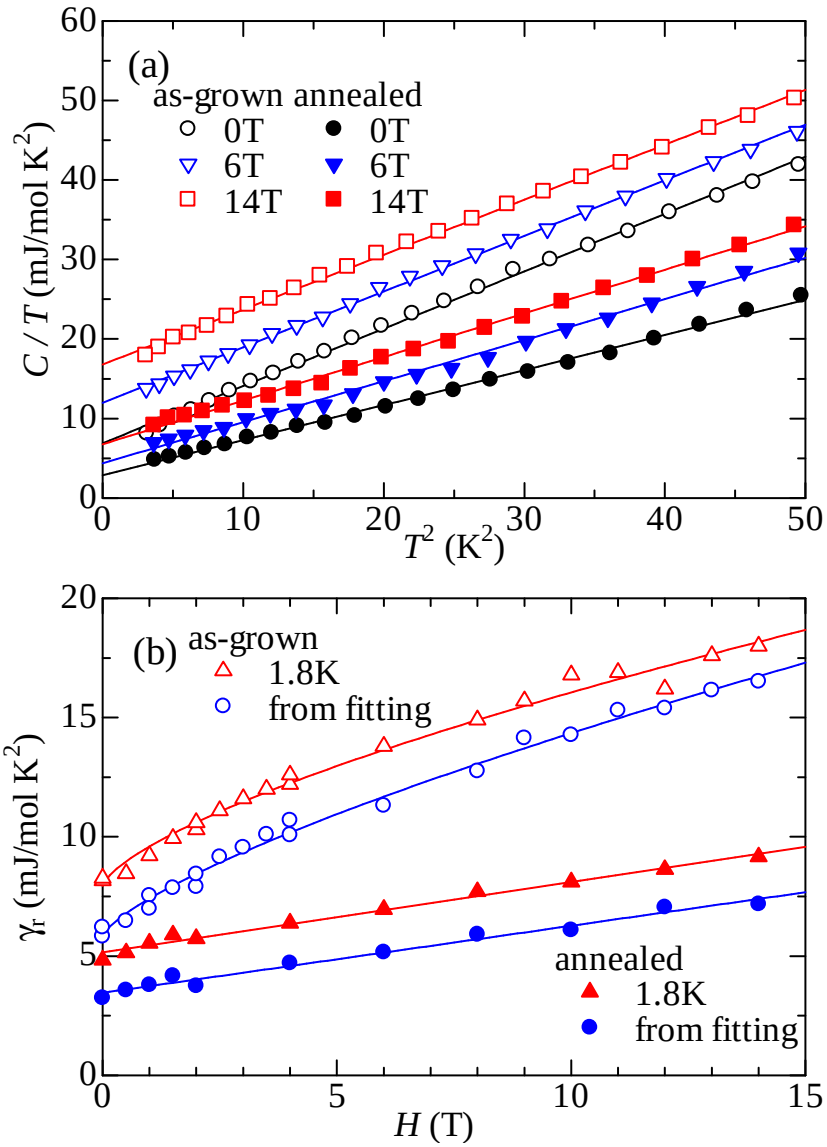

Figure 3.25: (a) The low-temperature specific heat of the as-grown and annealed $SrFe_2(As_{0.65}P_{0.35})_2$ measured at different magnetic fields applied along the c axis. (Circles: 0 T; triangles: 6 T; squares: 14 T; and open and closed symbols represent the data of the as-grown and the annealed samples, respectively.) (b) The magnetic-field dependence of the residual electronic specific heat coefficient γ_r. Red triangles and blue circles correspond to γ_r at 1.8 K and γ_r from $C/T = \gamma_r + \beta T^2$, respectively. The solid lines show $\gamma_r \propto H^{0.7}$ for the as-grown crystal and $\gamma_r \propto H$ for the annealed crystal.

($C_{\mathrm{phonon(SrFe_2As_2/SrFe_2P_2)}}$) were estimated by the formula of $C_{\mathrm{phonon(SrFe_2As_2/SrFe_2P_2)}} = C - \gamma_{\mathrm{(SrFe_2As_2/SrFe_2P_2)}}T$. Here, C and $\gamma_{\mathrm{(SrFe_2As_2/SrFe_2P_2)}}$ are total specific heat and electronic specific heat coefficient for these compounds, respectively. For the annealed crystal, C_{phonon} was calculated as a combination of the values of $SrFe_2As_2$ and $SrFe_2P_2$,

$$C_{\mathrm{phonon}} = 0.7 \times C_{\mathrm{phonon(SrFe_2As_2)}} + 0.3 \times C_{\mathrm{phonon(SrFe_2P_2)}},$$

while C_{phonon} was assumed to be equal to $C_{phonon(\mathrm{SrFe_2As_2})}$ for the as-grown crystal. Figure 3.24(b) shows only the extracted electronic component of C/T. Here, C_{el} for $SrFe_2(As_{0.65}P_{0.35})_2$ is estimated by the formula of $C_{el} = C - C_{\mathrm{phonon}}$. A jump due to superconducting transition was observed at 23 K for the as-grown crystal and a sharper jump at 33 K for the annealed crystal. The normal state Sommerfeld coefficient also changed from 47 mJ/mol K^2 to 17 mJ/mol K^2 by annealing. It seems that the post-annealing suppresses the mass enhancement. However, such a large change of the normal state Sommerfeld coefficient by the annealing treatment was not observed in the previous study of annealed Co-doped $BaFe_2As_2$ (Co-Ba122) [81]. Therefore, I cannot rule out the possibility that the observed change in Sommerfeld coefficient is artificial by the inappropriate subtraction of the phonon contribution. $\Delta C/T_c$ was 40 mJ/mol K^2 and 50 mJ/mol K^2 for the as-grown and the annealed crystals, respectively. Here, ΔC is the change of electronic specific heat due to superconducting transition. The present value of $\Delta C/T_c$ is still smaller than the general value of FeSC [82], indicating that the further improvement of the sample quality may be possible.

In order to discuss a superconducting gap structure, I examined the magnetic field dependence of C/T at 0 K, γ_r(H). Although in principle the presence of gap node can be discussed from low-T $C(T)$ without magnetic field, it is usually difficult to identify the T^2 term which is expected for the superconductor with line node because of the large phonon component [83]. Figure 3.25(a) shows the temperature dependence of C/T at different magnetic fields applied along the c-axis. In Fig. 3.25(b) is plotted the field dependences of residual C/T, the values at 1.8 K and the extrapolated values at 0 K with $C/T = \gamma_r + \beta T^2$. The phonon coefficient β also changed from 0.79 mJ/mol K^4 to 0.36 mJ/mol K^4 by annealing, while residual term γ_r decreased from 5.5 mJ/mol K^2 to 3.6 mJ/mol K^2 by annealing at H=0. This reduction in γ_r implies a decrease of residual density of states which originates from impurity or disorder. However, the γ_r of the annealed crystal is

still larger than that of P-Ba122 (γ_r=1.7 mJ/mol K^2)[84], indicating a larger residual density of state below T_c.

As shown in Fig. 3.25(b), the field dependence of γ_r follows $\gamma_r \propto H^{0.7}$ for the as-grown case, while the post-annealing treatment results in a moderate field dependence, $\gamma_r \propto H$.

The change from the sub-linear to the H-linear dependence of γ_r seems to indicate that the superconducting gap structure became a full gap after annealing. This behavior is consistent with the theoretical calculation of the $s_{\pm}$-wave superconducting state by Bnag [85] as shown in Fig. 3.26. In the the theoretical calculation based on the two band model [85], it is argued that the Doppler shift of the quasiparticle excitations in the superconducting state is caused by applying the magnetic field. When the Doppler shift energy becomes larger than the smaller gap size (Δ_S) while it is smaller than the larger gap one (Δ_L), the smaller gap collapses to create a finite density of state, resulting in the H-linear dependence of specific heat. This H-linear dependence of γ_r changes to a sub-linear H dependence when disorders are introduced in a full gap $s_{\pm}$-wave superconducting state. In addition, the impurity scattering in the $s_{\pm}$-wave superconducting state efficiently leads to zero energy impurity band near Fermi level and the finite $\gamma_r(0\,K)$ as observed in the present study. Therefore, my observation can be understood within a full gap $s_{\pm}$ regime. I note that the similar annealing effect on γ_r(H) was observed in Co-Ba122[81].

On the other hand, the penetration depth measurement performed by Murphy *et. al.* [86] gave a different result. The observed $\Delta\lambda(T)$ was T-linear in the annealed crystal, while $\Delta\lambda(T)$ followed T^n $(n < 2)$ in the as-grown crystal. This change of exponent n can be understood within a framework of nodal superconductor by assuming that the as-grown crystals was in a dirty limit, while the annealed one was in a clean limit. Considering all these results, I speculate that the Fermi surface with a heavier carrier mass has a full gap and dominates the specific heat, while the others with a lighter carrier mass have a nodal gap which governs the penetration depth. Here I note that the H-linear dependence of γ_r was also observed in P-Ba122 where one Fermi surface has a full gap and the others have nodes [84].

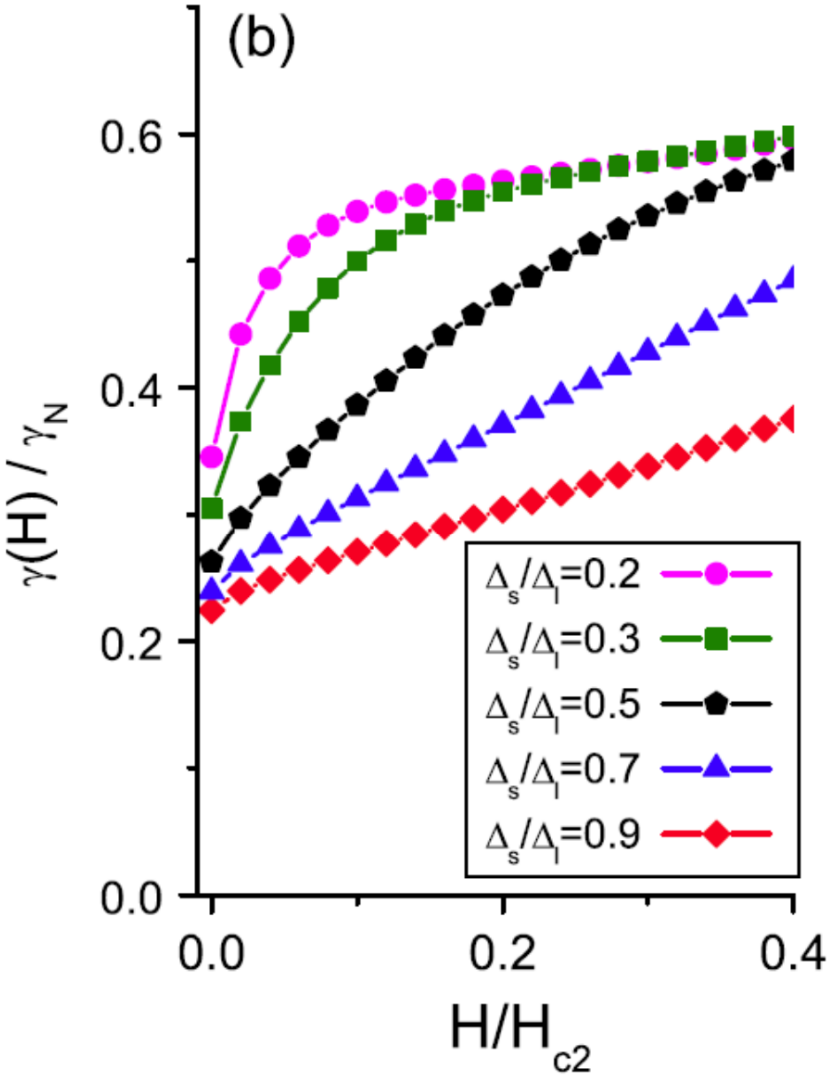

Figure 3.26: Normalized specific heat coefficient for different gap size ratios at 0 K. All calculations include the same concentration of impurities $\Gamma/\Delta_L = 0.05$ ($\Gamma \propto n_{\mathrm{imp}}$, n_{imp}; impurity concentration). This means that this gap size dependence is the same as n_{imp} dependence ($\Delta_S/\Delta_L \sim \Delta_S/\Gamma$). The figure is cited from Ref. [85].

3.8 Summary

I have successfully grown single crystals of $SrFe_2(As_{1-x}P_x)_2$ over the entire range of x and performed a systematic study of its electronic properties as well as of the annealing effects. The annealing treatment reduced the residual resistivity, increases $T_{\rm AFO}$, decreased T_c in the underdoped region, and increased T_c in the overdoped region. Using the annealed crystals, I have established the intrinsic phase diagram that was quite similar to that of P-Ba122 despite the large difference in the a and c-axes lattice constants. The similarity between the two systems has been attributed to the nearly identical pnictogen height, which dominates the electronic properties of iron pnictides. The dimensionality of the Fermi surface is a less important factor for determining T_c.

I also studied the annealing effect on specific heat and a precise x-ray diffraction analysis. I found that T_c is enhanced up to 33 K that is higher than the value of optimal P-Ba122. I have found that there are two effects of post-annealing. One is the elongation of the c-axis and the pnictogen height in the average crystal structure. This causes the enhancement of T_c in the annealed crystals. The other effect is to reduce disorders within crystals, which is clearly observed in specific heat. This suggests that the system changes from a dirty to clean superconductor with the $s_\pm$ full gap on the Fermi surface with a heavier carrier mass.

Part IV

In-plane resistivity anisotropy of $Ba(Fe_{1-x}TM_x)_2As_2$ (TM=Cr, Mn, and Co)

4.1 Introduction

In almost all iron pnictides, the terminal compositions, $BaFe_2As_2$ and LaFeAsO, undergo a structural and magnetic phase transition from a higher-temperature paramagnetic-tetragonal (PT) state to a lower-temperature antiferromagnetic-orthorhombic (AFO) one with decreasing temperature. By substituting various elements or applying pressure, the AFO state is suppressed and superconductivity emerges. One of the puzzles in the normal-state properties is the anomalous electronic anisotropy in the AFO and paramagnetic-orthorhombic phases [43, 44]. Although the anisotropy in the paramagnetic-orthorhombic phase, which is the so-called nematic phase [19, 45, 87, 88], has attracted much interest in terms of the nematic nature of the electronic state, the anisotropy in the AFO phase is also unusual. Particularly, the in-plane resistivity shows significant anisotropy in the AFO phase at low temperatures [45]. The resistivity along the longer a-axis with an antiferromagnetic spin arrangement (ρ_a) is smaller than that along the shorter b-axis with a ferromagnetic spin arrangement (ρ_b). This observed anisotropy ($\rho_b > \rho_a$) is counterintuitive because both of the larger orbitals overlap due to a smaller lattice constant and smaller spin-fluctuation scattering due to a ferromagnetic spin arrangement, which should give a smaller resistivity in the b-direction ($\rho_b < \rho_a$). Several theories based on magnetic order, orbital order, and lattice distortion have been proposed to explain this anomalous anisotropic resistivity [89, 90, 91, 92, 93, 94]. However, all of them fail to explain the fact that transition metal (TM) substitution for the Fe sites enhances the resistivity anisotropy despite the suppression of the magnetic order, orbital polarization, and lattice orthorhombicity [19, 95].

To understand these counterintuitive behaviors, two different mechanisms have been proposed. One is based on the anisotropy of impurity scattering and the other on the effect of anisotropic Fermi surface topology. The key experimental fact for the first scenario is that the anisotropy of in-plane resistivity in $BaFe_2As_2$ (Ba122) almost disappears after the postannealing treatment, which removes defects in the crystals [68, 96]. It was also pointed out that the anisotropy decreases with increasing distance of the substitution site from the Fe sites [97]. Based on these results, Ishida and co-workers proposed that the anisotropy of impurity scattering by substituted atoms is the origin of the anisotropy of in-plane resistivity, in other words, that the observed anisotropy is an extrinsic property. This scenario is supported by optical [48, 98] and scanning tunnel spectroscopy studies [50, 51, 52], as well

as by theoretical investigations [99, 100, 101].

Another important experimental result for the second scenario is the comparative study of electron-doped $Ba(Fe_{1-x}Co_x)_2As_2$ (Co-Ba122) and hole-doped $(Ba_{1-x}K_x)Fe_2As_2$ (K-Ba122). The difference of resistivity ($\Delta\rho = \rho_b - \rho_a$) is smaller in K-Ba122 than in Co-Ba122, and more surprisingly, it becomes negative ($\rho_b < \rho_a$) with further K substitution [102, 103]. Theoretically, the reversal of anisotropy has been predicted by considering the change of the Fermi surface topology and Drude weight in the AFO phase [103, 104]. However, they do not explain the postannealing effect, and recently it has been pointed out that the calculated anisotropy of the Drude weight is inconsistent with the experimental results [105]. The mechanism based on spin-fluctuation scattering also takes account of the topology of the Fermi surface [106, 107], but it is applicable only in the nematic phase, not in the AFO phase. In addition, some studies have regarded the observed inverse anisotropy as negligibly small, which is due to weak carrier scattering because of the off-site substitution [97, 99, 101]. Thus, the previous studies could not distinguish the two factors of the in-plane resistivity anisotropy because they compared different site-substituted systems, and it turns out that the origin of the in-plane resistivity anisotropy is still controversial.

To distinguish the roles of the impurity scattering and the band structure, a comparative study using materials in which holes and electrons are doped by chemical substitution at the same atomic sites should be performed. In this chapter, I chosed $Ba(Fe_{1-x}TM_x)_2As_2$ (TM-Ba122, TM=Cr, Mn) as the hole-doped systems. Even when holes are doped, they do not show superconductivity and have the same AFO phase in the underdoped region ($x \leqq 0.30$ for Cr and $x \leqq 0.10$ for Mn) as in doped Ba122 [24, 25]. (In the higher-doped region, Cr- and Mn-Ba122 systems show different types of antiferromagnetic order.) Since Cr, Mn, and Co are substituted for Fe, hole-doped TM-Ba122 (TM=Cr and Mn) is a suitable counterpart of the electron-doped Co-Ba122 to discuss the role of impurity scattering and band structure. The purpose of the present work is to clarify the role of the impurity scattering and the topology of the Fermi surface in the in-plane resistivity anisotropy in the AFO and nematic phases of iron pnictide superconductors.

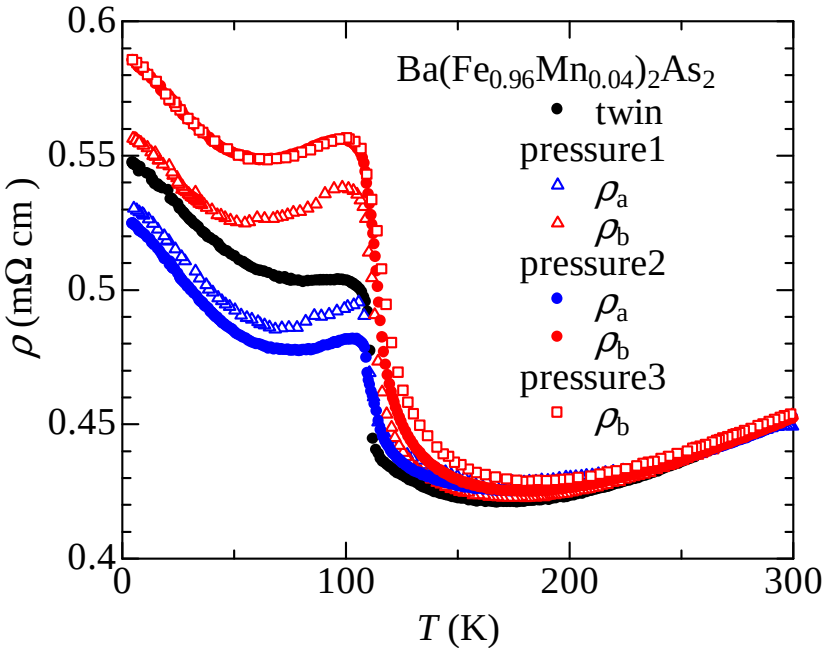

Figure 4.27: Temperature (T) dependence of the in-plane resistivity along a-axis (ρ_a) (blue) and b-axis (ρ_b) (red) of detwinned $Ba(Fe_{0.96}Mn_{0.04})_2As_2$ under different pressures. Triangles indicate the result under the first pressure (Pressure1), circles and squares under larger pressures (Pressure2 and Pressure3), respectively. The largest pressure (Pressure3) data almost completely overlap the second largest pressure (Pressure2) data, suggesting saturation of the effect due to complete detwinning.

4.2 Resistivity measurement with detwinned crystals

The crystals were detwinned by applying mechanical uniaxial pressure with a device displayed in the experimental method. In the AFO phase, the shorter b-axis is naturally aligned in the direction of the applied uniaxial pressure. The measurements of the in-plane resistivity along both a- and b-axes of the orthorhombic lattice were performed on detwinned samples by a standard four-probe method. I repeated the resistivity measurements with increasing pressure and confirmed the saturation of the anisotropy, as shown

in Fig. 4.27.

Figures 4.28(a)-(k) show the temperature dependence of the in-plane resistivity for detwinned TM-Ba122 (TM=Cr, Mn, and Co). All the crystals of TM-Ba122 show the AFO transition, as in Co-Ba122 [24, 25]. Further increases of Cr and Mn content led to other ordered phases, as shown in Figs. 4.28(l) and 4.28(m). In this study, I investigated the resistivity anisotropy in the composition region of $x \leqq 0.24$ for Cr and $x \leqq 0.08$ for Mn.

At room temperature, the resistivity monotonically increases with increasing Cr and Mn content beyond the statistical error, in contrast to the case of Co- and K-Ba122 [97]. This suggests that Cr and Mn atoms in the FeAs plane are stronger scatterers than Co atoms. The resistivity decreases with decreasing temperature down to the magnetostructural transition temperature, $T_{\rm AFO}$. Below $T_{\rm AFO}$, the resistivity increases with decreasing temperature in both Cr- and Mn-Ba122. For $x = 0$ [Fig. 4.28(a)], resistivity anisotropy between $\rho_{\rm a}$ and $\rho_{\rm b}$ is observed only around $T_{\rm AFO}$, as previously reported [68]. For $x = 0.02$ of Cr-Ba122 [Fig. 4.28(b)], $\rho_{\rm b}$ is larger than $\rho_{\rm a}$ below $T_{\rm AFO}$, which is similar to the electron-doped Co-Ba122 shown in Figs. 4.28(j) and 4.28(k). Remarkably, the anisotropy decreases with further Cr substitution, and eventually one can see the crossover from $\rho_{\rm a} < \rho_{\rm b}$ to $\rho_{\rm a} > \rho_{\rm b}$ at low temperatures above $x = 0.09$ [Figs. 4.28(d)-(g)]. On the other hand, in the case of Mn substitution, a clear anisotropic feature of $\rho_{\rm a} < \rho_{\rm b}$ continues up to $x = 0.08$, as shown in Figs. 4.28(h) and 4.28(i).

I summarize the temperature dependence of the in-plane resistivity anisotropy $\Delta\rho(T) = \rho_{\rm b} - \rho_{\rm a}$ for TM-Ba122 (TM=Cr, Mn, and Co) in Fig. 4.29. When the temperature decreases, $\Delta\rho(T)$ starts to increase above $T_{\rm AFO}$ in all the samples, suggesting that the nematic phase is induced by applying pressure in this temperature range [87, 88]. For Cr-Ba122, $\Delta\rho(T)$ at $x = 0.02$ is larger than that at $x = 0$, as shown in Fig. 4.29(a). With further Cr substitution, a maximum $\Delta\rho(T)$ around $T_{\rm AFO}$ decreases but remains positive, whereas $\Delta\rho(T)$ at the lowest temperature has a negative value above $x = 0.09$. As a result, an intersection of $\rho_{\rm a}$ and $\rho_{\rm b}$, namely, $\Delta\rho = 0$, is observed between $T_{\rm AFO}$ and the lowest temperature. This is significantly different behavior from that of Mn- and Co-Ba122, as shown in Figs. 4.29(b) and 4.29(c). In both systems, $T_{\rm AFO}$ is suppressed by the Mn and Co substitution, whereas the anisotropy of the in-plane resistivity, $\Delta\rho$, at the lowest temperature monotonically increases with x below $x = 0.08$ in Mn-Ba122 and below $x = 0.04$ in Co-Ba122. In Mn- and Co-Ba122, $\Delta\rho(T)$ is always positive in all the temperature and composition ranges.

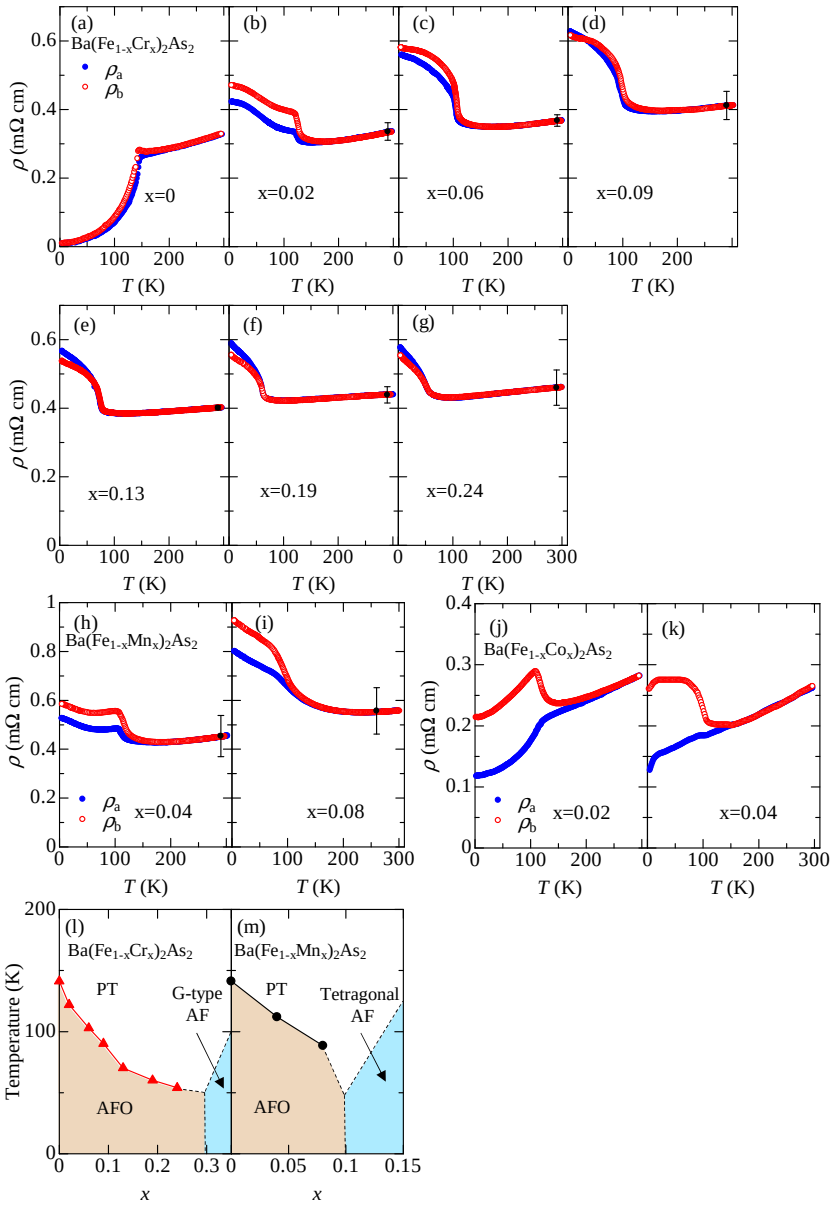

Figure 4.28: Temperature (T) dependence of the in-plane resistivity along the a-axis ($\rho_{\rm a}$) (blue, closed circles) and b-axis ($\rho_{\rm b}$) (red, open circles) of detwinned $Ba(Fe_{1-x}TM_x)_2As_2$ TM=Cr [(a)-(g)], Mn [(h), (i)] and Co [(j), (k)]. Statistical error bars of quantitative resistivity values are shown for $Ba(Fe_{1-x}TM_x)_2As_2$ (TM=Cr and Mn). (l) and (m) show the $T-x$ phase diagram of $Ba(Fe_{1-x}Cr_x)_2As_2$ and $Ba(Fe_{1-x}Mn_x)_2As_2$, respectively. The magnetostructural transition temperatures, $T_{\rm AFO}$, determined from $d\rho(T)/dT$ with twinned crystals, are indicated by triangles in (l) and circles in (m). The Cr-doped system with $x \geq 0.30$ and the Mn-doped one with $x \geq 0.10$ show the magnetic transition to a G-type antiferromagnetic (AF) state and an AF-tetragonal structural state, respectively, as reported in previous studies [24, 25].

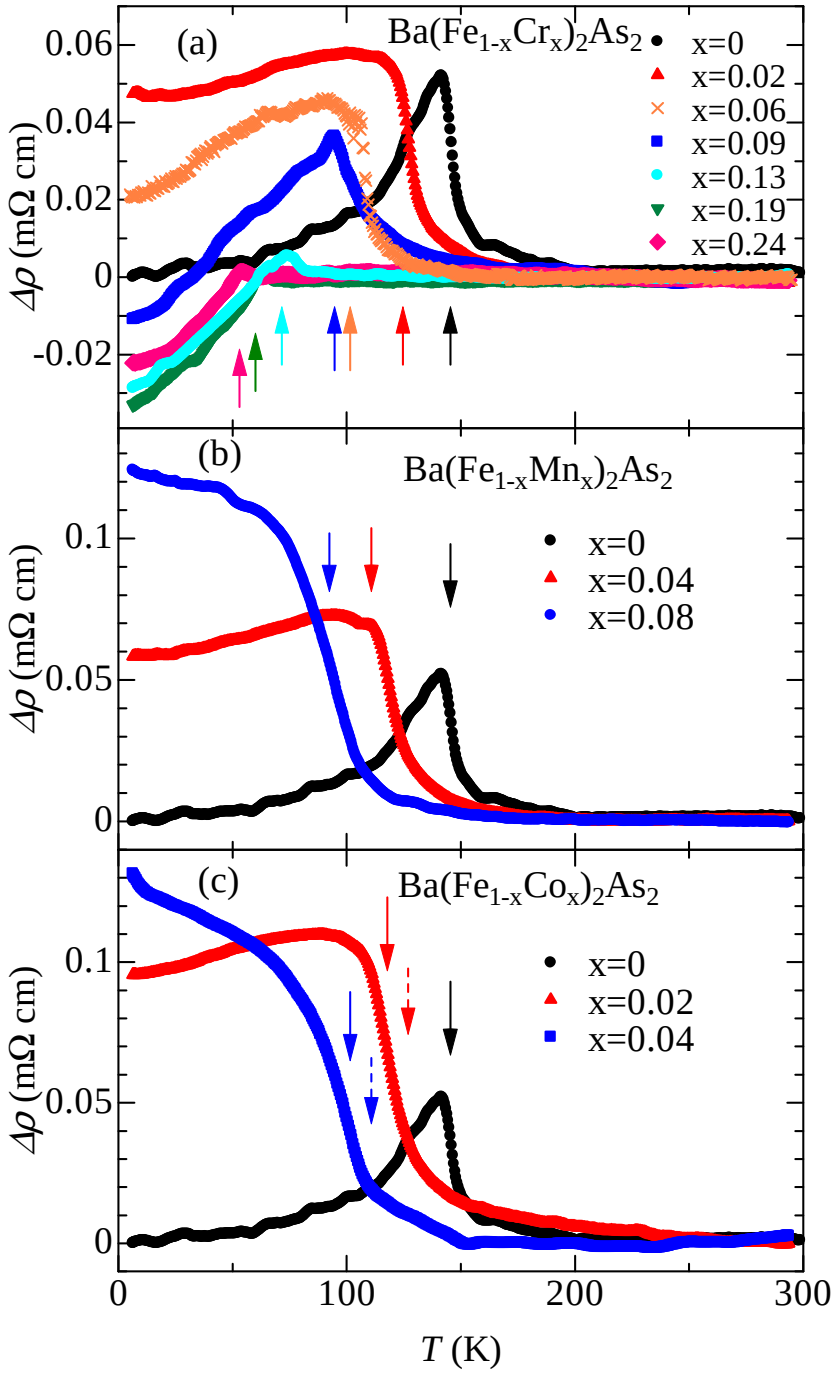

Figure 4.29: Temperature dependence of resistivity difference $\Delta\rho = \rho_{\rm b} - \rho_{\rm a}$ for (a) $Ba(Fe_{1-x}Cr_x)_2As_2$ with $x = 0 - 0.24$, (b) $Ba(Fe_{1-x}Mn_x)_2As_2$ with $x = 0 - 0.08$, and (c) $Ba(Fe_{1-x}Co_x)_2As_2$ with $x = 0 - 0.04$. The arrows in (a) and (b) represent the magnetostructural transition temperature, $T_{\rm AFO}$. The solid and dotted arrows in (c) represent the magnetic and structural transition temperatures, respectively. The magnetic transition coincides with the structural transition in Cr- and Mn-Ba122, whereas the two transitions separate with substitution in Co-Ba122 [24, 25].

4.3 Hall effect in Cr and Mn-Ba122

To clarify the origin of the difference between Cr-Ba122 and Mn-Ba122, I performed Hall resistivity measurements. Figures 4.30(a) and 4.30(b) show the temperature dependence of the Hall coefficient, $R_{\rm H}(T)$, of Cr- and Mn-Ba122, respectively. Above $T_{\rm AFO}$, the sign of $R_{\rm H}(T)$ changes from negative to positive with Cr substitution, whereas $R_{\rm H}(T)$ slightly changes but remains negative with Mn substitution. This suggests that holes are doped by Cr substitution but not by Mn substitution, which will be more clearly discussed later. Around $T_{\rm AFO}$, $|R_{\rm H}(T)|$ abruptly increases due to the reconstruction of the Fermi surface. It is noted that $R_{\rm H}(T)$ below $T_{\rm AFO}$ shows a local minimum or maximum in Cr- and Mn-Ba122, which is different from K-Ba122 [108, 109]. The origin of these temperature dependences may be related to the multi-band effect [110, 111].

4.4 Relation between $R_{\rm H}$ and $\Delta\rho$

Figure 4.31 shows the doping dependence of $R_{\rm H}$ at $T_{\rm AFO}$ and $\Delta\rho = \rho_{\rm b} - \rho_{\rm a}$ at 5 K and $T_{\rm AFO}$. At $T_{\rm AFO}$, $R_{\rm H}$ of Cr-Ba122 increases with x, resulting in a sign change around $x = 0.09$, and almost saturates above $x = 0.13$, while $R_{\rm H}$ of Mn-Ba122 decreases with doping and remains negative. A similar peak structure of $R_{\rm H}$ around $T_{\rm AFO}$ with doping is observed in the hole-doped K-Ba122 [108, 109]. This suggests that the holes are effectively doped into Cr-Ba122 but not into Mn-Ba122. The almost absence of carrier doping in Mn-Ba122 is also suggested by the nuclear magnetic resonance and photoemission measurements [112, 66].

As shown in Fig. 4.31(b), $\Delta\rho(5\,{\rm K})$ for Cr-Ba122 increases with increasing x up to $x = 0.02$ and then decreases above this composition. As a result, $\Delta\rho(5\,{\rm K})$ of Cr-Ba122 shows a sign change at approximately $x = 0.09$. Above $x = 0.13$, it becomes nearly doping independent, corresponding to the saturation of $R_{\rm H}(T_{\rm AFO})$. In contrast to Cr-Ba122, $\Delta\rho(5\,{\rm K})$ of Mn-Ba122 monotonically increases with increasing doping.

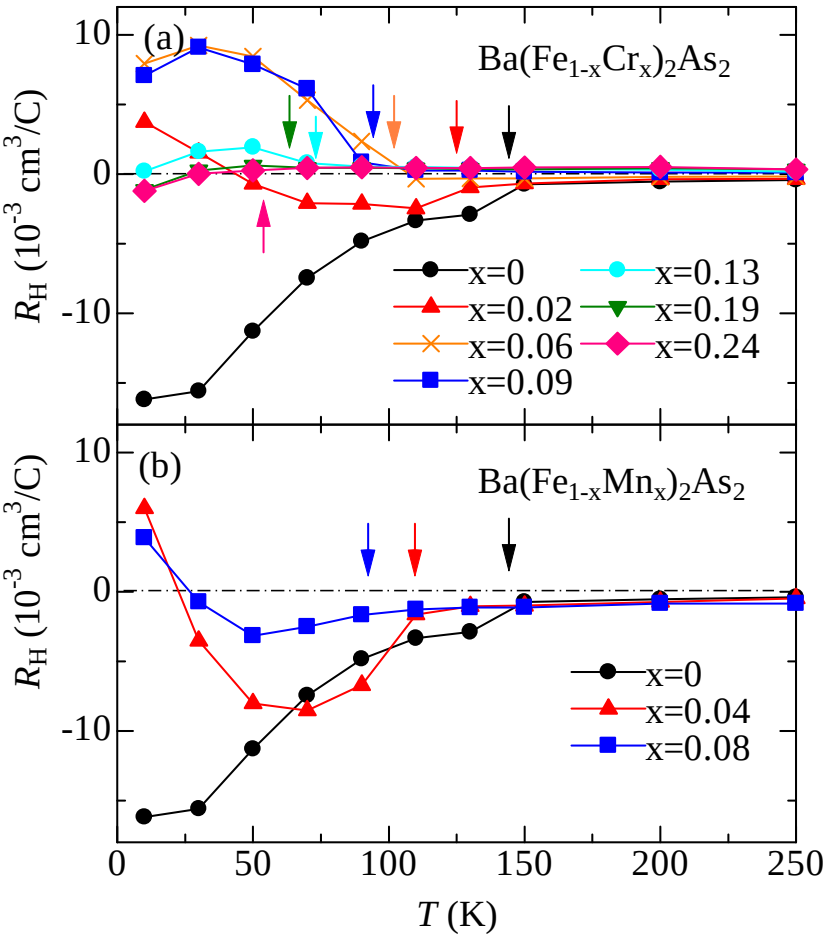

Figure 4.30: Temperature dependence of Hall coefficient $R_{\rm H}(T)$ for (a) $Ba(Fe_{1-x}Cr_x)_2As_2$ and (b) $Ba(Fe_{1-x}Mn_x)_2As_2$. The arrows indicate the position of $T_{\rm AFO}$.

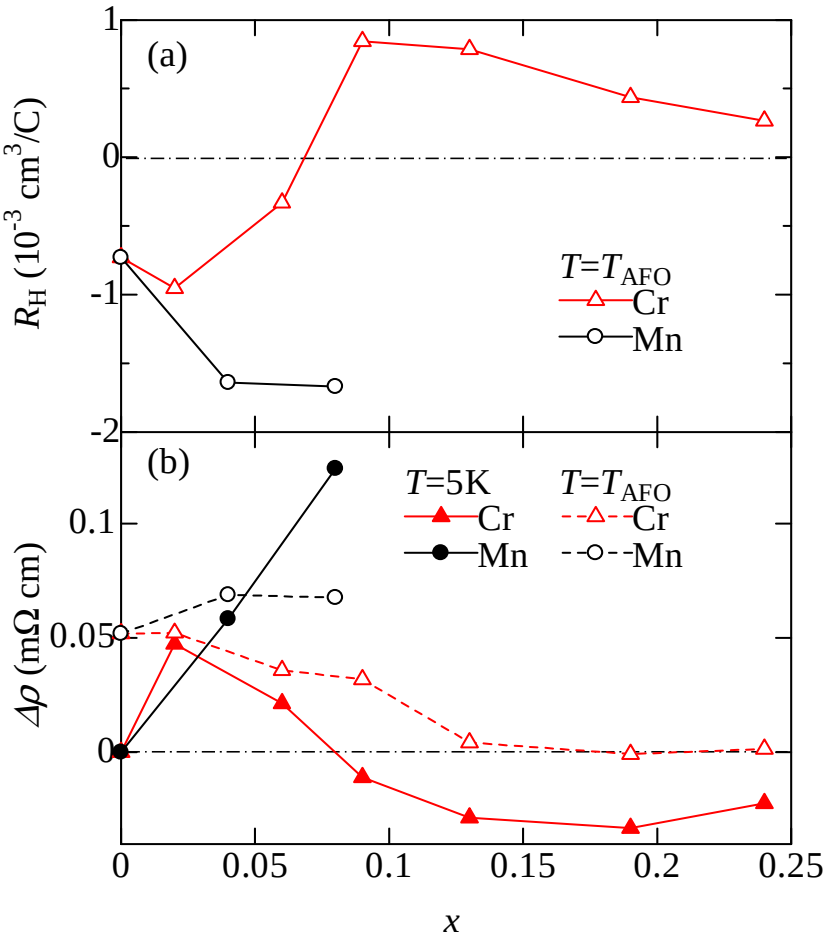

Figure 4.31: The doping (x) dependence of (a) Hall coefficient $R_{\rm H}$ at $T_{\rm AFO}$ (open symbols) and (b) $\Delta\rho = \rho_{\rm b} - \rho_{\rm a}$ at 5 K (closed ones) and $T_{\rm AFO}$ (open ones) for $Ba(Fe_{1-x}TM_x)_2As_2$ [TM=Cr (red triangles) and Mn (black circles)].

4.5 Discussion on the origin of the resistivity anisotropy

There are several possible origins of the difference in $\Delta\rho(T)$ in the AFO phase among Cr-Ba122, Mn-Ba122, and Co-Ba122. One is the crystallographic effect, namely, the change of lattice constants with doping affects $\Delta\rho(T)$. This is unlikely, however, because of the following reason. According to previous studies, the lattice constants of a- and c-axes increase with increasing Cr and/or Mn substitution in Ba122 [113, 114], whereas they decrease with increasing Co substitution [115]. On the other hand, $\Delta\rho(T)$ is similar in Mn-Ba122 and Co-Ba122 but different between Mn-Ba122 and Cr-Ba122. Therefore, there is no correlation between crystallographic change and $\Delta\rho(T)$ in these three systems.

The second possible origin is the difference in carrier scattering. Above T_{AFO}, $\rho(T)$ of Cr-, Mn-, Co-, and K-Ba122 [97] is more or less similar. Below T_{AFO}, however, $\rho(T)$ of Cr-, Mn-, and Co-Ba122 increases upon cooling , whereas $\rho(T)$ of K-Ba122 decreases. This difference originates from the difference in the impurity scattering strength which depends on the substituted element and site. Nevertheless, the difference in carrier scattering cannot explain the difference of $\Delta\rho(T)$. One example is that $\Delta\rho(T)$ of Mn-Ba122 is similar to that of Co-Ba122, despite the different $\rho(T)$, namely, different impurity scattering levels. A similar relation is observed between Cr-Ba122 and K-Ba122. These two compounds show different $\rho(T)$ but similar $\Delta\rho(T)$. Therefore, the impurity scattering strength alone does not determine $\Delta\rho(T)$ in iron pnictides.

The third candidate is the different carrier doping level. The present results can be summarized as follows. The resistivity anisotropy, $\Delta\rho$, in the AFO phase is relatively small and shows a sign change whenever hole carriers are doped into the system, irrespective of the chemical substitution site. This indicates that the size and shape of Fermi surfaces strongly affect the in-plane resistivity anisotropy. Thus, the theories which attribute the small $\Delta\rho$ in K-Ba122 to the absence of strong disorder [99, 100, 101] are inadequate as a general explanation of the in-plane resistivity anisotropy in iron pnictides. Of course, I cannot ignore the impurity scattering effect, considering the annealing effect [68, 96]. Actually, it has been pointed out that the theoretical calculation of conductivity based on the Fermi surface topology alone predicts anisotropy opposite to the observed one [105]. Therefore, it is

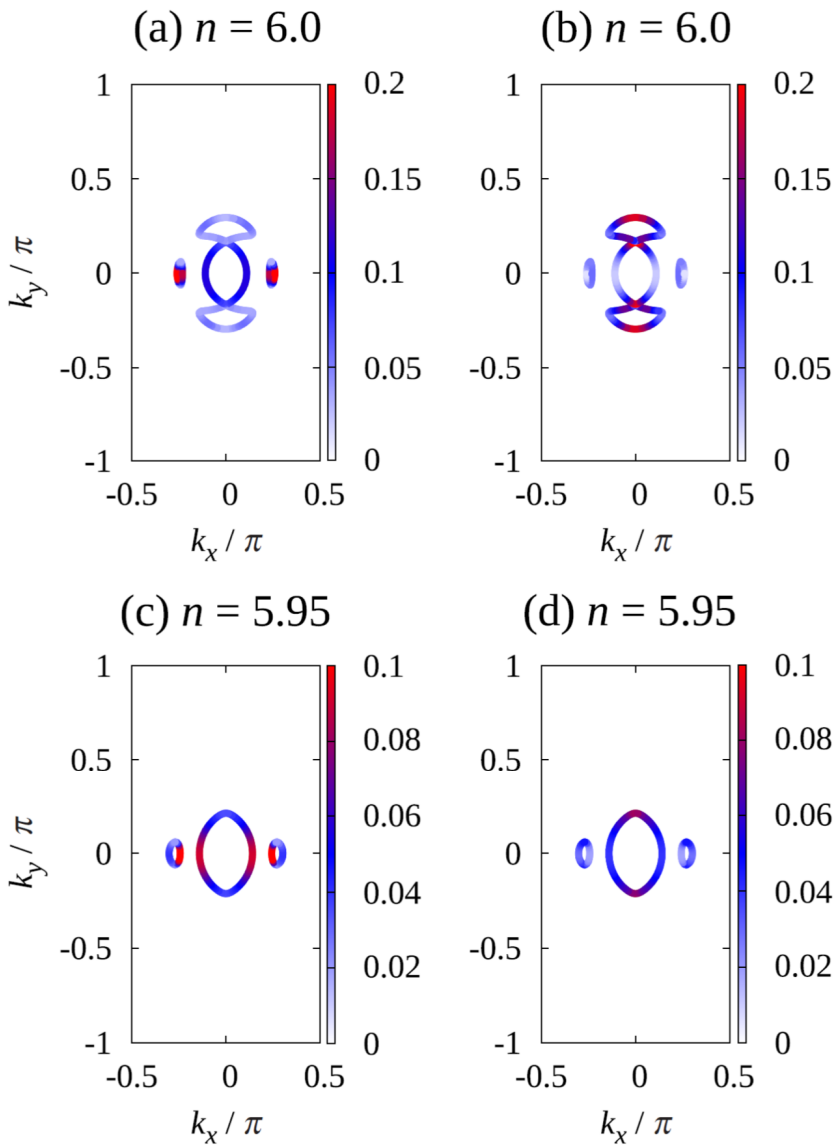

Figure 4.32: The intensity of $\mathrm{Im}M_{\alpha\alpha}(\mathbf{k_0}, 0)/(cI_{imp}^2)$. $\mathrm{Im}M$ is the imaginary part of the memory function which denotes the the momentum dependent contrbution to the impurity scattering. (a) $\alpha = x$ and $n = 6.0$ (parent compound). (b) $\alpha = y$ and $n = 6.0$. (c) and (d): The same as (a) and (b), respectively, but $n = 5.95$ (hole-doped). The figure is cited from Ref. [105].

likely that the anisotropy of resistivity of Ba122 systems in the AFO phase is induced by the anisotropic impurity scattering that reflects the anisotropic electronic state (Fermi surface), as recently proposed [105]. In the theoretical study by Sugimoto *et al*. [105], the in-plane resistivity was calculated by using a memory function approach where the momentum dependent contrbution to the impurity scattering can be clarified. They found that the scattering rate along *a*-axis mainly comes from the Dirac pockets while the electron pockets contributes to the scattering rate along *b*-axis as shown in Fig. 4.32. With increasing hole carrier concentration, the electron pockets disappear and the Dirac pockets governs the scattering rate. The contribution from the impurity scattering to the in-plane resistivity is more than that from the Drude weight. These effects result in the electron-hole asymmetry of the in-plane resistivity anisotropy. This scenario can explain not only the large anisotropy in the electron-doped Co-Ba122, where both electron doping and impurity scattering result in a positive $\Delta\rho$, but also that of Mn-Ba122, where the disorder determines $\Delta\rho$ because the Fermi surface does not change very much due to the absence of carrier doping. In the hole-doped systems, the resistivity anisotropy is intrinsically small and shows a negative $\Delta\rho$, regardless of the impurity scattering strength.

Finally, I discuss the anisotropy at $T > T_{\mathrm{AFO}}$. I can consider the different origin of the resistivity anisotropy below and above T_{AFO} because the AFO and nematic phases have different electronic structures [19, 88]. A small positive $\Delta\rho(T_{\mathrm{AFO}})$ decreases with increasing Cr content in Cr-Ba122, as shown in Fig. 4.31(b). This is similar to the results for K-Ba122 and Na-substituted $CaFe_2As_2$, where a very small $\Delta\rho$ is observed above T_{AFO} [102, 103, 116], but different from the results for the electron-doped Co-Ba122, where a positive $\Delta\rho$ is enhanced with doping [45, 103]. Here again, the behaviors of $\Delta\rho$ are similar among the hole-doped systems but different between the hole- and electron-doped systems, irrespective of the substitution site. Therefore, the impurity scattering caused by the substituted atoms does not play a major role, instead, the change of the Fermi surface by carrier doping is crucial in the resistivity anisotropy above T_{AFO}.

Several theories have been proposed to explain the anisotropy in the nematic phase, such as mechanisms based on impurity scattering with an orbital order [101, 105] or emergent defect states [117]. I cannot support these scenarios based on impurity scattering, however, because it does not explain the observed electron-hole asymmetry in $\Delta\rho$. On the other hand, the spin-fluctuation scattering mechanism [106, 107] predicts the electron-hole

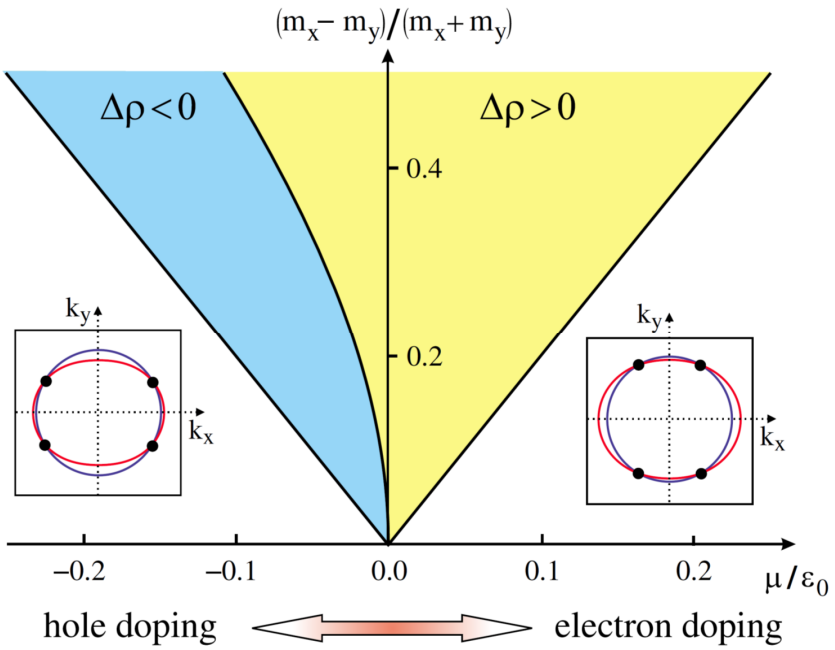

Figure 4.33: Sign of the low-temperature resistivity anisotropy $\Delta\rho$ as a function of the ellipticity $(m_x - m_y)/(m_x + m_y)$ of the electron pockets and the chemical potential μ. The inset shows that the nesting point of the Fermi surfaces is different between the electron and the hole-doped side. The figure is cited from Ref. [106].

asymmetry of the anisotropy depending on the topology of the Fermi surface in the nematic phase as shown in Fig. 4.33. In these theoretical studies, the contribution of the spin-fluctuation scattering to the in-plane resistivity is considered. The anisotropy of the spin-fluctuation scattering depends on the location of the hot spot in the Brillouin zone where the electron Fermi surface overlaps with the hole one. The position of the hot spot can be tuned by the carrier doping which change the shape of the electron and hole Fermi surfaces, resulting the electron-hole asymmetry of the spin-fluctuation scattering. Because the present results can be explained by this mechanism, the spin-fluctuation scattering mechanism would be a strong candidate for the theory in the nematic phase. Recently, Kuo *et al.* [46] reported that the anisotropy in the nematic phase of the electron-doped Ba122 is independent of disorder. They compared the strain-induced resistivity anisotropy in the nematic phase of Co/Ni-Ba122 with the same T_{AFO} but the different residual resistivity. Their result demonstrates that the in-plane resistivity anisotropy in the nematic phase is not due to elastic scattering from anisotropic defects, which is consistent with my conclusion.

4.6 Summary

I found that the in-plane resistivity anisotropy, $\Delta\rho$, in the AFO phase is small, but it clearly shows a sign change with increasing substituent and decreasing temperature in hole-doped Cr-Ba122. This is similar to the case of hole-doped K-Ba122 but different from the cases of the electron-doped Co-Ba122 and Mn-Ba122 where holes are almost undoped. Moreover, the anisotropy above T_{AFO} shows electron-hole asymmetry in Co- and Cr-Ba122. These results demonstrate that the doping-dependent anisotropy of the Fermi surface indeed plays a dominant role in the resistivity anisotropy in both the AFO and the nematic phases, irrespective of the chemical substitution sites. My results suggest that all the proposed mechanisms that attribute the electron-hole asymmetry of $\Delta\rho$ to the difference in the impurity scattering strength alone are inadequate. Rather, it depends on the electron-hole asymmetry of Fermi surface topology whether the impurity scattering results in a positive or negative $\Delta\rho$.

Part V

Optical property of $Ba(Fe_{1-x}TM_x)_2As_2$ (TM=Cr, Mn, and Co)

5.1 Introduction

In iron-based superconductor (FeSC), superconductivity appears when the antiferromagnetic-orthorhombic (AFO) phase of parent compound, such as $BaFe_2As_2$ (Ba122), is suppressed [6, 7]. This suggests that superconductivity in FeSC is intimately related to a magnetic fluctuation. The AFO order is suppressed by a chemical substitution and applying pressure [6]. However, $Ba(Fe_{1-x}TM_x)_2As_2$ (TM=Cr, Mn; TM-Ba122) is the exceptional case that superconductivity is not induced by the chemical substitution. In Mn and Cr-Ba122 which are nominally hole-doped systems, the magnetic transition temperature $T_{\rm AFO}$ is suppressed by Mn and Cr-doping but new magnetic order appears above a critical concentration instead of superconducting phase [25, 24]. This is in contrast to its counterpart of the electron-doped Co-Ba122, where $T_{\rm AFO}$ is suppressed and superconducting phase appears with Co-doping. For elucidation of superconductivity mechanism in FeSC, it is important to understand what causes the different behaviors of these transition metal substitution systems. In addition, as discussed in the previous part, TM-Ba122 shows a different transport property, such as a different in-plane resistivity anisotropy. It is required to investigate how the different transition metal doping affects the electronic structure of TM-Ba122, for understanding the charge transport mechanism of iron-pnictides.

An optical measurement is a useful bulk-sensitive and energy-resolved probe for investigating the doping evolution of the electronic structure and charge carrier dynamics [59, 118, 58]. The previous optical studies of a parent and Co-Ba122 revealed that a metallic response is derived from multi-carriers in a low-energy region above $T_{\rm AFO}$, and the antiferromagnetic gap opens in a partial region of Fermi surfaces below $T_{\rm AFO}$ which is closed with Co-doping [119, 60, 61]. The important ingredient for superconductivity in FeSC will be revealed by comparing the low-energy charge dynamics of Co and Cr/Mn-Ba122.

In this study, I performed the optical study of $Ba(Fe_{1-x}TM_x)_2As_2$ (TM=Cr, Mn, and Co) with single crystals. I compared the doping evolution of optical conductivity $\sigma(\omega)$ in TM-Ba122 to reveal why superconductivity is not induced by Cr and Mn-doping but is induced by Co-doping. I demonstrated that the coherent carrier transport is strongly suppressed by magnetic impurity, such as Cr and Mn, while it is robust against nonmagnetic impurity, such as Co. In addition, I found a new anomalous feature above $T_{\rm AFO}$ in Cr and Mn-Ba122, which is not observed in Co-Ba122. I attribute this anomalous

feature to the collective effect between magnetic impurities and conduction electrons.

5.2 Doping dependence of optical spectra

In this study, I performed measurements of the frequency dependence of optical reflectivity R(ω), and obtained the optical conductivity $\sigma(\omega)$ by using Kramers-Kronig transformation. Figures 5.34(a)-(c), 5.35(a)-(d), and 5.36(a)-(c) show the temperature dependence of R(ω) of $Ba(Fe_{1-x}TM_x)_2As_2$ (TM=Cr, Mn, and Co). Here, I use the published data of R(ω) for a parent compound and Co-Ba122 [60]. In Fig. 5.37, I show R(ω) for $Ba(Fe_{0.98}Cr_{0.02})_2As_2$ ($T_{\rm AFO} = 122\,{\rm K}$) at 150 K (above $T_{\rm AFO}$) and 5 K (below $T_{\rm AFO}$). These spectra are typical for $Ba(Fe_{1-x}TM_x)_2As_2$ (TM=Cr, Mn, and Co) as shown in Figs. 5.34(a)-(c), 5.35(a)-(d), and 5.36(a)-(c) Above $T_{\rm AFO}$, R(ω) shows a metallic behavior, approaching to unity at $\omega = 0$. Below $T_{\rm AFO}$, the suppression of R(ω) appears below $1000\,{\rm cm}^{-1}$, which indicates the formation of energy gap due to the reconstruction of the Fermi surface by the magnetostructural transition. Low-ω R(ω) approaches unity even more steeply than that of R(ω) above $T_{\rm AFO}$. This suggests that the energy gap opens at a part of the Fermi surface and the system remains metallic below $T_{\rm AFO}$.

Figures 5.38(a)-(c), 5.39(a)-(d), and 5.40(a)-(c) show $\sigma(\omega)$ of $Ba(Fe_{1-x}TM_x)_2As_2$ (TM=Cr, Mn, and Co) at various temperatures. For the parent compound ($x = 0$), the spectrum above magnetic transition temperature shows a peak at $\omega = 0$ and a long tail extends to $2000\,{\rm cm}^{-1}$ or higher [Fig. 5.38(a)]. Below $T_{\rm AFO}$, $\sigma(\omega)$ below $650\,{\rm cm}^{-1}$ is suppressed and the suppressed spectral weight is transfered to higher energy region, forming a peak structure around $1000\,{\rm cm}^{-1}$. In the Co-doped systems, the low-energy peak at $\omega = 0$ remains above $T_{\rm AFO}$. Below $T_{\rm AFO}$, the suppression of the conductivity below $650\,{\rm cm}^{-1}$ gets small and the peak structure around $1000\,{\rm cm}^{-1}$ diminishes with doping [See Figs. 5.38(b) and (c)].

In Cr and Mn-doped systems, $\sigma(\omega)$ shows the peak structure around $500 \sim 1000\,{\rm cm}^{-1}$ below $T_{\rm AFO}$ as in Co-Ba122 (Figs. 5.39 and 5.40). This indicates that the SDW gap opens in Cr and Mn-Ba122 as in Co-Ba122. On the other hand, the Drude-like peak at $\omega = 0$ is strongly suppressed above and below $T_{\rm AFO}$, which is different from the case of Co-Ba122. As shown in Figs. 5.39(a) and 5.40(a), a Drude-like peak can be observed but becomes more broadened than that of Co-Ba122. With further doping, no Drude-

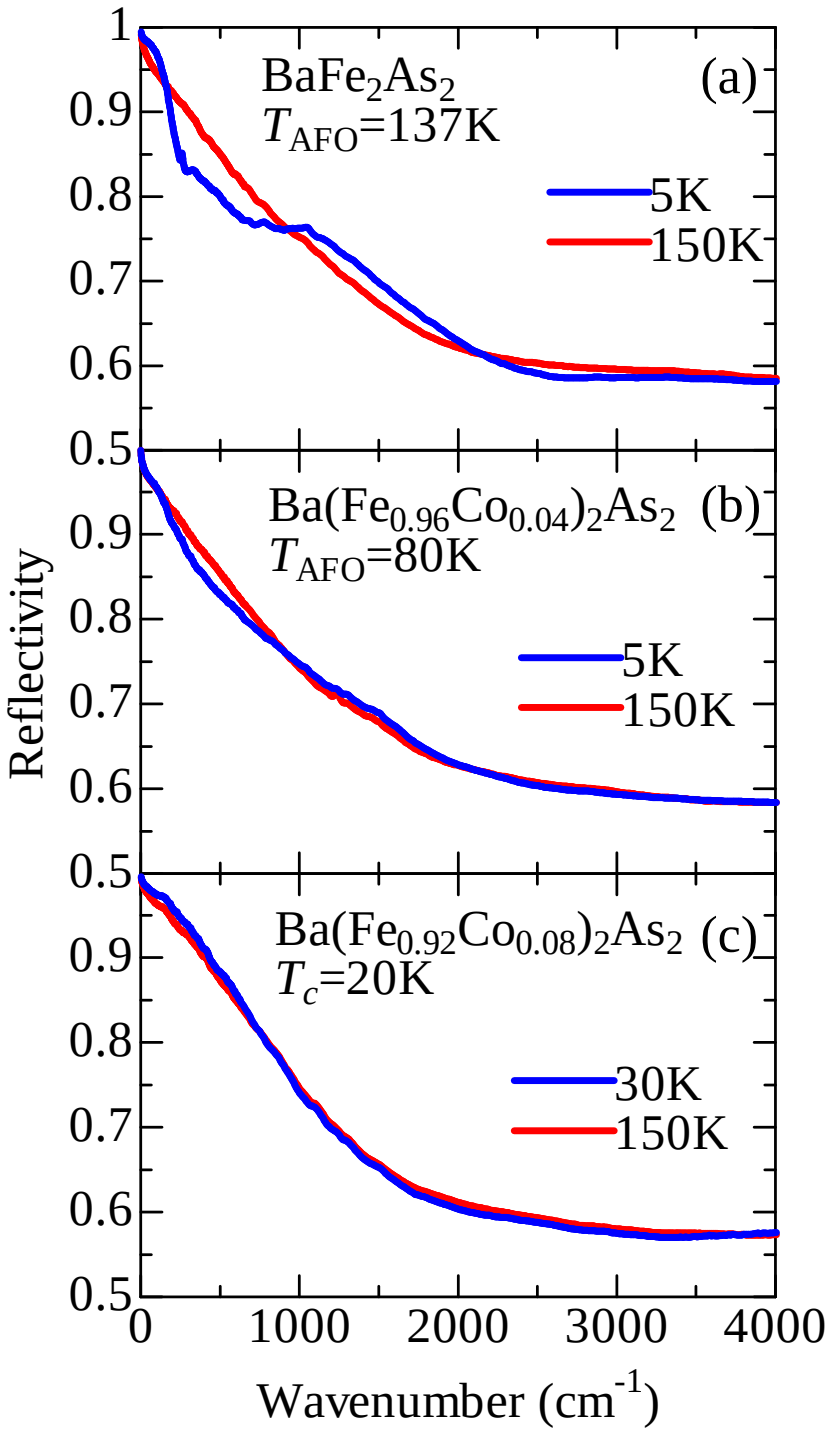

Figure 5.34: (a)-(c) Optical reflectivity of $Ba(Fe_{1-x}Co_x)_2As_2$ ($x = 0, 0.04,$ and 0.08) at 150 K (red) and 5 K (blue).

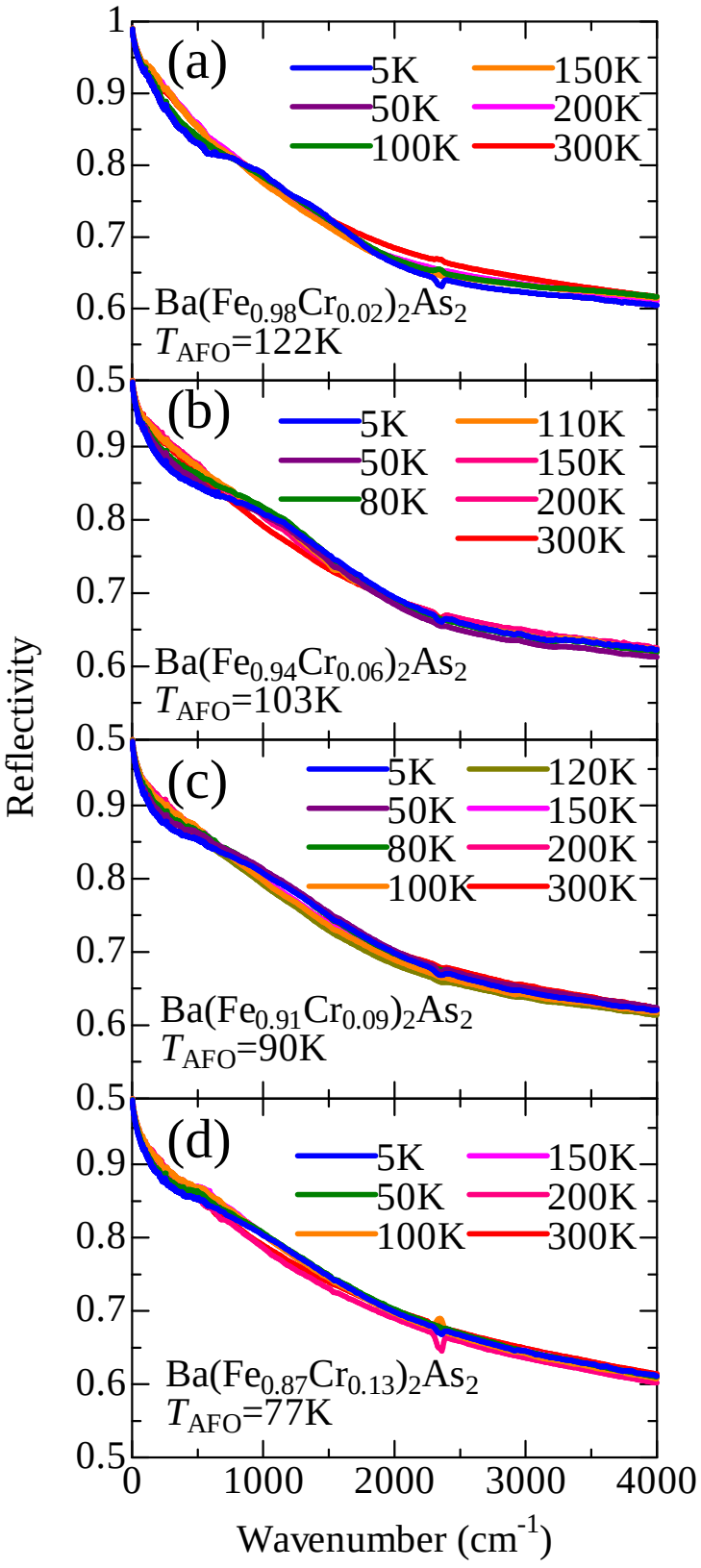

Figure 5.35: (a)-(d) Optical reflectivity of $Ba(Fe_{1-x}Cr_x)_2As_2$ ($x = 0.02, 0.06, 0.09,$ and 0.13) at various temperatures.

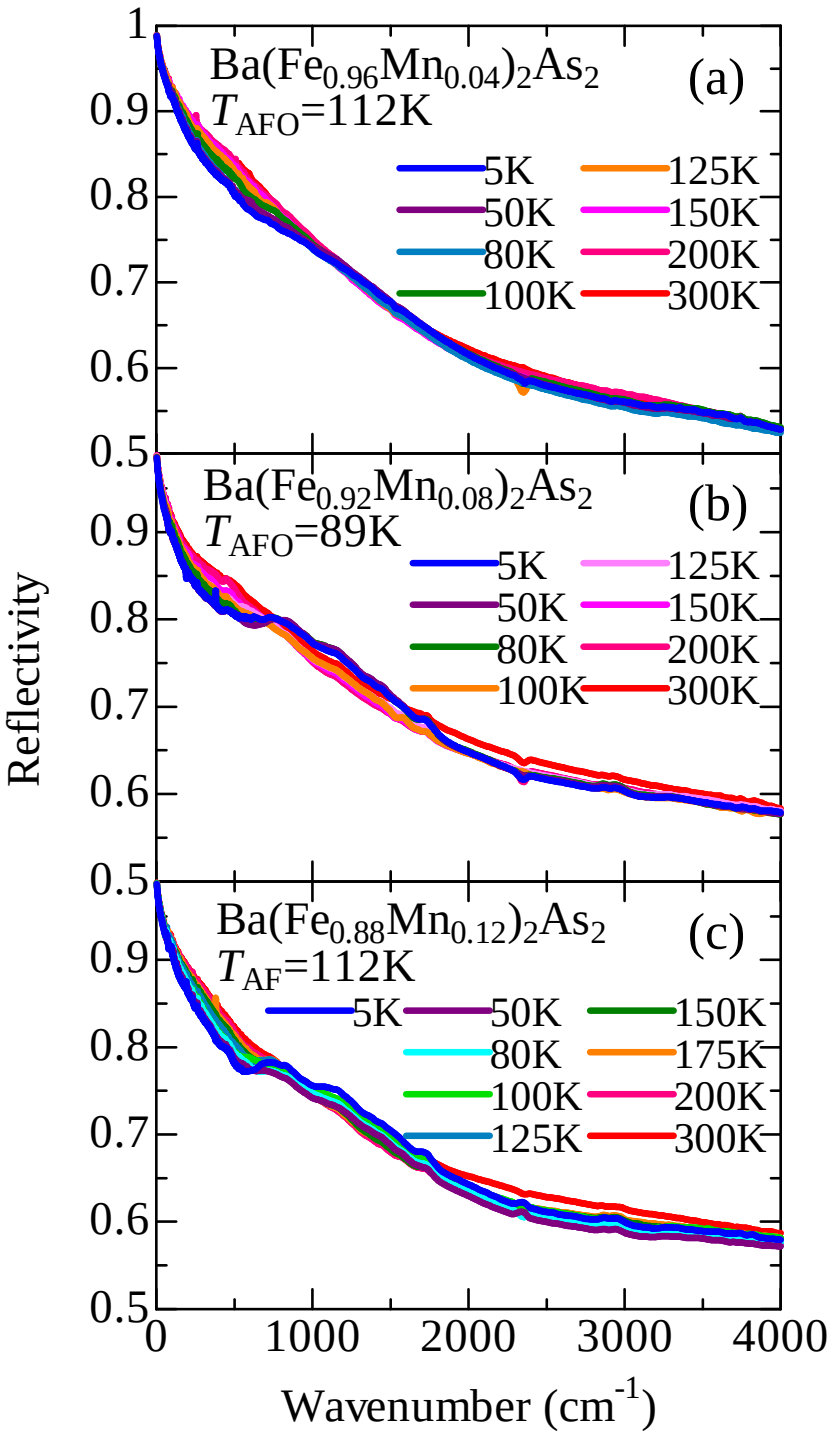

Figure 5.36: (a)-(c) Optical reflectivity of $Ba(Fe_{1-x}Mn_x)_2As_2$ ($x = 0.04, 0.08,$ and 0.12) at various temperatures.

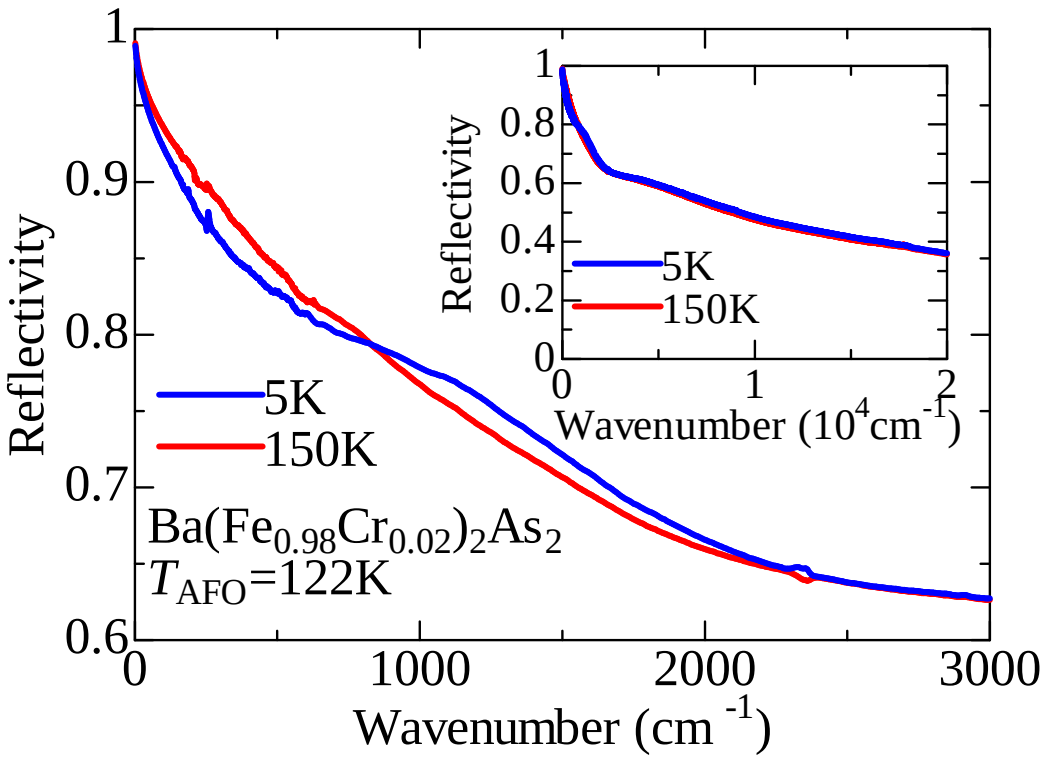

Figure 5.37: Optical reflectivity of $Ba(Fe_{0.98}Cr_{0.02})_2As_2$ at 150 K (red) and 5 K (blue). The inset shows the reflectivity up to 20000 cm^{-1}.

like peak is recognized, in contrast to Co-Ba122 where a sharp peak clearly exists at $\omega = 0$ even with $x = 0.08$ [Figs. 5.39(b)-(d) and 5.40(b)-(c)]. In addition, in Cr and Mn-doped systems above $T_{\rm AFO}$, a new peak structure is observed around $200\,{\rm cm}^{-1}$ which is absent in Co-doped systems. For the clarity, I show the enlarged views of the low-energy $\sigma(\omega)$ for Cr and Mn-Ba122 as shown in Figs. 5.41(a)-(d) and 5.42(a)-c). This indicates that the new mechanism, which induces the localized carrier state above $T_{\rm AFO}$, exists in Cr and Mn-Ba122.

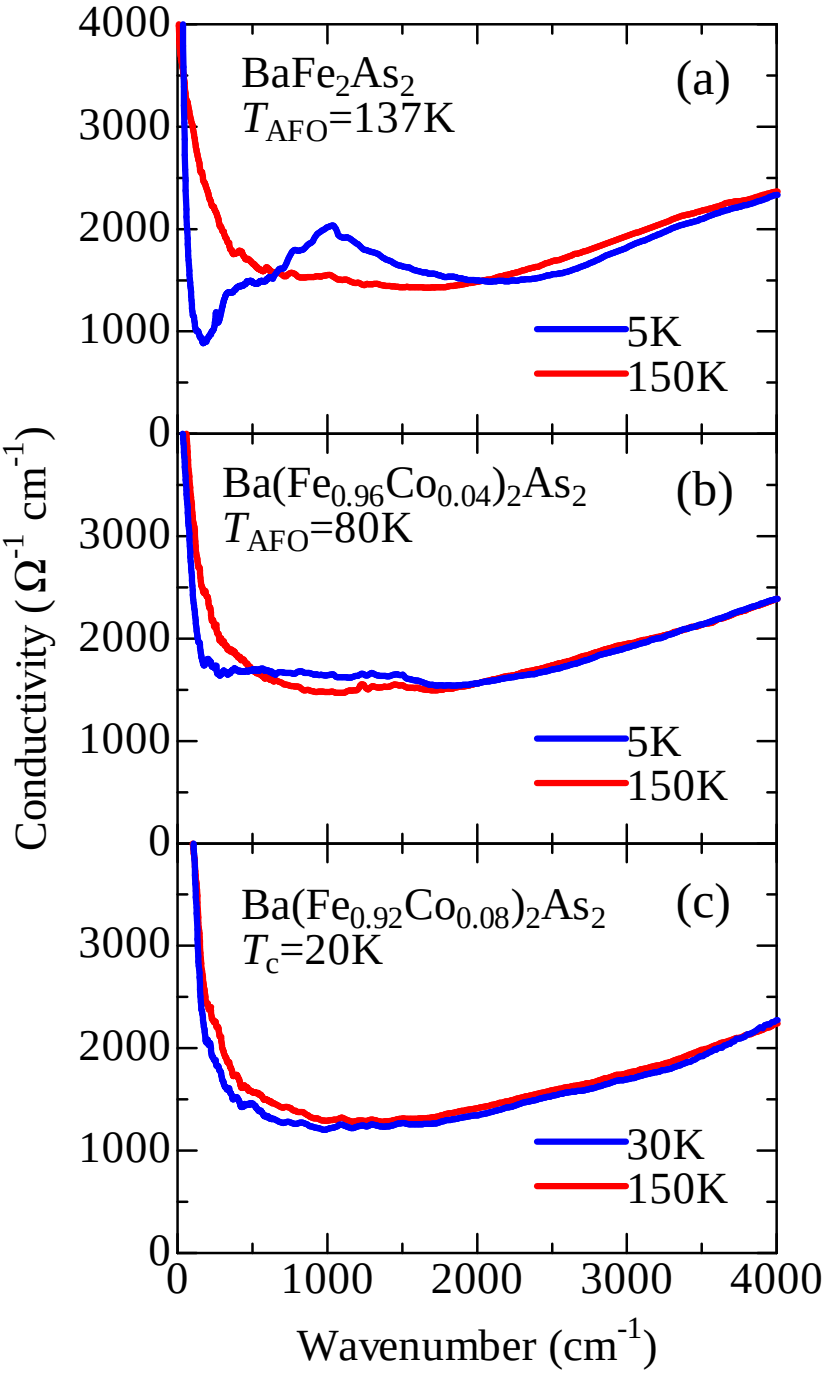

Figure 5.38: (a)-(c) Optical conductivity of $Ba(Fe_{1-x}Co_x)_2As_2$ ($x = 0, 0.04,$ and 0.08) at 150 K (red) and 5 K (blue).

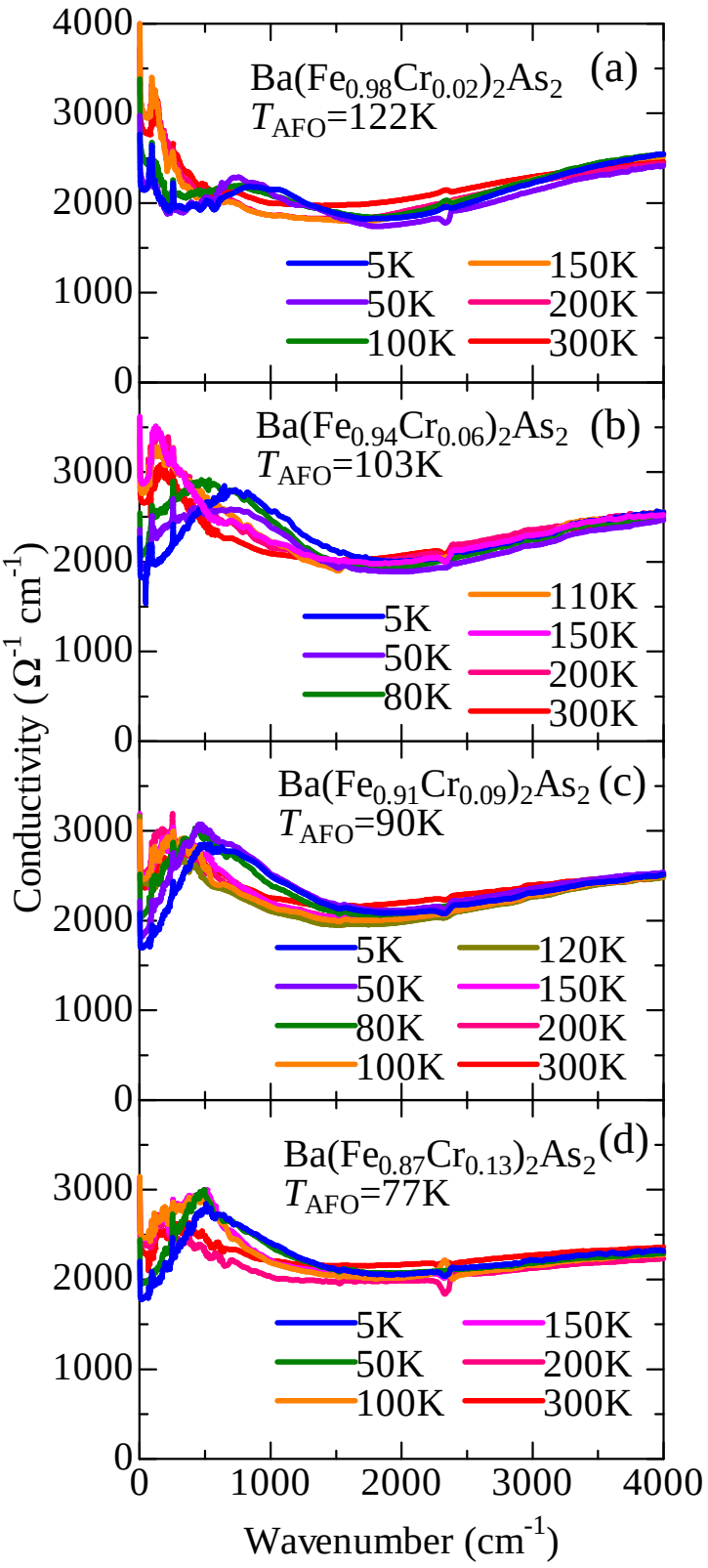

Figure 5.39: (a)-(d) Optical conductivity of $Ba(Fe_{1-x}Cr_x)_2As_2$ (x = 0.02, 0.06, 0.09, and 0.13) at various temperatures.

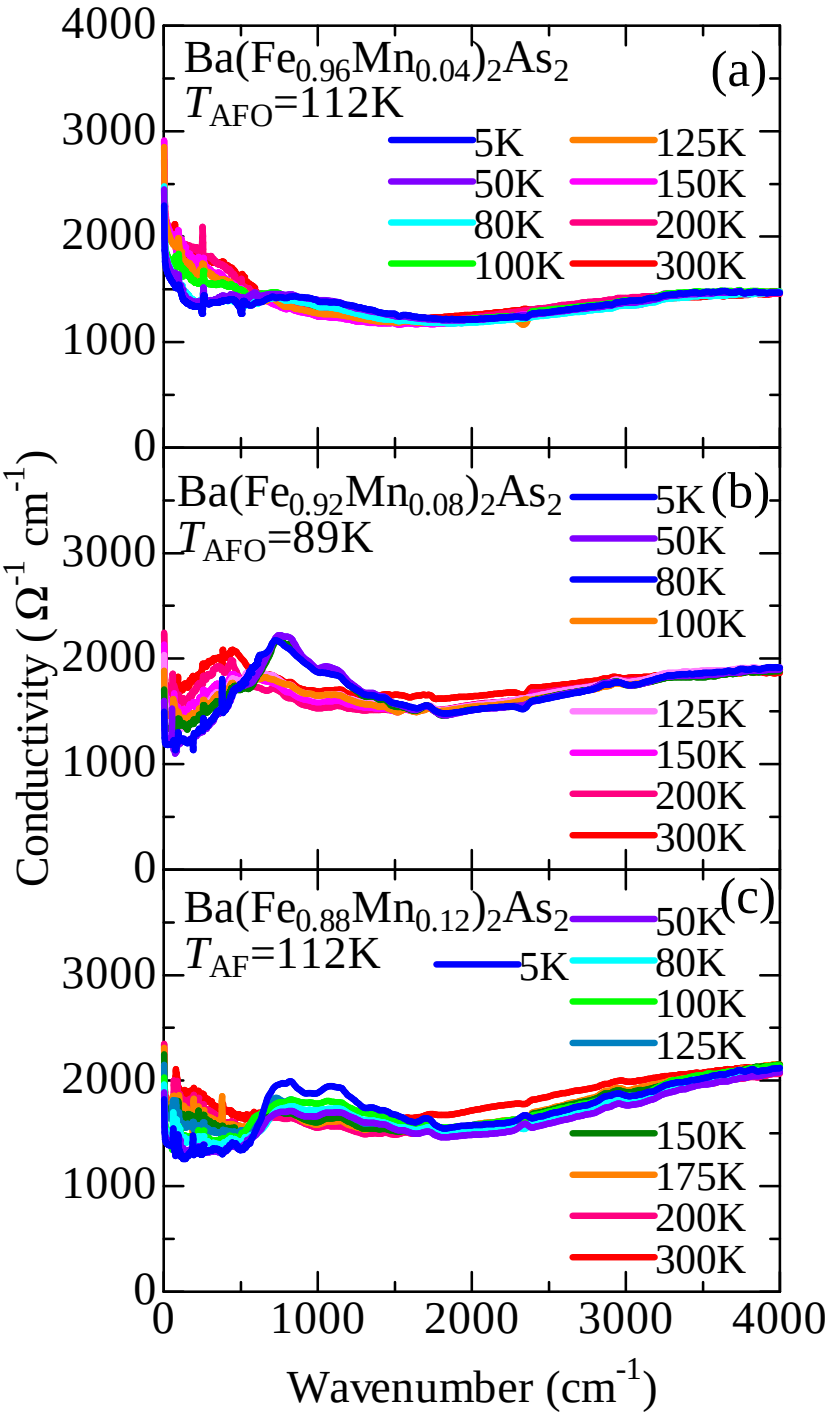

Figure 5.40: (a)-(c) Optical conductivity of $Ba(Fe_{1-x}Mn_x)_2As_2$ ($x = 0.04, 0.08,$ and 0.12) at various temperatures.

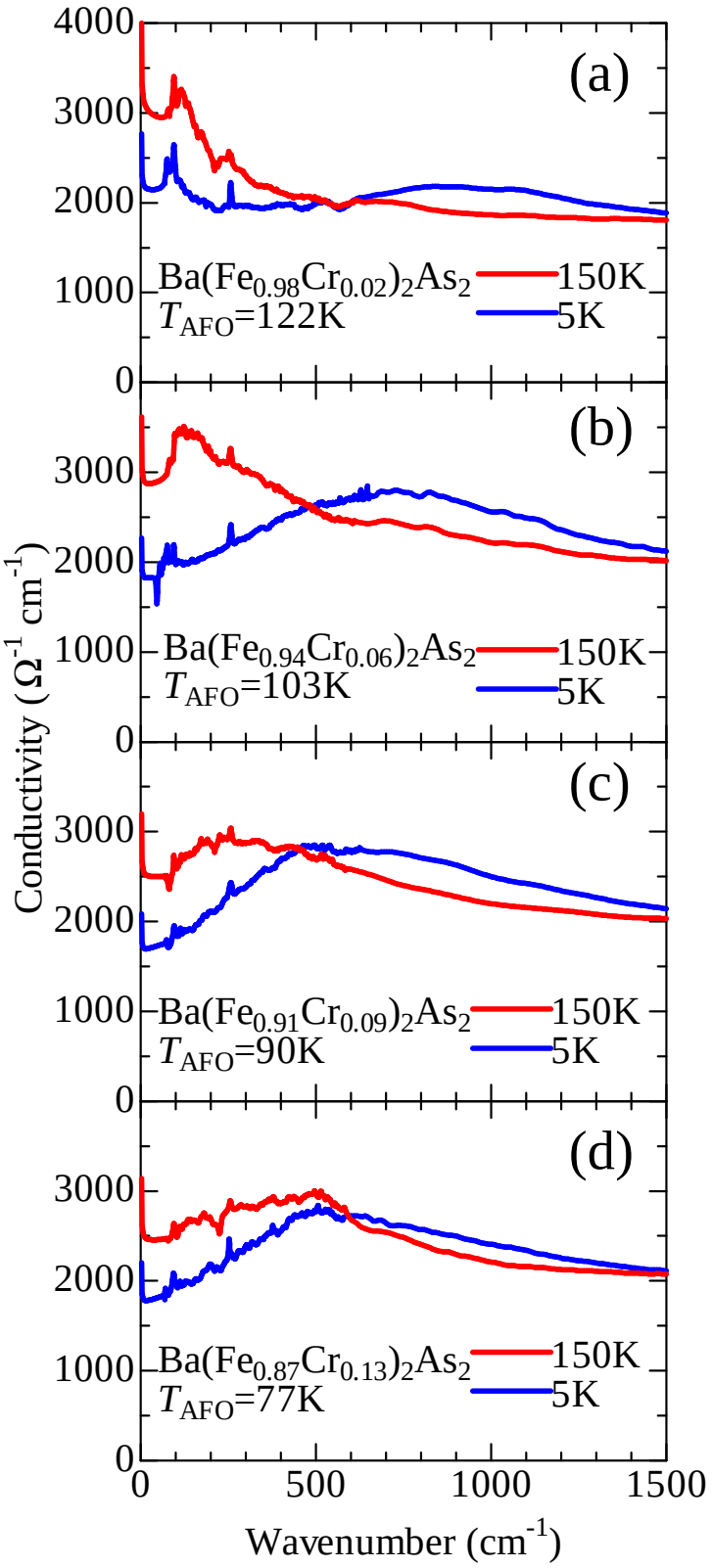

Figure 5.41: (a)-(d) Optical conductivity of $Ba(Fe_{1-x}Cr_x)_2As_2$ (x = 0.02, 0.06, 0.09, and 0.13) at 150 K and 5 K below 1500 cm^{-1}.

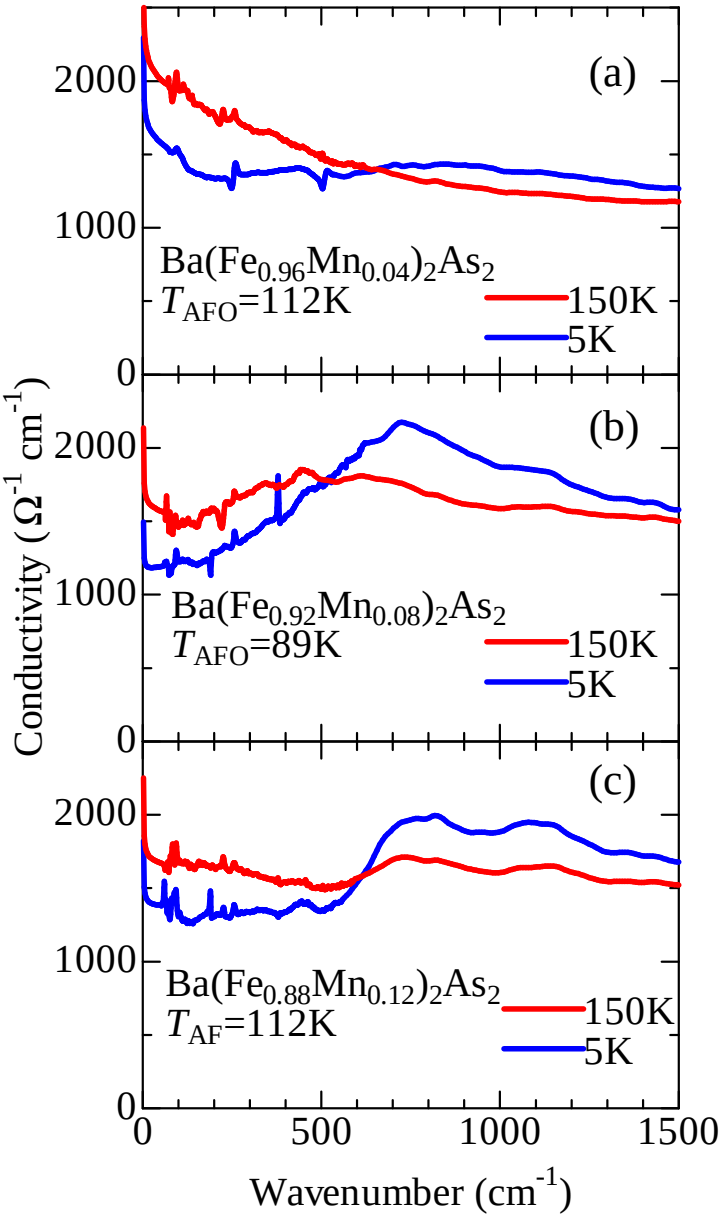

Figure 5.42: (a)-(c) Optical conductivity of $Ba(Fe_{1-x}Mn_x)_2As_2$ ($x = 0.04, 0.08,$ and 0.12) at 150 K and 5 K below 1500 cm^{-1}.

5.3 Fitting of $\sigma(\omega)$ with Drude-Lorentz model

To get more information from the optical spectra of TM-Ba122, I fit the spectra based on Drude-Lorentz model. When I fit a spectrum, I basically assumed two Drude components because the iron pnictides are multi-band systems. This assumption is adopted in the previous studies [60, 61]. This two Drude model works well in the parent compound and Co-Ba122 but not in Cr and Mn-Ba122 because the sharp Drude feature in the low-energy region becomes unclear with Cr and Mn-doping as discussed later. Therefore, I fit the optical spectrum at $T = 150\,\mathrm{K}$ of Cr and Mn-Ba122 with two different methods. In one method, I fit the data of Cr and Mn-Ba122 with one Drude components as far as possible, as shown in Figs. 5.44 and 5.45. In this method, I cannot help using the two Drude component for $x = 0.02$ of Cr-Ba122, and $x = 0.04$ of Mn-Ba122 because there exists small but relatively sharp Drude component. However, other data can be fitted with one Drude component. In another method, I fit the data of Cr and Mn-Ba122 with fixing the incoherent component and changing the coherent component, as shown in Figs. 5.46 and 5.47.

The fitting results by the first method are shown in Figs. 5.44(a)-(e) and 5.45(a)-(d) for the 150 K spectra of all the measured samles, while the results by the second method are shown in Figs. 5.46(a)-(e), and 5.47(a)-(d).

In the parent compound above T_{AFO}, the low-energy $\sigma(\omega)$ is dominated by two Drude components as shown in Fig. 5.43(a). One component is a coherent Drude term which has a relatively sharp peak at $\omega = 0$, and the other is an incoherent term which has a broad peak at $\omega = 0$ with a long higher-energy tail. The coherent and incoherent components have the scattering rate, $1/\tau \sim 200\,\mathrm{cm}^{-1}$ and $2000\,\mathrm{cm}^{-1}$, respectively. These values correspond to the mean free path l ($=v_{\mathrm{Fermi}}\tau$, v_{Fermi}:Fermi velocity) of $\sim 50\,\text{Å}$ and $\sim 1.7\,\text{Å}$ for the coherent and the incoherent components, respectively [120]. Considering that the shortest interatomic distance is about 2.4 Å, the former is much larger than interatomic distance and the latter is shorter than that. Therefore, I call the latter "incoherent". In order to fit $\sigma(\omega)$ in the higher energy region, I used the third term to reproduce a peak structure around $5000\,\mathrm{cm}^{-1}$ which originates from the excitation from hybridized Fe-d and As-p states below the Fermi energy to Fe-d states in the vicinity of the Fermi level [121]. In Co-doped systems above T_{AFO} as shown in Figs. 5.43(b) and 5.43(c), the coherent term increases with doping, while the incoherent term is almost unchanged. According to the previous studies, the coherent term

derives mainly from electron carriers and the incoherent term is related to the hole like carriers [61] or would arise from some Fermi-surface sheets or their segments which fulfil the nesting condition for an SDW gap instability [60]. Thus this result suggests that Co-substitution acts as an electron doping.

In contrast to the parent compound and Co-doped systems, Cr and Mn-doped systems show different optical spectra. In Cr and Mn-doped systems, the low-energy $\sigma(\omega)$ is strongly suppressed as shown in Figs. 5.44(a)-(e) and 5.45(a)-(d) [or Figs. 5.46(a)-(e) and 5.47(a)-(d)]. This suppression is mainly attribute to the suppression of the coherent Drude term. In fact, the relatively sharp peak structure at $\omega = 0$ can be seen in $x = 0.02$ for Cr and $x = 0.04$ for Mn-doped Ba122, while the peak cannot be clearly observed in further doped systems. In such high-doped compounds, the incoherent component dominates $\sigma(\omega)$ at $\omega = 0$. This indicates that the dc-conductivity above T_{AFO} is mostly governed by the doping-independent incoherent component as Cr or Mn-concentration increases, which is consistent with the saturation of the in-plane resistivity with Cr and Mn-doping discussed later. The suppression of the coherent term can be attribute to the increase of the scattering rate or the reduction of plasma frequency based on the Drude formula. More details are discussed in the following section.

In addition to the suppression of the coherent component, a new anomaly is observed in Cr and Mn-doped systems. As shown in Figs. 5.44(a)-(e), 5.45(a)-(d) [or Figs. 5.46(a)-(e) and 5.47(a)-(d)], a peak like structure is observed around $200\,\mathrm{cm}^{-1}$ in Cr and Mn-doped systems, which is not observed in Co-doped systems. The origin of this new anomalous feature is discussed in the following section.

Next, I move to the optical spectrum in the AFO phase. In the parent compound as shown in Fig. 5.48(a), the low-energy spectrum can be decomposed into one narrow Drude component and two peak structures around $500 \sim 1000\,\mathrm{cm}^{-1}$. The lowest-energy part can be fitted using a narrowed Drude term with the same weight as that at $T = 150\,\mathrm{K}$. This means that an antiferromagnetic gap, or spin-density-wave (SDW) gap opens mainly on hole Fermi surfaces, and the incoherent Drude component, which is observed above T_{AFO}, is decomposed into two peak structures around $500 \sim 1000\,\mathrm{cm}^{-1}$, and thus it does not contribute to the dc conductivity in the antiferromagnetic phase. The presence of remaining Drude component indicates that SDW gap opens at only partly at the multi-bands Fermi surface.

With Co-doping, the gap like feature shifts to lower energy region and disappears as the AFO phase is suppressed, while the narrow peak at $\omega = 0$

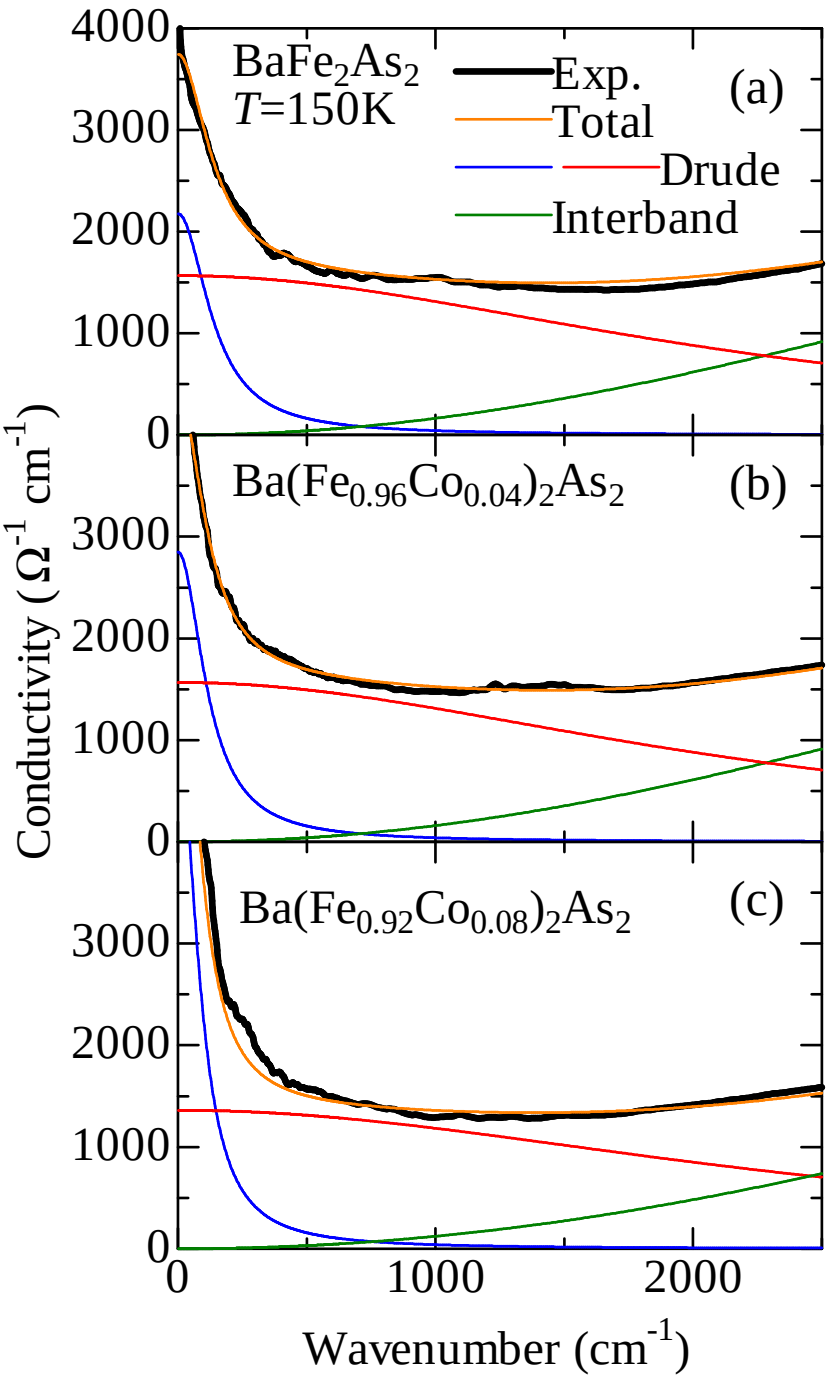

Figure 5.43: The fitting results of $Ba(Fe_{1-x}Co_x)_2As_2$ at 150 K.

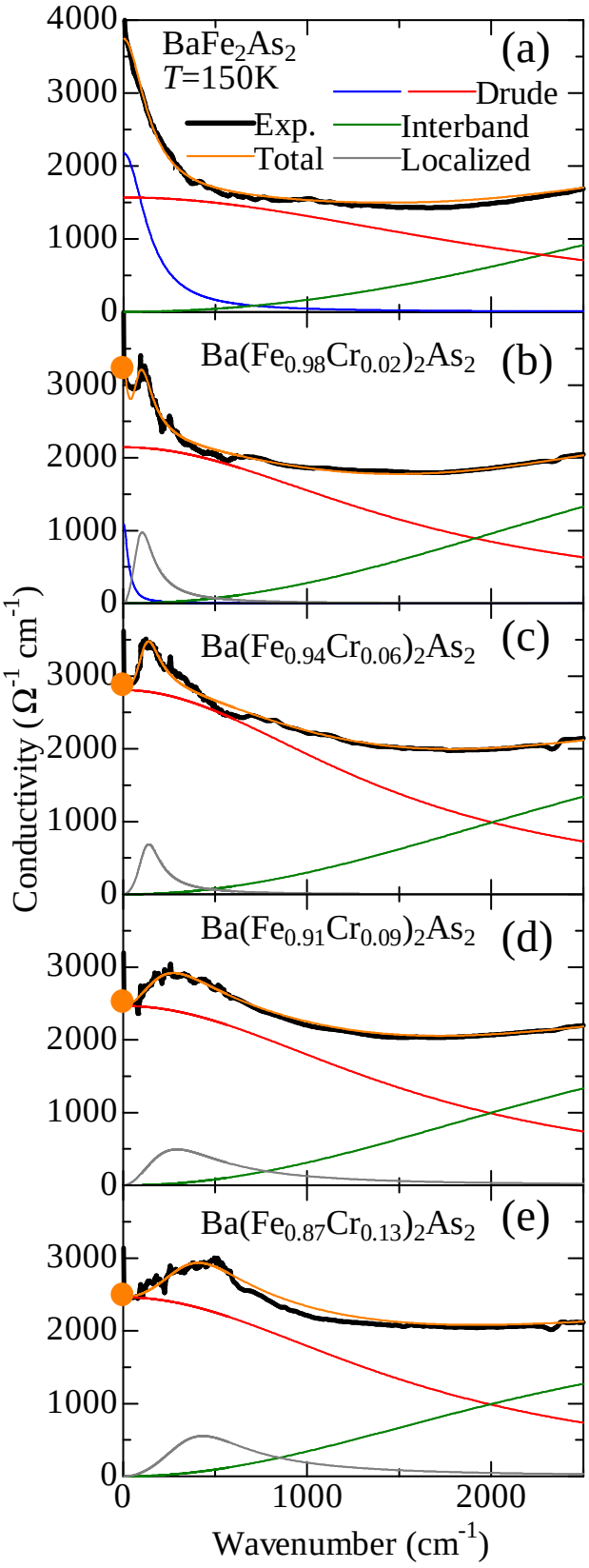

Figure 5.44: The fitting results of $Ba(Fe_{1-x}Cr_x)_2As_2$ at 150 K. Solid circles indicate the values of the dc ($\omega = 0$) conductivity for each composition. These are the fitting results of "one Drude" fitting method.

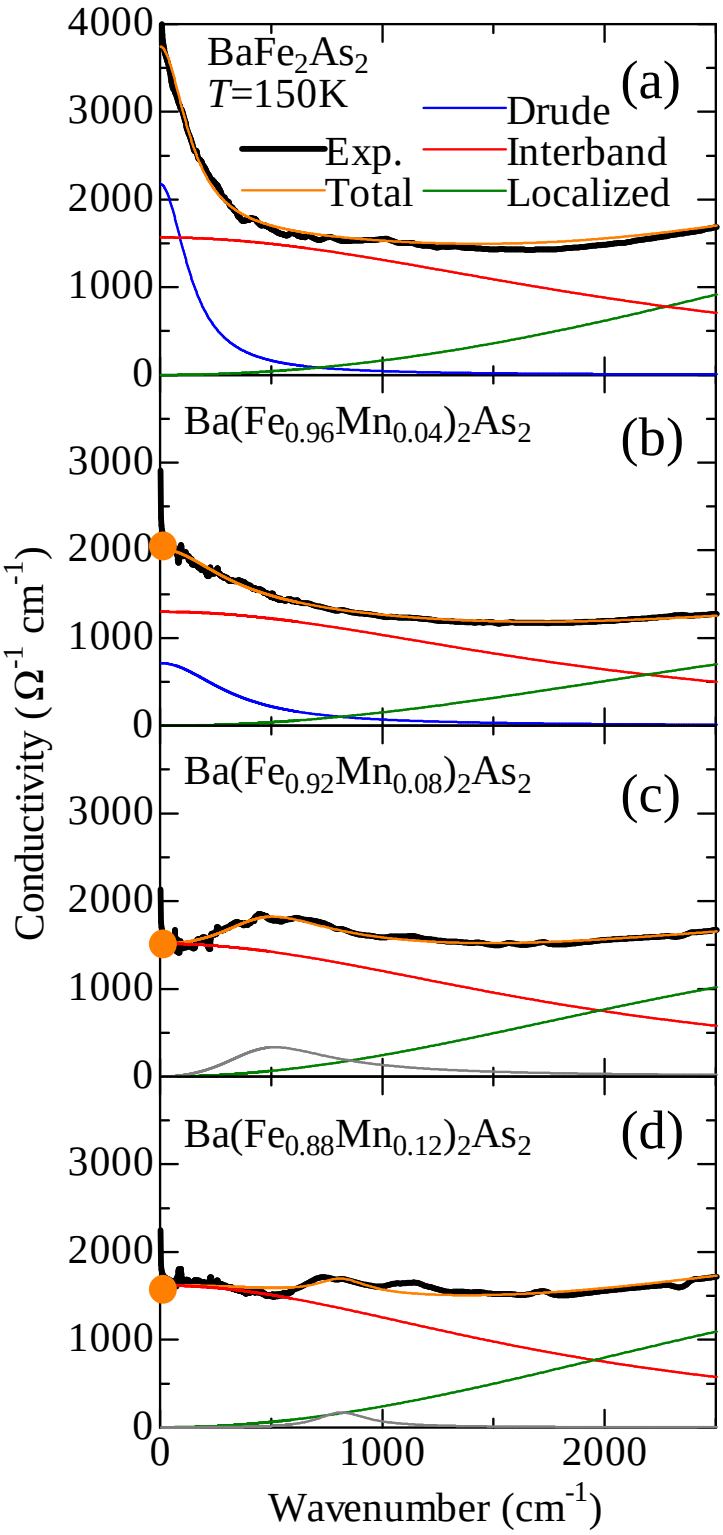

Figure 5.45: The fitting results of $Ba(Fe_{1-x}Mn_x)_2As_2$ at 150 K. Solid circles indicate the values of the dc ($\omega = 0$) conductivity for each composition. These are the fitting results of "one Drude" fitting method.

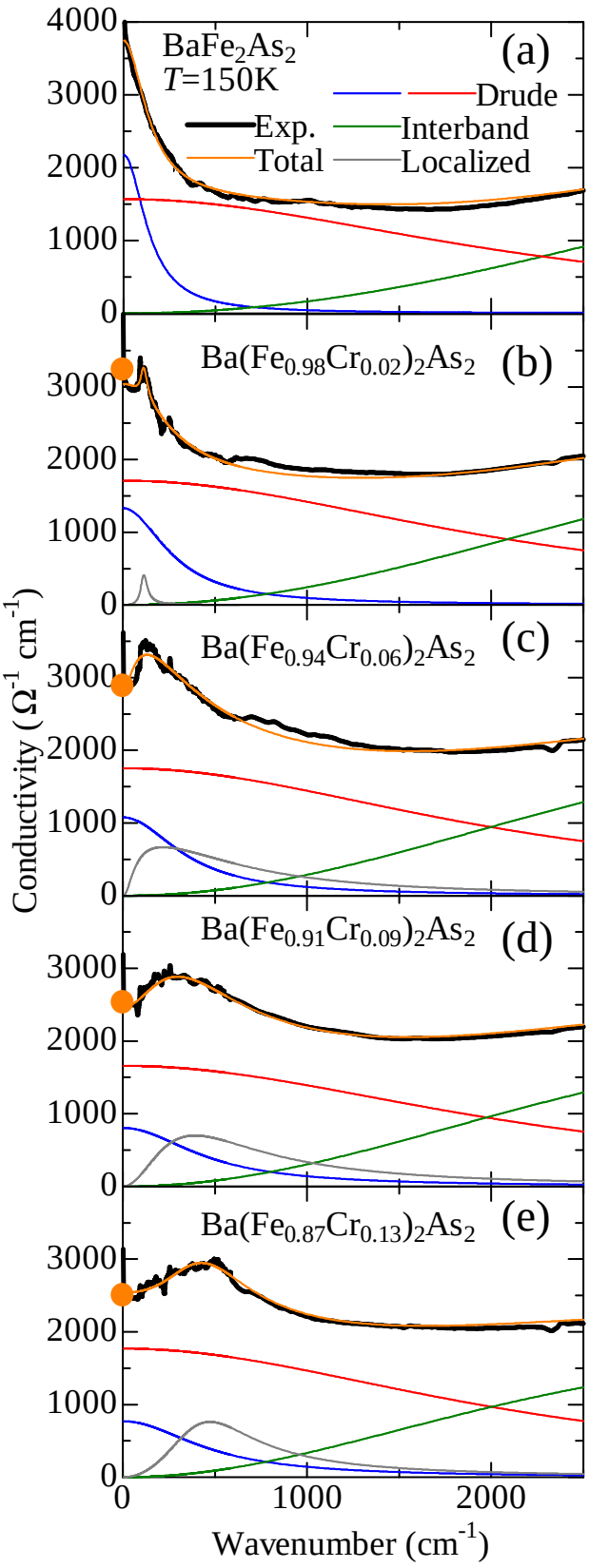

Figure 5.46: The fitting results of $Ba(Fe_{1-x}Cr_x)_2As_2$ at 150 K. Solid circles indicate the values of the dc ($\omega = 0$) conductivity for each composition. For the incoherent component of Cr-doped systems, the similar fitting parameters to that of the parent compound are used.

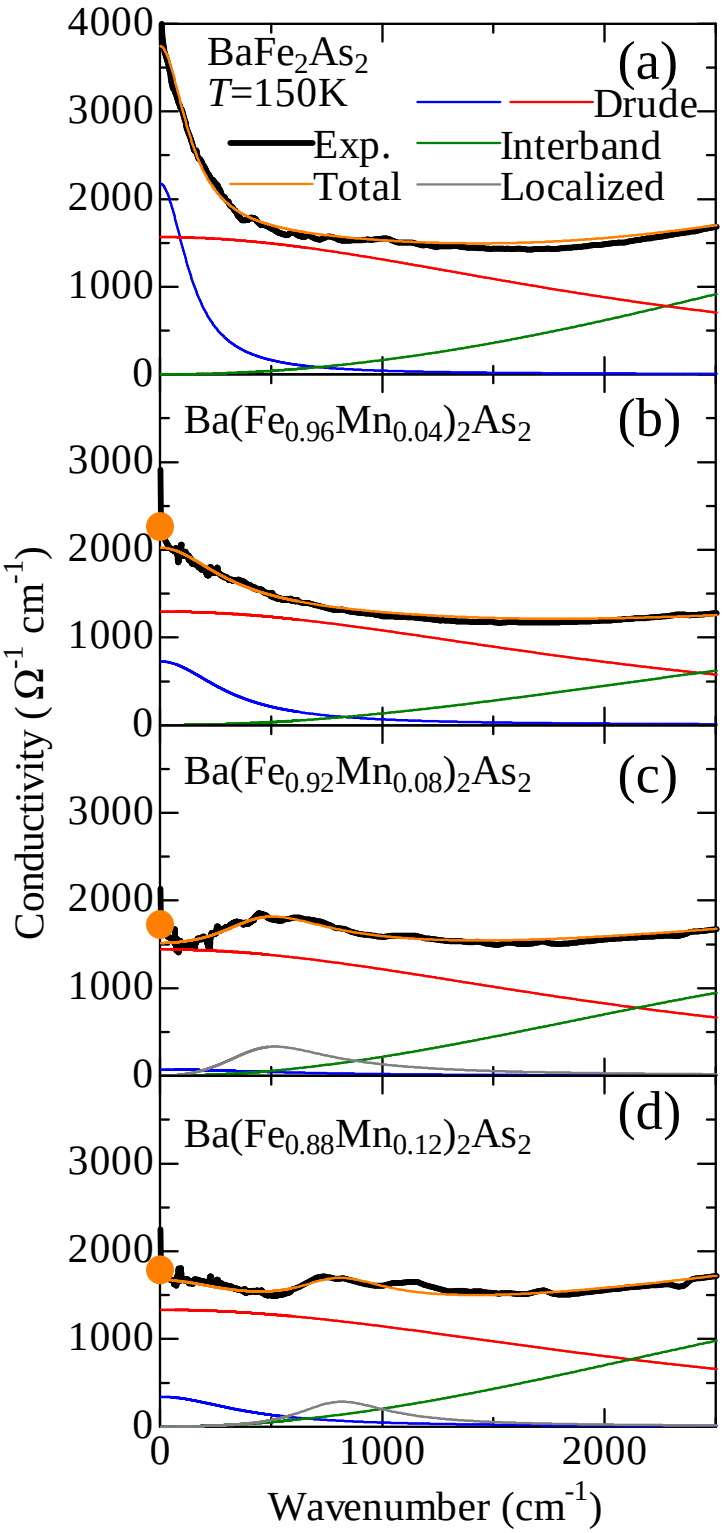

Figure 5.47: The fitting results of $Ba(Fe_{1-x}Mn_x)_2As_2$ at 150 K. Solid circles indicate the values of the dc ($\omega = 0$) conductivity for each composition. For the incoherent component of Mn-doped systems, the similar fitting parameters to that of the parent compound are used.

is very pronounced even in the AFO phase, as shown in Fig. 5.48(b). At $x = 0.08$ in Fig. 5.48(c), the peak feature is not observed down to 30 K. This indicates that the AFO transition is completely suppressed at this composition. It is noted that the superconducting transition is observed at $T_c \sim 20$ K in this composition and the spectral behavior of $\sigma(\omega)$ below T_c suggests Co-Ba122 is a full gap superconductor [60].

In Cr and Mn-doped systems shown in Figs. 5.49(a)-(e) and 5.50(a)-(d), the low-energy $\sigma(\omega)$ is suppressed below $T_{\rm AFO}$ and a gap like feature is clearly formed in the higher energy region, as in the case of Co-Ba122. In these systems, the Drude peak at $\omega = 0$ exists but is much broader than that of Co-doped system. The SDW gap energy shifts to lower energy region with Cr and Mn-doping except for Mn-Ba122 with $x = 0.12$, which is consistent with the reduction of $T_{\rm AFO}$ with doping as in Co-Ba122. These results in the AFO phase of TM-Ba122 suggest that the main difference between Co and Cr/Mn-Ba122 is the strong suppression of the coherent Drude component.

In the following sections, I discuss the doping dependence of the SDW gap energy, the impurity scattering effect on coherent part, and the origin of the localized carrier feature above $T_{\rm AFO}$ observed in Cr and Mn-Ba122.

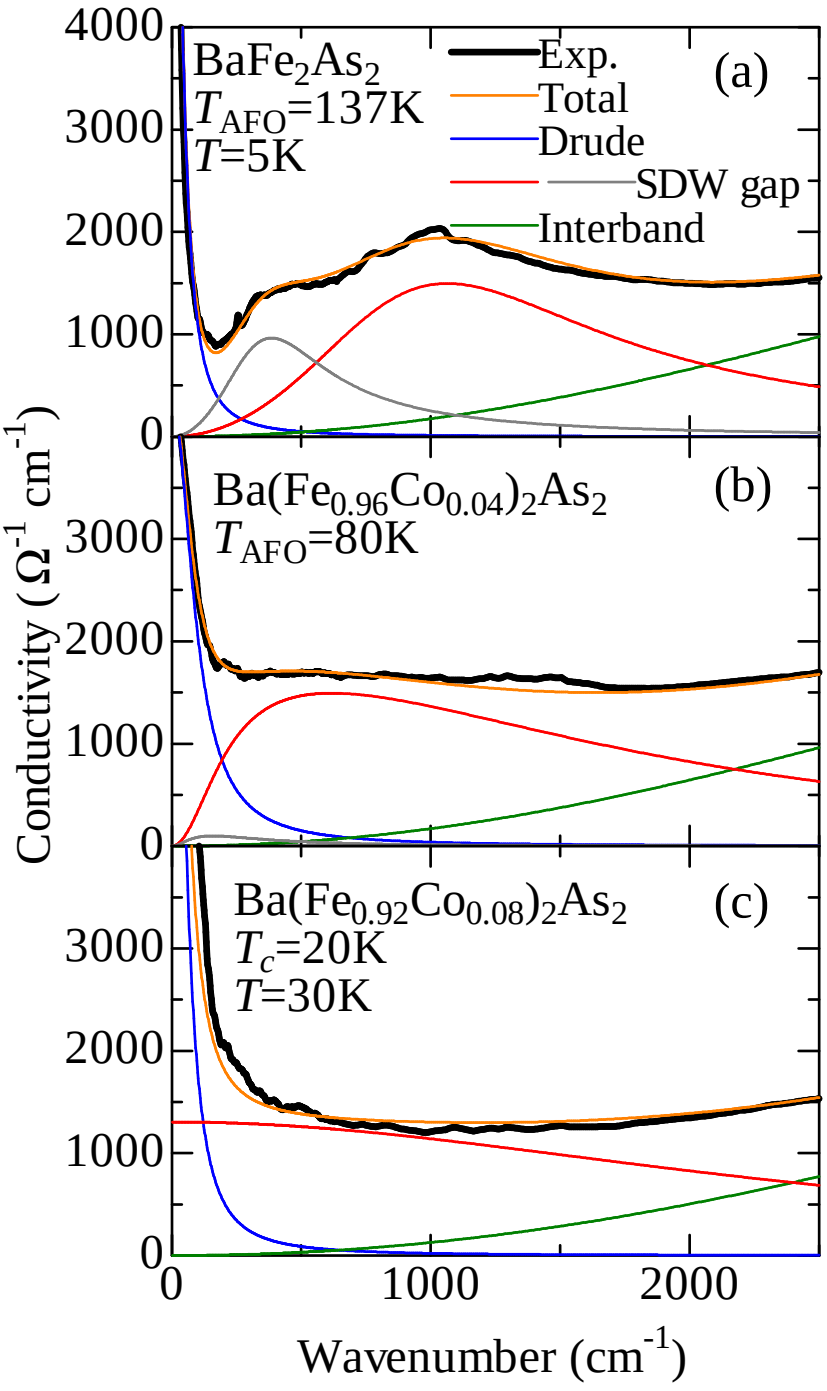

Figure 5.48: The fitting results of $Ba(Fe_{1-x}Co_x)_2As_2$ at 5 K.

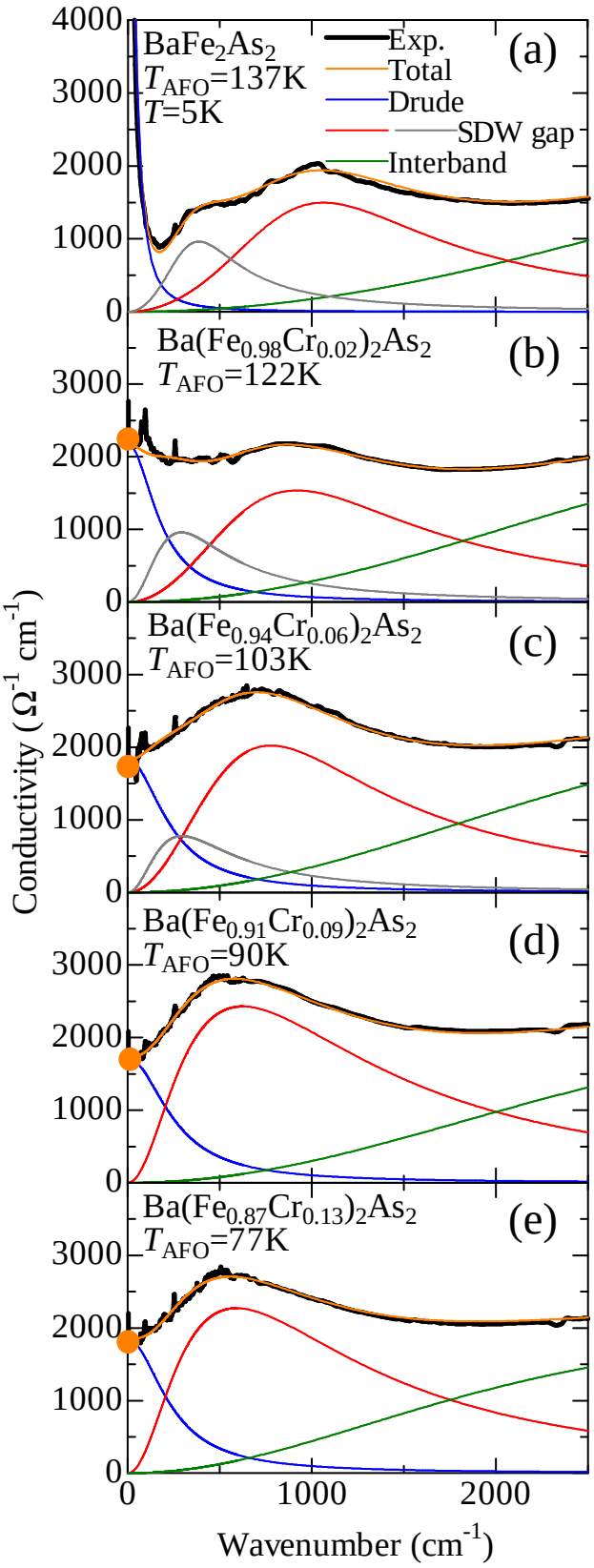

Figure 5.49: The fitting results of $Ba(Fe_{1-x}Cr_x)_2As_2$ ($x = 0.02, 0.06, 0.09,$ and 0.13) at 5 K. Solid circles indicate the values of the dc ($\omega = 0$) conductivity for each composition.

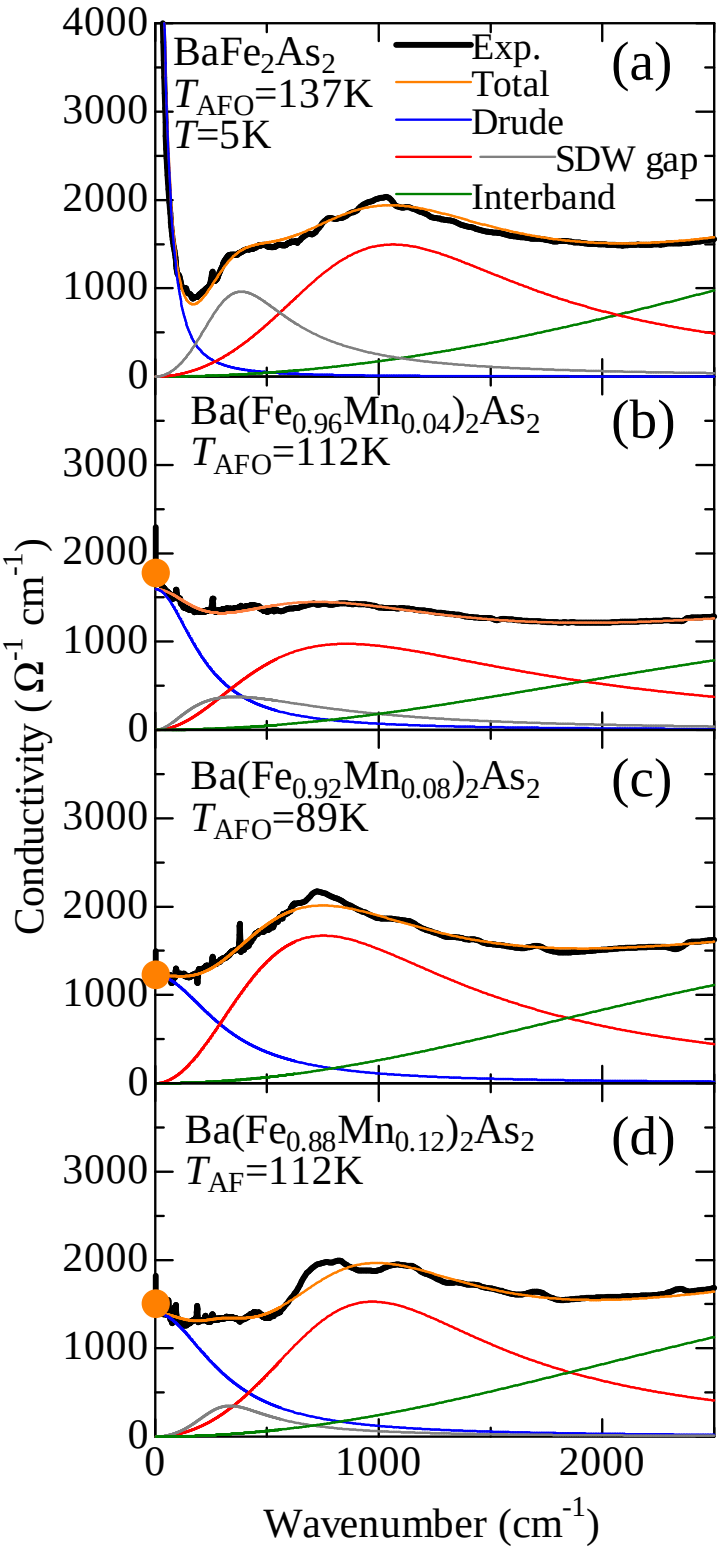

Figure 5.50: The fitting results of $Ba(Fe_{1-x}Mn_x)_2As_2$ at 5 K. Solid circles indicate the values of the dc ($\omega = 0$) conductivity for each composition.

5.4 Transition metal doping effect on the AFO state

First, I discuss the doping effect on the AFO state in TM-Ba122.

Figures 5.51(a) and 5.51(b) show the doping and the $T_{\rm AFO}$ dependence of the SDW gap energy of $Ba(Fe_{1-x}TM_x)_2As_2$ and $(Ba_{1-x}K_x)Fe_2As_2$ [122]. Here, I use the peak position to estimate the SDW gap energy. It is noted that I plot the larger SDW gap energy estimated from the fitting because the smaller one is difficult to reliably extract from the present analysis.

As shown in Fig. 5.51(a), in all the case, the doping results in the reduction of a SDW gap energy except for Mn-Ba122 with $x = 0.12$ although the suppression rate of the SDW gap energy depends on the doped atom. The suppression rates of Cr and Mn-Ba122 are between the largest rate of electron doped Co-Ba122 and the smallest one of hole doped of K-Ba122. Considering that hole carriers are doped in Cr-Ba122 and carriers are almost undoped in Mn-Ba122 as indicated in the previous part, the larger suppression rate in Co-Ba122 than in Cr and Mn-Ba122 can be attribute to electron doping effect, and the smallest suppression rate of K-Ba122 can be attribute to the doped site dependence or the hole doping level.

As shown in Fig. 5.51(b), I found that the AF gap energy 2Δ is linearly proportion to $T_{\rm AFO}$ in a wide doping range. The obtained relation is $2\Delta = 7.8k_{\rm B}T_{\rm AFO}$, which is much different from the relation observed in the conventional density wave materials, $2\Delta = 3.52k_{\rm B}T_{\rm SDW}$ [123, 124], indicating that the magnetic state of iron-pnictides is not a simple SDW state. Such a large value of 2Δ is also reported for $A122$ (A=Sr and Eu) and ReFeAsO (Re=La, Nd, and Sm) [119, 61, 125], indicating that this relation is universal for the magnetic state in iron-pnictides.

On the other hand, theoretical studies [126, 127] suggest that the SDW peak energy depends on the ordered magnetic moment of Fe in the AFO state. This magnetic moment dependence comes from that the coulomb interaction and the Hund's coupling strength determine how the reconstruction of the band structure due to the magnetic order is induced and they also control the size of the magnetic moment, These theoretical works can explain the difference of the SDW gap energy in different iron-pnictides with different magnetic moments [119, 125]. Figure 5.51(c) shows the doping dependence of the magnetic moment of Fe for $Ba(Fe_{1-x}TM_x)_2As_2$ and $(Ba_{1-x}K_x)Fe_2As_2$ [12, 24, 25, 128]. The magnetic moment is rapidly suppressed by Co-doping while

other doping results in much slower suppression of the magnetic moment. To confirm the theoretical prediction, I plot the relation between the SDW gap energy and the ordered moment as shown in Fig. 5.51(d). Unexpectedly, there is no clear relation between the SDW gap energy and the magnetic moment, in contrast to that between the SDW gap energy and $T_{\rm AFO}$ in Fig. 5.51(b). These results indicate that the magnetic moment is not a unique parameter which determine the SDW gap energy and $T_{\rm AFO}$. The present study indicates that the different SDW gap energy in different iron-pnictides comes from the difference of the carrier doping rather than the magnetic moment.

It was suggested in iron-pnictides that the stripe-type magnetic order results from the nesting between the hole and electron Fermi surfaces of itinerant electrons, in other words, the SDW order [129, 130]. Alternatively, it was also proposed that local superexchange interaction mediated through the off-plane As atom plays an important role [131, 132]. The conventional relation $2\Delta = 3.52 k_{\rm B} T_{\rm SDW}$ for the SDW materials is based on the Fermi surface nesting, or the itinerant picture. Considering the large Hund's coupling in iron-pnictides [133], the Hund's couping between the itinerant and the localized electrons can change the nature of the SDW state. More detailed studies of the effect of the carrier doping and the structural parameter on the AFO state are required based both on the itinerant picture and the local superexchange mechanism.

As mentioned above, the situation is different in Mn-Ba122 with $x = 0.12$. The magnetic transition temperature $T_{\rm AF}$ (112 K) of $x = 0.12$ estimated from the transport and magnetic susceptibility measurement is higher than that of $x = 0.08$ ($T_{\rm AFO} = 89$ K). This doping dependence of $T_{\rm AF}$ is consistent with the previous study [25]. In Mn-Ba122 with $x = 0.12$, the antiferromagnetic (AF) gap like feature is observed below $T_{\rm AF}$ and the peak energy is higher than that of Mn-Ba122 with $x = 0.08$ as shown in Fig. 5.51(a). According to the previous study, the ground state of Mn-Ba122 with $x = 0.12$ is the tetragonal-antiferromagnetic phase while most of the underdoped iron-based superconductor is orthorhombic-antiferromagnetic phase. The origin of this tetragonal-antiferromagnetic phase remains an open issue [134, 135, 136]. The present result of Mn-Ba122 with $x = 0.12$ revealed that the AF gap opens in such a novel magnetic state, and the gap energy is correlate with $T_{\rm AF}$ as in the other TM-Ba122 as in Fig. 5.51(b).

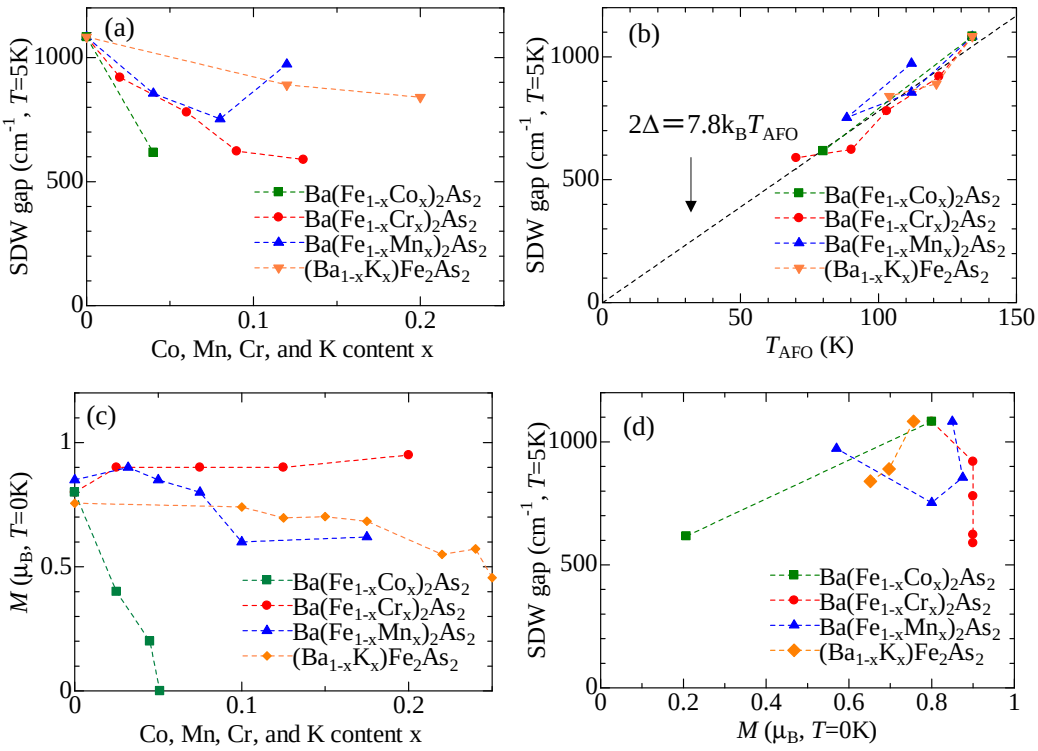

Figure 5.51: (a) Doping dependence of SDW gap energy of $Ba(Fe_{1-x}TM_x)_2As_2$ (TM=Cr, Mn, and Co) and (b) antiferromagnetic transition temperature dependence of SDW gap energy of $Ba(Fe_{1-x}TM_x)_2As_2$ (TM=Cr, Mn, and Co). For the comparison, the data of $(Ba_{1-x}K_x)Fe_2As_2$ in Ref. [122] are also plotted in panels (a) and (b). (c) The doping dependence of the magnetic moment of Fe of $Ba(Fe_{1-x}TM_x)_2As_2$ (TM=Cr, Mn, and Co) and $(Ba_{1-x}K_x)Fe_2As_2$. The data are cited from Refs. [12, 24, 25, 128]. (d) The ordered magnetic moment dependence of the SDW gap energy for $Ba(Fe_{1-x}TM_x)_2As_2$ (TM=Cr, Mn, and Co) and $(Ba_{1-x}K_x)Fe_2As_2$. For Co-Ba122 and Mn-Ba122 with $x = 0.12$, T_{AFO} represents the magnetic transition temperature.

5.5 Magnetic/nonmagnetic impurity effect on the coherent carrier

In this section, I discuss the doping dependence of the Drude components. Drude component can be expressed as follows;

$$\sigma(\omega) = \frac{\omega_p^2}{4\pi} \frac{\tau}{(\omega\tau)^2 + 1} \tag{5.9}$$

Here $1/\tau$ is a scattering rate and $\omega_p \propto \sqrt{n/m^*}$ (n: carrier number, m^*: effective carrier mass) is a plasma frequency. $\sigma(\omega)$ at $\omega = 0$ is correspond to the dc-conductivity value.

Before the discussion of the fitting parameters of the Drude component, I show the temperature dependence of the in-plane resistivity $\rho(T)$ for $Ba(Fe_{1-x}TM_x)_2As_2$ (TM=Co, Cr, and Mn). Figure 5.52(a) shows $\rho(T)$ for Co-Ba122 [60]. $\rho(T)$ for $x = 0$ decreases with lowering the temperature and abruptly decreases at $T_{\rm AFO}$. With further lowering temperature, $\rho(T)$ decreases faster than that above $T_{\rm AFO}$. Naively, $\rho(T)$ is expected to increase below $T_{\rm AFO}$ because the carrier number decreases due to the opening of the SDW gap at a part of the Fermi surface. The result opposite to the expectation indicates that the reduction of $1/\tau$ overcomes the reduction of the carrier number. In the lightly Co-doped Ba122 with $x = 0.04$, $\rho(T)$ shows a jump at the structural transition temperature at $T = 90\,\mathrm{K}$ and saturates at $T \sim 80\,\mathrm{K}$ which corresponds to the magnetic transition temperature. For $x = 0.06$ and 0.08, there is no indication of the magnetostructural transition while the superconducting transition is observed at $T_c \sim 20\,\mathrm{K}$. The absolute value of $\rho(T)$ at room temperature decreases with Co-doping, indicating that the carrier number increases with doping.

For Cr and Mn-Ba122 as shown in Figs. 5.52(b) and (c), $\rho(300\,\mathrm{K})$ increases with doping, indicating that the doped Cr and Mn act as a stronger scatterers than Co. The increasing tendency of $\rho(300\,\mathrm{K})$ continues up to $x \sim 0.10$ but saturates above this composition. $\rho(T)$ for Cr and Mn-Ba122 decreases with lowering temperature, starts to increases above $T \sim T_{\rm AFO}$, and it shows a jump at $T_{\rm AFO}$ where the magnetic and structural transition occurs simultaneously [24, 25]. Below $T_{\rm AFO}$, $\rho(T)$ increases with lowering temperature, which is a contrast to Co-Ba122 where $\rho(T)$ decreases below $T_{\rm AFO}$. $T_{\rm AFO}$ decreases with Cr and Mn-doping but any sign of the superconducting transition is not observed.

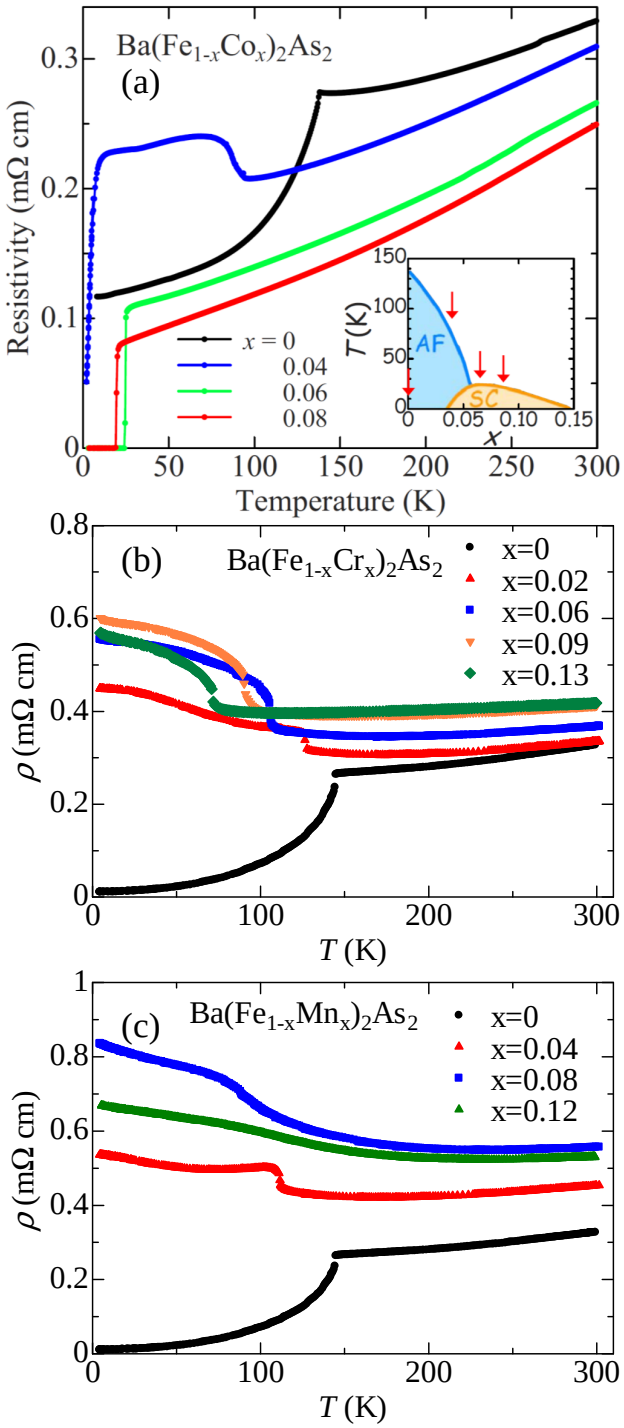

Figure 5.52: Temperature dependence of the in-plane resistivity of $Ba(Fe_{1-x}TM_x)_2As_2$ (TM=Co, Cr, and Mn) with various xs. (a), (b), and (c) show the results for TM=Co, Cr, and Mn, respectively. The figure of $Ba(Fe_{1-x}Co_x)_2As_2$ is cited from Ref. [60].

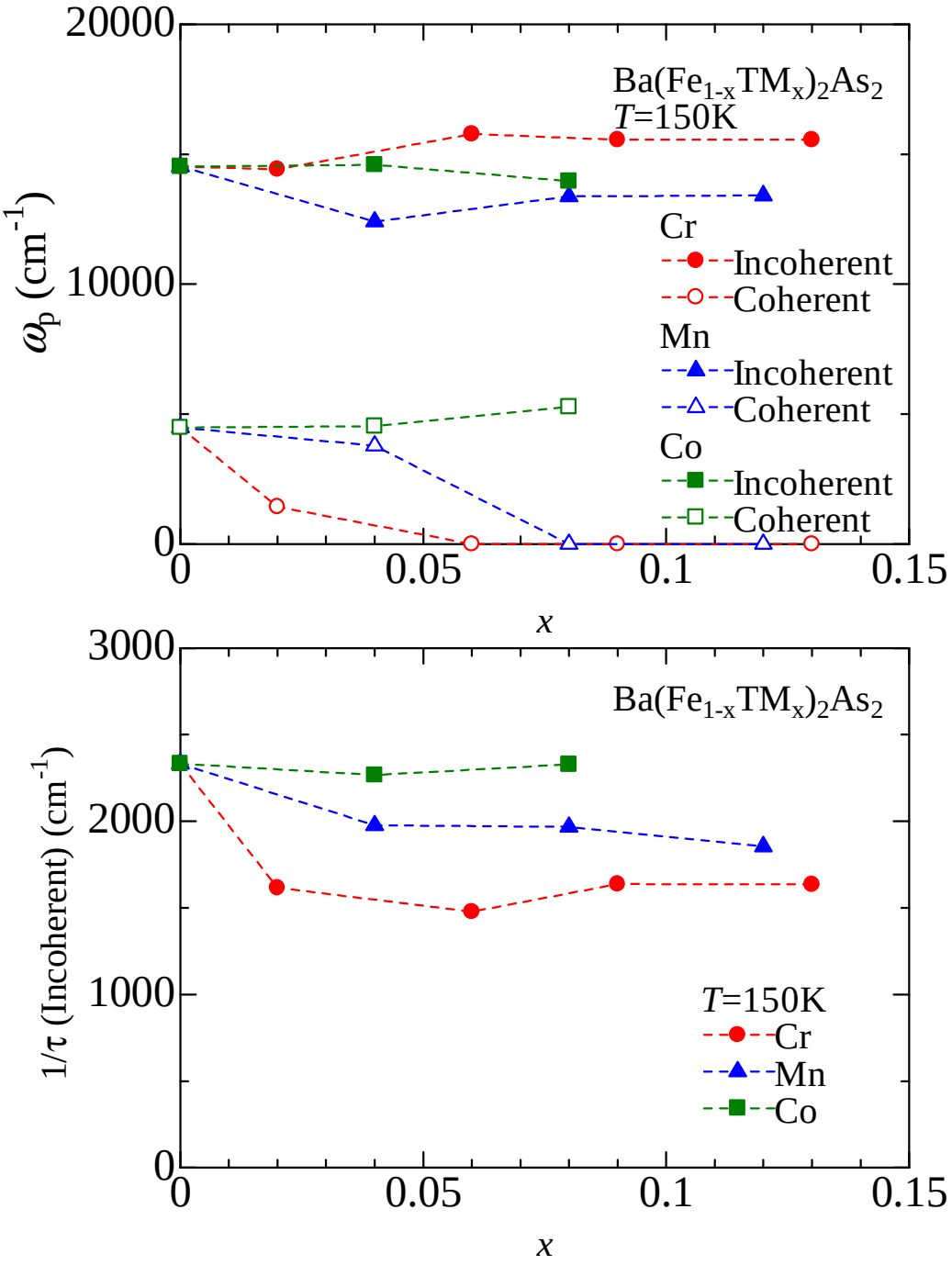

Figure 5.53: (a) Doping dependence of the plasma frequency of coherent (open) and incoherent (closed) component for $Ba(Fe_{1-x}TM_x)_2As_2$ [TM=Cr (red circles) and (Mn) (blue triangles), and Co (green squares)] at 150 K, respectively. (b) Doping dependence of scattering rate of incoherent component for $Ba(Fe_{1-x}TM_x)_2As_2$ [TM=Cr (red circles) and Mn (blue triangles), and Co (green squares), respectively. These are the fitting results of "one Drude" fitting method.

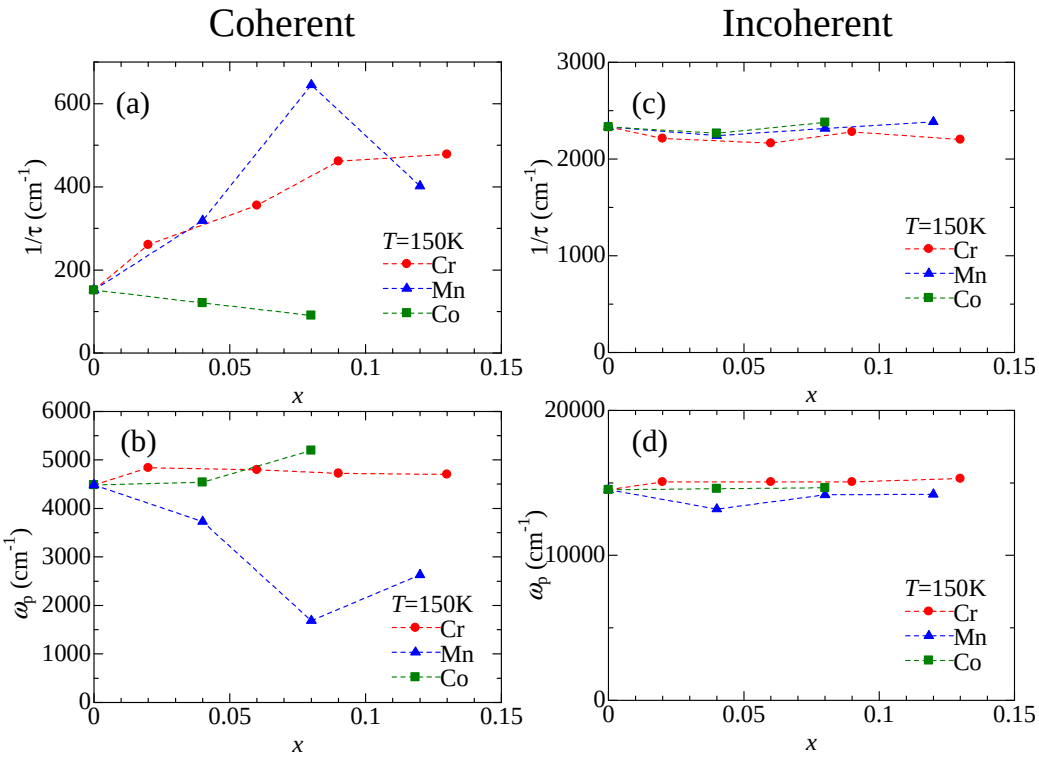

Figure 5.54: Doping dependence of (a), (c) scattering rate and (b), (d) plasma frequency of for $Ba(Fe_{1-x}TM_x)_2As_2$ (TM=Cr, Mn, and Co) at 150 K. (a), (b) are the fitting parameters for the coherent component and (c), (d) are for the incoherent component, respectively in "two Drude" fitting method.

First, I show the fitting results of one Drude method as shown in Figs. 5.53. The fitting results of Co-Ba122 is also shown in Fig. 5.53. As shown in Fig. 5.53(a) and 5.53(b), the plasma frequency $\omega_{\rm p}$ and the scattering rate of $1/\tau$ of the incoherent component saturates as $\omega_{\rm p}$ of the coherent component disappears. These fitting results indicate that the coherent component cannot be distinguished from the incoherent one with increasing Cr and Mn-concentration, and the incoherent component dominates the dc-conductivity.

One of the criteria of the incoherence of the carrier transport is the Mott-Ioffe-Regel (MIR) limit where the mean free path $l_{\rm mfp}$ of the carrier reaches the interatomic spacing ($k_{\rm Fermi}l_{\rm mfp} \sim 1$). In iron-pnictides, there are five quasi-2 dimensional Fermi surfaces in the paramagnetic state. In this case, MIR limit of the conductivity is roughly estimated $\sigma_{\rm MIR} \sim 5 \times (e^2/h)(k_{\rm Fermi}l_{\rm mfp})/c$ (e; elementary charge, h; Planck constant, c; the interlayer spacing, $c \sim 6.6$Å for TM-Ba122), or $\rho_{\rm MIR} \sim 0.35\,({\rm m}\Omega\,cm)$. The resistivity value of Cr/Mn-Ba122 at $T = 150\,{\rm K}$ exceeds the MIR limit with TM-doping as shown in Figs. 5.52(b) and 5.52(c), indicating the carrier transport becomes incoherent. Therefore the fitting with one incoherent Drude component is valid for Cr/Mn-Ba122.

Next, I show the fitting results of the two Drude method with fixing the incoherent component. In this fitting method, I focus on how the coherent component is affected by Cr/Mn-doping and becomes incoherent. Figures 5.54(a)-(d) show the doping dependence of the fitting parameter for the coherent and incoherent Drude component of TM-Ba122 above $T_{\rm AFO}$ (at $T = 150\,{\rm K}$). It is noted that the fitting of Cr and Mn-Ba122 is based on the assumption that the scattering rate and the plasma frequency for the incoherent component do not change so much from those of the parent compound as shown in Figs. 5.54(c) and 5.54(d), because it is almost unchanged in Co-Ba122 and it is needed to reproduce the nearly flat $\sigma(\omega)$ around $2000\,{\rm cm}^{-1}$. Therefore, although there remains an uncertainty of the fitting results, the present fitting results is reasonable, considering the smooth doping evolution of $\sigma(\omega)$ in Cr and Mn-Ba122 from the parent compound.

Figures 5.54(a) and 5.54(b) show the scattering rate and plasma frequency for the coherent component, and Figures 5.54(c) and 5.54(d) for the incoherent component in the paramagnetic phase, respectively. In Co-doped systems, the plasma frequency for the coherent component slightly increases with doping while the scattering rate decreases. This suggests that Co-doping acts as an electron doping and Co atoms substituted for Fe site are quite weak impurity scattering centers. In Cr-doped systems, the plasma fre-

quency for the coherent component is almost unchanged while the scattering rate significantly increases with doping. The small doping dependence of the plasma frequency for the coherent component can be interpreted as follows. Cr-doping introduces holes but doped hole carriers predominantly contribute to the incoherent component. The large scattering rate in Cr-Ba122 indicates that Cr substituted for Fe acts as a strong impurity scattering center for the coherent carrier.

On the other hand, in Mn-doped systems, the scattering rate for the coherent component increases as in the case of Cr-Ba122 while the plasma frequency significantly decreases [See Fig. 5.54(a) and (b)]. This reduction of the plasma frequency is mainly caused by the fitting uncertainty because the low-energy $\sigma(\omega)$ for Mn-Ba122 is too low to fit the spectrum with the coherent component. If I reduce the plasma frequency or increases the scattering rate of the incoherent component to increase the plasma frequency of the coherent component, the fitting results of the spectrum above $1000\,\mathrm{cm}^{-1}$ gets worse. Therefore, I believe that the present fitting results are valid, and conclude that the increase of the scattering rate in Mn-Ba122 is intrinsic. The origin of reduction in the plasma frequency is unclear. One possibility is that it is related to insulator-metal transition considering that $BaMn_2As_2$ has an insulating ground state [137] or the localization of the coherent carriers as discussed in the next section. However, the reduction of the plasma frequency seems inconsistent with the conclusion of the previous part that carrier is almost undoped in Mn-Ba122. To get rid of these discrepancies, the different fitting model from the Drude-Lorentz model may be required. In any case, the strong increasing of the scattering rate of TM-Ba122 (TM=Cr and Mn) indicates that the coherent component gets incoherent and indistinguishable from the incoherent component.

Two different fitting methods shown here demonstrate the same conclusion that the coherent component gets incoherent with Cr and Mn-doping and the incoherent Drude component dominates the dc-conductivity in contrast to the case of Co-Ba122.

Figures 5.55(a) and 5.55(b) show the scattering rate and plasma frequency in the antiferromagnetic phase, respectively. The scattering rate slightly increases with Co-doping up to $x = 0.04$ and it decreases toward $x = 0.08$, while it increases much significantly in Cr and Mn-Ba122. On the other hand, the plasma frequency is almost unchanged with doping in all the TM-Ba122.

These results indicate that both of Cr and Mn act as a stronger scatterer than Co both in the paramagnetic and antiferromagnetic phase. Namely, Cr

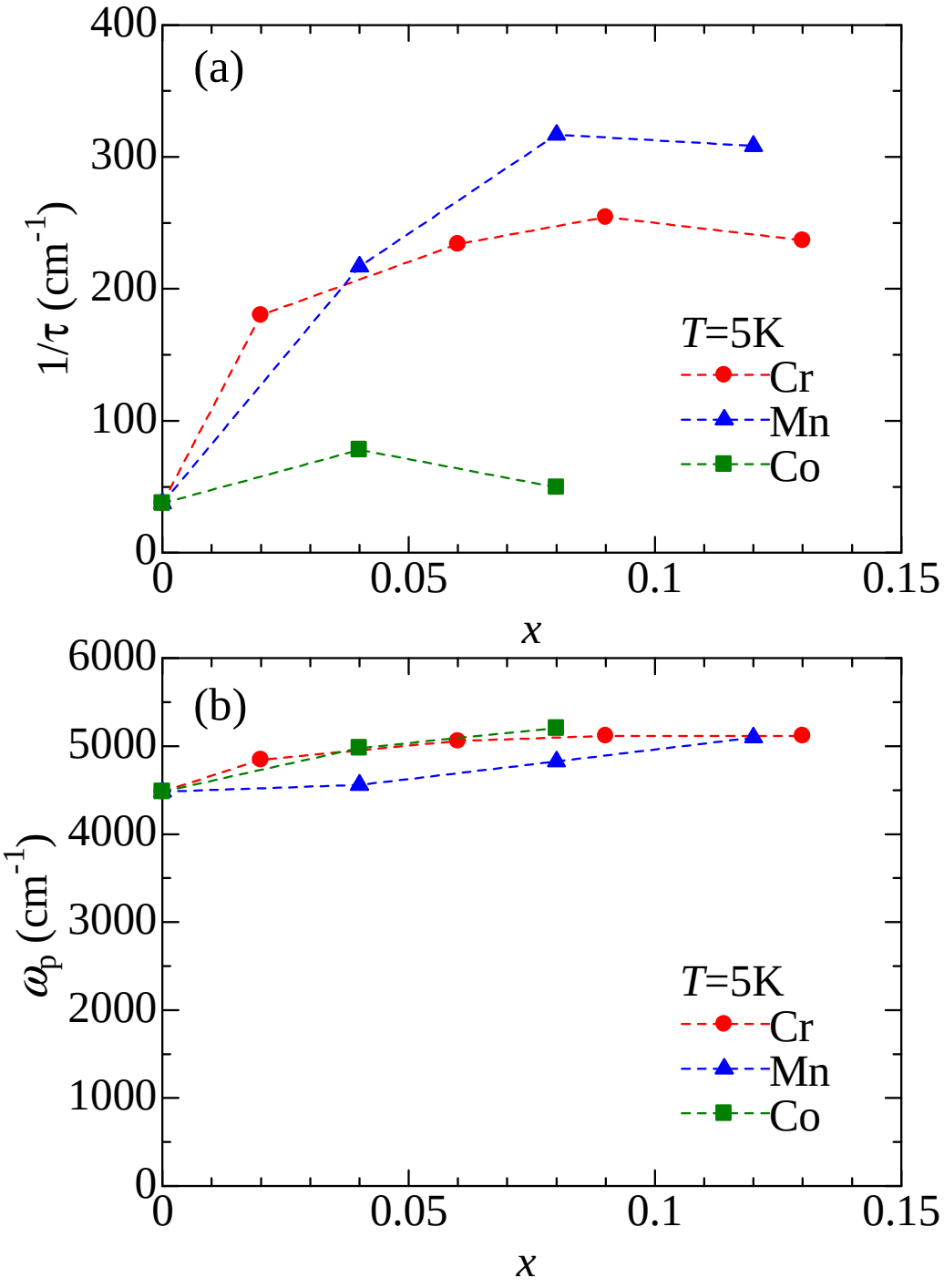

Figure 5.55: Doping dependence of (a) scattering rate and (b) plasma frequency of for $Ba(Fe_{1-x}TM_x)_2As_2$ (TM=Cr, Mn, and Co) at 5 K. For $x = 0.08$ of Co-Ba122, the data at 30 K was used.

and Mn-substitution strongly suppresses the coherent carrier transport in Cr and Mn-Ba122 but only weakly in Co-Ba122. The main difference between these transition metals is that Cr and Mn are magnetic impurities [113, 114] while Co is nonmagnetic impurity [115], indicating that the carrier scattering in iron-pnictides mainly caused by the magnetic scattering.

It is noted that the theoretical study [138] predicts that the suppression of the coherent Drude component can be caused by hole-doping. This suppression of the coherent Drude component derives from the enhancement of the electronic correlation by hole-doping. However, even in KFe_2As_2 which is the end member of hole-doped Ba122, the spectral weight of the coherent Drude component does not change so much [139]. Thus the strong suppression of the coherent component compared with $BaFe_2As_2$ observed in the present study cannot be attributed solely to the hole-doping effect.

5.6 Localized carrier induced by Mn/Cr-doping

Finally, I discuss the localized carrier feature above $T_{\rm AFO}$ observed in Cr and Mn-Ba122. In these doped systems, a peak structure is observed around $200\,{\rm cm}^{-1}$ above $T_{\rm AFO}$, which is not observed in Co-Ba122, and the peak energy increases with doping as shown in Fig. 5.57. The peak structure at a finite frequency is characteristic of localized carriers.

One of the possible origins of this feature is a precursor of the spin-density-wave gap. Actually, it is reported in charge-density-wave material that the localized carrier energy increases with the impurity concentration [140]. However, this is not valid because the localized carrier energy anticorrelates with the SDW gap energy with doping in the present systems, and the peak structure is observed above $T_{\rm AFO}$.

Another possible origin is the excitation from the doped Cr and Mn states, but this is also not relevant for the present systems because the partial density of state of doped Cr and Mn exists at $1 \sim 10\,{\rm eV}$ below the Fermi energy according to the resonance photoemission measurements [66], and it cannot explain the doping dependence of the localized energy.

The third possible origin is the disorder effect. In fact, the similar peak structure is sometimes observed in disordered metals, such as Zn-doped or He-irradiated cuprate superconductors [141, 142]. Thus the present results can be attributed to the disorder effect by Cr and Mn-doping, but this can not explain why such a disorder effect is not observed in Co-Ba122 where disorders are also introduced into Fe-plane.

As discussed above, it is difficult to attribute this origin of the peak structure to an usual impurity effect, suggesting the interplay between the conduction electron and the magnetic impurity should be considered.

A representative interaction between the magnetic impurity and the conduction electron is the Kondo effect [143]. Kondo materials or heavy-fermion systems, such as YbB_{12} and $CeCu_2Si_2$ [144, 145], show a peak structure in the far-infrared energy region. Actually, the temperature dependence of resistivity of Cr and Mn-Ba122 shows a small upturn above $T_{\rm AFO}$ as shown in Fig. 5.52, suggesting the Kondo effect. However, it is suggested by a dynamical mean-field theory [146] that a multiband system with large Hund's coupling J has a significantly reduced Kondo temperature, and large J is required to explain the observed electronic structure of Mn-Ba122 [66]. This is inconsistent with the present observation that the peak structure in $\sigma(\omega)$ is already observed near the room temperature which is much higher than

the expected Kondo temperature. Therefore the present observation can not be explained by the simple Kondo effect.

Another aspect is that magnetic impurities induce a local magnetic order around themselves [136] as shown in Fig. 5.56. In a lower magnetic impurity concentration, magnetic impurity induces local Neel type magnetic order above T_{AF} and it coexists with the original long-range stripe type magnetic order below T_{AF}. In a higher magnetic impurity concentration, Neel and stripe type magnetic orders coexist below T_{AF}, while stripe type magnetic order is dominant even above T_{AF} due to the cooperative magnetic impurity effect. This theory can explain the previous experimental observation in Mn-Ba122 that Neel and stripe type magnetic orders coexist and tetragonal-stripe type magnetic order emerges in the higher doping range [25].

This interaction can cause the strong suppression of the coherent carrier transport, and the peak feature observed in the present study is related to this cooperative effect between magnetic impurities and conduction electrons. Based on this assumption, the difference of the phase diagram in Cr and Mn-Ba122 can be also understood. The increasing rate of the peak energy is larger in Mn-Ba122 than in Cr-Ba122 as shown in Fig. 5.57, suggesting that the interaction strength is different in these systems.

The localization peak abruptly disappears below T_{AFO}, and the SDW gap structure instead appears as shown in Figs. 5.49 and 5.50. This indicates that the localized state disappears due to the reconstruction the electronic structure or the original long-range SDW order that affects the magnetic impurity-induced local magnetic order. This suggests that Cr and Mn acts as more than the mere magnetic impurity in the paramagnetic phase, whereas they still act as the magnetic impurity scattering center in the AFO state, as is seen in the fact that the scattering rate of Cr/Mn-Ba122 in the AFO state is much larger than that of Co-Ba122.

This localization of the coherent carriers by the magnetic Cr and Mn should cause a strong pair-breaking effect for superconductivity, in addition to the short-range Neel fluctuations induced by magnetic impurity which leads to the strong suppression of superconductivity [147, 135]. This is the reason why superconductivity is not observed in Cr and Mn-Ba122 although T_{AFO} is well suppressed down to the temperature at which superconductivity and the AFO state coexist in Co-Ba122.

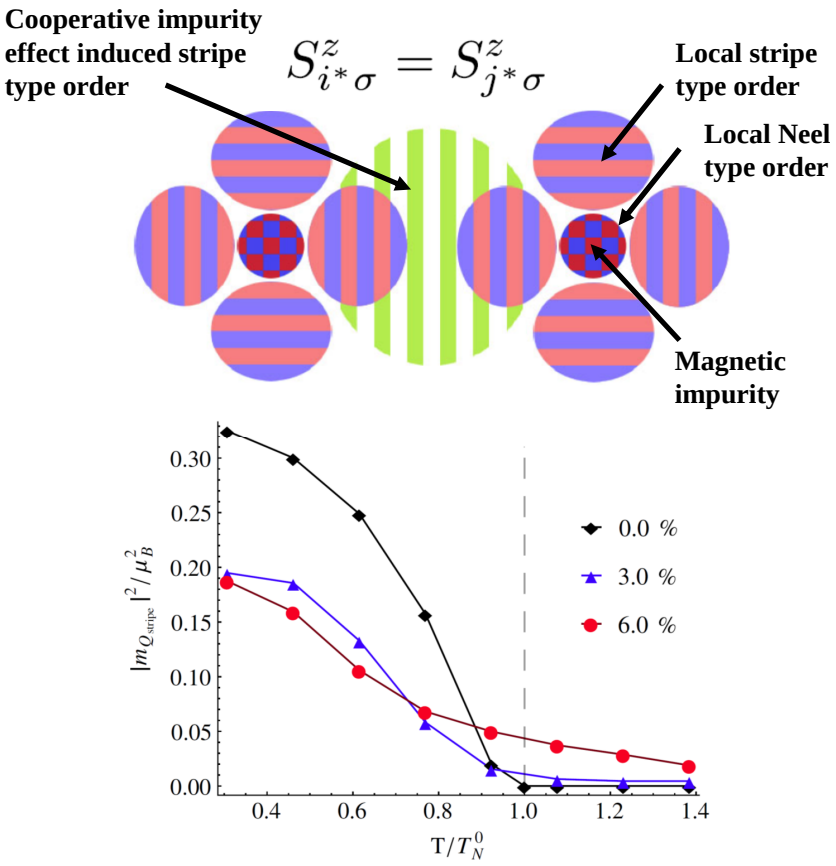

Figure 5.56: (Upper panel) The schematic picture of the magnetic impurity induced local magnetic order and its constructive interference between the magnetic impurities. (Bottom panel) Theoretical calculation of the temperature dependence of the magnetic $\boldsymbol{q} = \boldsymbol{Q}_{\rm stripe}$ Bragg peak for the homogeneous system (black diamonds), $x = 0.03$ (blue triangles) disorder, and $x = 0.06$ (red dots) disorder for $Ba(Fe_{1-x}Mn_x)_2As_2$. Vertical dashed line indicates $T = T_N^0$. The figures are cited from Ref. [136].

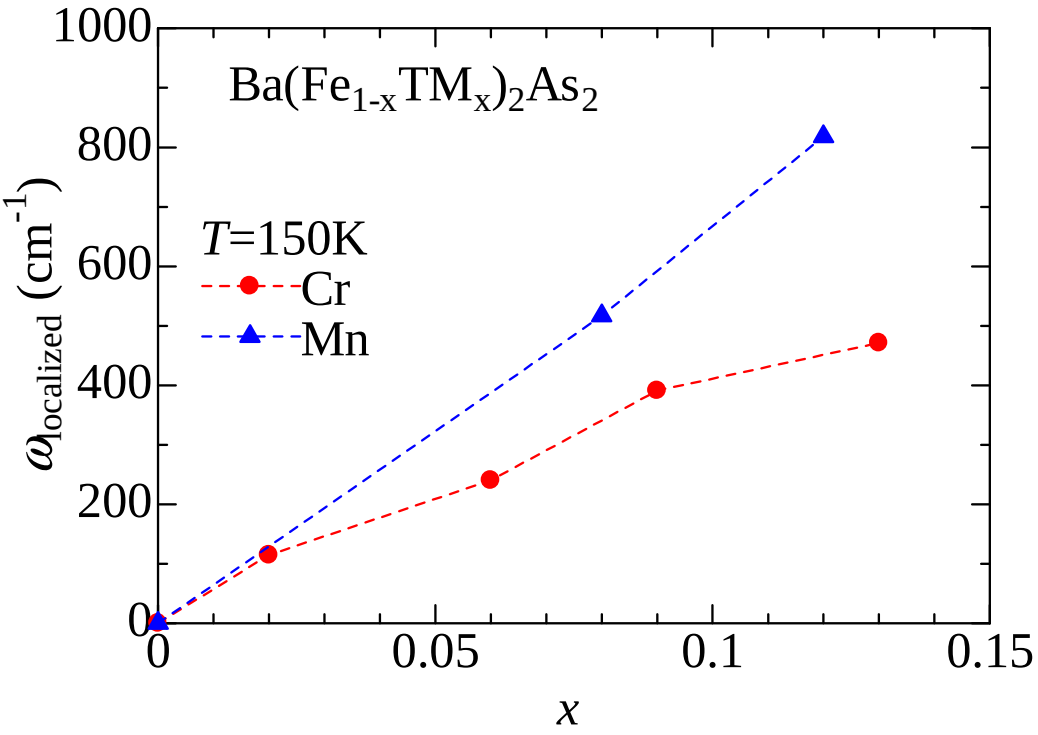

Figure 5.57: Doping dependence of localized carrier peak at 150 K for $Ba(Fe_{1-x}TM_x)_2As_2$ (TM=Cr and Mn).

5.7 Summary

I performed optical conductivity measurements in TM-Ba122. I found that the coherent component of optical conductivity is strongly suppressed by magnetic Mn and Cr-doping while it is robust against Co-doping both in the paramagnetic and the antiferromagnetic state. This result indicates that the coherent carriers are strongly scattered by magnetic impurity but not by nonmagnetic impurity in iron pnictieds. In addition, the localized carrier feature is observed above T_{AFO} in Cr and Mn-Ba122, which is not observed in Co-Ba122. It is proposed that this localization of carriers is related to the cooperative effect between magnetic impurity and conduction electrons. Eventually this interaction leads to the strong suppression of the coherent carrier transport in the normal state, resulting in the disappearance of superconductivity in Cr and Mn-Ba122.

Part VI

Conclusion

In this study, I have investigated the unusual electronic properties in normal and superconducting phase of iron-pnictide superconductors by performing the transport, magnetization, specific heat, single crystal x-ray diffraction, and optical spectra measurement. I have revealed that the electronic properties including the superconducting, the AFO, and the paramagnetic state are drastically changed by the structural change, carrier-doping, and impurity scattering.

6.1 Crystal structure and superconductivity property in $SrFe_2(As_{1-x}P_x)_2$

In part III, I discuss the relationship between the crystal structure and the superconducting properties in $SrFe_2(As_{1-x}P_x)_2$. The main results are as follows:

- The postannealing treatment of $SrFe_2(As_{1-x}P_x)_2$ is highly effective. The optimal T_c of $SrFe_2(As_{1-x}P_x)_2$ is enhanced from 30 K for the as-grown crystals to 33 K for the annealed one. The single crystal x-ray diffraction measurement revealed that the lattice parameters, in particular the pnictogen height from the Fe-plane, are increased by the postannealing, which leads to the enhancement of T_c

- The doping dependence of T_c in $SrFe_2(As_{1-x}P_x)_2$ is quite similar to that of $BaFe_2(As_{1-x}P_x)_2$, in spite of the large difference of lattice constants in these systems. This similarity comes from the same value of the pnictogen height at the optimal composition both in $SrFe_2(As_{1-x}P_x)_2$ and $BaFe_2(As_{1-x}P_x)_2$.

- The magnetic field dependence of the residual electronic specific heat coefficient shows H-linear dependence in the annealed crystal and sub-H-linear dependence in the as-grown one, suggesting that $SrFe_2(As_{1-x}P_x)_2$ has $s_{\pm}$-wave full gaps with different size. On the other hand, NMR and penetration depth measurement indicated that $SrFe_2(As_{1-x}P_x)_2$ has a nodal gap. These results demonstrate that $SrFe_2(As_{1-x}P_x)_2$ is a multi-band $s_{\pm}$-wave superconductor with an accidental node on the part of the Fermi surfaces.

The comparative study of $SrFe_2(As_{1-x}P_x)_2$ and $BaFe_2(As_{1-x}P_x)_2$ in terms of the crystal structure revealed that the pnictogen height h_{Pn}/As-Fe-As bond-angle α play a more important role for T_c than lattice constants. The previous studies also suggested the importance of h_{Pn}/α for T_c, but they compared the materials with different carrier doping level and lattice constants. Thus, the present study using isovalent-doping systems with different lattice constants has a very important meaning to demonstrate that h_{Pn} and α are indeed crucial for T_c.

In addition, specific heat measurement of as-grown and annealed crystals revealed that superconducting properties is sensitive to disorders. The sensitivity of superconducting properties to disorders also appears in the different response of T_c by the annealing treatment in underdoped and overdoped samples, suggesting the $s_{\pm}$-wave superconductivity.

The importance of the magnetic fluctuation is also demonstrated by the NMR and other measurements using the crystals grown in this study, which is consistent with $s_{\pm}$-wave superconductivity. On the other hand, the photoemission measurement using my crystals revealed that the key orbitals for the superconductivity in FeSC is d_{xy} and/or $d_{xz/yz}$ orbitals, whereas d_{z^2} orbital is unimportant for superconductivity. All these results can be naturally explained by the spin-fluctuation mechanism for superconductivity.

6.2 Resistivity anisotropy in $Ba(Fe_{1-x}TM_x)_2As_2$ (TM=Cr, Mn, and Co)

In part IV, I discussed the origin of the in-plane resistivity anisotropy in $Ba(Fe_{1-x}TM_x)_2As_2$ (TM=Cr, Mn, and Co; TM-Ba122). The main results of this part are as follows:

- The in-plane resistivity anisotropy in the antiferromagnetic-orthorhombic (AFO) phase increases with substitution in Co-Ba122 and Mn-Ba122 while it decreases and shows a sign-change in Cr-Ba122.

- Hall effect measurement revealed that R_H at T_{AFO} changes the sign from negative to positive in Cr-Ba122, while the sign of R_H at T_{AFO} does not change in Mn-Ba122. This implies that Cr-Ba122 is hole-doped system, while Mn-Ba122 is almost undoped system.

- The in-plane resistivity anisotropy in the nematic phase also shows the electron-hole asymmetry in Co and Cr-Ba122, suggesting that the spin-fluctuating scattering mechanism is dominant in the nematic phase.

The comparative study of $Ba(Fe_{1-x}TM_x)_2As_2$ (TM=Cr, Mn, and Co) clarified the origin of the in-plane resistivity anisotropy. The in-plane resistivity anisotropy shows a clear electron/hole-doping asymmetry in the AFO and the nematic phase. In the previous studies, it was proposed that the anisotropic impurity state in the conduction layer results in the anisotropic in-plane resistivity, and the different magnitude of the resistivity anisotropy in different iron-pnictides depends on the impurity scattering strength. However, the previous studies could not distinguish the effect of the carrier doping and the doped site dependences. My result clearly demonstrates that the in-plane resistivity anisotropy is electron/hole asymmetric both in the AFO and the nematic phase by comparing the different carrier-doped but the same site substituted Ba122. These results cannot be attributed to the strength of the impurity scattering alone. It is required to consider both the impurity scattering effect and the topology of the Fermi surface for the in-plane resistivity anisotropy in the AFO phase. The asymmetry in the nematic phase indicates that the carrier transport above the magnetic transition temperature is dominated by the spin-fluctuation scattering which depends on the Fermi surface topology.

The present study demonstrates that the resistivity anisotropy exhibits electron-hole asymmetry in both AFO and nematic phases and that it depends on the Fermi surface topology whether the carrier scattering results in a positive or negative $\delta\rho = \rho_b - \rho_a$.

6.3 Optical conductivity in $Ba(Fe_{1-x}TM_x)_2As_2$ (TM=Cr, Mn, and Co)

In part V, I discussed the doping dependence of the optical conductivity in $Ba(Fe_{1-x}TM_x)_2As_2$ (TM=Cr, Mn, and Co; TM-Ba122). The main results of this part are as follows:

- The magnetic transition temperature is proportional to the SDW gap energy with $2\Delta = 7.8 k_B T_{AFO}$ over a wide doping range. On the other hand, the ordered magnetic moment does not correlate with the SDW gap energy.

- In Mn-Ba122 with $x = 0.12$, where the tetragonal-antiferromagnetic phase is proposed, the antiferromagnetic gap opens below the magnetic transition temperature as in other underdoped iron-pnictides.

- The coherent component of the optical conductivity is strongly suppressed by the magnetic impurity (Cr/Mn), while it is robust against the nonmagnetic impurity (Co) both below and above T_{AFO}.

- In Cr and Mn-Ba122, a peak is observed in the far-infrared region in the paramagnetic phase, which is not observed in Co-Ba122. This feature can be ascribed to the collective effect between magnetic impurities and conduction electrons in iron-pnictides.

I found that the SDW gap energy well correlates with T_{AFO}, while it does not correlate with the ordered magnetic moment, in contrast to the theoretical prediction. This suggests that $\mathrm{Ba(Fe_{1-}}_x\mathrm{TM}_x)_2\mathrm{As}_2$ shares the common origin of the magnetic transition but further theoretical study is required. The structural change and carrier-doping effect should be taken into account to understand the nature of the magnetic state of iron-pnictides.

The optical measurement revealed that the coherent charge transport shows a different response to Co and Cr/Mn-doping. This difference cannot be explained by the electron-hole asymmetry of Co and Cr/Mn-doping. Rather the response to impurity doping depends on whether the impurity is nonmagnetic (Co) or magnetic (Cr/Mn).

Moreover, the novel localized state is induced by the interaction between the magnetic impurity and the conduction electrons in Cr/Mn-Ba122. This interpretation naturally explains that the strong suppression of the coherent carrier transport is caused by the collective effect of the magnetic impurity and the conduction electrons, resulting in the disappearance of superconductivity in Cr/Mn-Ba122.

6.4 Summary

The present study revealed that the superconducting phase in FeSC can be understood in terms of the spin-fluctuation mediated $s_{\pm}$-wave superconducting mechanism with impurity scattering. It is important to use clean crystals for investigating the intrinsic superconducting properties of FeSC

because T_c of FeSC is quite sensitive to the annealing treatment as shown in this study.

My study demonstrates that the in-plane resistivity anisotropy in FeSC shows electron-hole asymmetry. This indicates that the electronic anisotropy of FeSC depends on the topology of the Fermi surface. In particular, the spin-fluctuation scattering depending on the Fermi surface topology is suggested to be dominant in the paramagnetic phase. Considering the superconducting phase also shows electron-hole asymmetry, the electron-hole asymmetric electronic anisotropy indicates that the spin-fluctuation plays an important role for superconducting mechanism of FeSC.

The magnetic impurities in the paramagnetic phase of FeSC play a unique role, which induces local magnetic order around impurities due to the interaction between the impurity and conduction electron, and the collective effect of magnetic impurities can result in the long-range magnetic order. These novel magnetic impurity effects suppress the emergence of superconductivity in Cr/Mn-substituted iron-pnictides.

These results can be understood as the result of the magnetic fluctuation in the paramagnetic state of FeSC. The magnetic fluctuation acts as a glue for the Cooper-pairing in the superconducting state. The carrier scattering by the magnetic fluctuation is anisotropic and depends on the shape of the Fermi surface which can be tuned by the carrier doping. The magnetic impurities interacts with the spin of the conduction electrons and pins the magnetic fluctuation around it, resulting the local magnetic order. The present study demonstrates that the magnetic fluctuation is the crucial ingredient which dominates the electronic properties of FeSC.

I believe that these results contribute to elucidating the superconducting mechanism and normal electronic properties of the iron-based superconductor.

6.5 Future work

For the superconducting state of $SrFe_2(As_{1-x}P_x)_2$, the position of the node on the superconducting gap in the momentum space still remains an open issue. The investigation of the node position by ARPES or other momentum-resolved probe, such as Raman spectroscopy will give more information about the superconductivity in iron-pnictides.

The in-plane resistivity anisotropy shows the electron-hole asymmetry.

In Co-doped systems, the STM measurement revealed that the anisotropic impurity state emerges around Co atoms and it is related to the anisotropic resistivity. The STM investigation on the hole-doped systems where the resistivity anisotropy changes the sign will be useful for understanding the impurity state in the antiferromagnetic and paramagnetic state.

Similarly, other anisotropic properties, such as the thermopower, Raman scattering response, orbital order, low-energy spin excitations should be studied in terms of the electron-hole asymmetry. Transition metal substituted $Ba(Fe_{1-x}TM_x)_2As_2$ (TM=Cr, Mn and Co) is a good platform for such a study.

The optical study of $Ba(Fe_{1-x}TM_x)_2As_2$ (TM=Cr and Mn) with detwinned crystals is also meaningful. The previous study of Co-Ba122 revealed that the anisotropy of conductivity in the high-energy region decreases with Co-doping while the anisotropy of the dc-conductivity increases in the AFO state. Hole-doping effect on the anisotropy in the high-energy region of the conductivity should be addressed. In the present study, the localization feature is observed in Cr/Mn-Ba122. The optical measurement with detwinned crystals will reveal whether this localized feature is anisotropic or not. In addition, the resistivity or optical measurement under the magnetic field is required to reveal the nature of the localized state.

It is also important to reveal the electronic structure in Cr and Mn-Ba122. The present study demonstrates that hole-carrier is doped in Cr-Ba122 but almost undoped in Mn-Ba122. This should be confirmed by other measurement, such as ARPES or Seebeck coefficient measurement.

Bibliography

[1] Yoichi Kamihara, Takumi Watanabe, Masahiro Hirano, and Hideo Hosono. Iron-based layered superconductor La[$O_{1-x}F_x$]FeAs ($x = 0.05-0.12$) with $T_c = 26$ K. *Journal of the American Chemical Society*, Vol. 130, No. 11, pp. 3296–3297, 2008.

[2] Ren Zhi-An, Lu Wei, Yang Jie, Yi Wei, Shen Xiao-Li, Zheng-Cai, Che Guang-Can, Dong Xiao-Li, Sun Li-Ling, Zhou Fang, and Zhao Zhong-Xian. Superconductivity at 55 K in Iron-Based F-Doped Layered Quaternary Compound Sm[$O_{1-x}F_x$]. *Chinese Physics Letters*, Vol. 25, No. 6, p. 2215, 2008.

[3] Shaolong He, Junfeng He, Wenhao Zhang, Lin Zhao, Defa Liu, Xu Liu, Daixiang Mou, Yun-Bo Ou, Qing-Yan Wang, Zhi Li, et al. Phase diagram and electronic indication of high-temperature superconductivity at 65 K in single-layer FeSe films. *Nature materials*, Vol. 12, No. 7, pp. 605–610, 2013.

[4] J George Bednorz and K Alex Müller. Possible high T_c superconductivity in the Ba-La-Cu-O system. *Zeitschrift für Physik B Condensed Matter*, Vol. 64, No. 2, pp. 189–193, 1986.

[5] Johnpierre Paglione and Richard L Greene. High-temperature superconductivity in iron-based materials. *Nature Physics*, Vol. 6, No. 9, pp. 645–658, 2010.

[6] G. R. Stewart. Superconductivity in iron compounds. *Rev. Mod. Phys.*, Vol. 83, pp. 1589–1652, Dec 2011.

[7] PJ Hirschfeld, MM Korshunov, and II Mazin. Gap symmetry and structure of Fe-based superconductors. *Reports on Progress in Physics*, Vol. 74, No. 12, p. 124508, 2011.

[8] Pengcheng Dai. Antiferromagnetic order and spin dynamics in iron-based superconductors. *Rev. Mod. Phys.*, Vol. 87, pp. 855–896, Aug 2015.

[9] Hideo Hosono and Kazuhiko Kuroki. Iron-Based Superconductors: current status of materials and pairing mechanism. *Physica C: Superconductivity and its Applications*, Vol. 514, pp. 399–422, 2015.

[10] Marianne Rotter, Marcus Tegel, and Dirk Johrendt. Superconductivity at 38 K in the Iron Arsenide $(Ba_{1-x}K_x)Fe_2As_2$. *Phys. Rev. Lett.*, Vol. 101, p. 107006, Sep 2008.

[11] M D Lumsden and A D Christianson. Magnetism in Fe-based superconductors. *Journal of Physics: Condensed Matter*, Vol. 22, No. 20, p. 203203, 2010.

[12] C. Lester, Jiun-Haw Chu, J. G. Analytis, S. C. Capelli, A. S. Erickson, C. L. Condron, M. F. Toney, I. R. Fisher, and S. M. Hayden. Neutron scattering study of the interplay between structure and magnetism in $Ba(Fe_{1-x}Co_x)_2As_2$. *Phys. Rev. B*, Vol. 79, p. 144523, Apr 2009.

[13] S. Avci, O. Chmaissem, E. A. Goremychkin, S. Rosenkranz, J.-P. Castellan, D. Y. Chung, I. S. Todorov, J. A. Schlueter, H. Claus, M. G. Kanatzidis, A. Daoud-Aladine, D. Khalyavin, and R. Osborn. Magnetoelastic coupling in the phase diagram of $Ba_{1-x}K_xFe_2As_2$ as seen via neutron diffraction. *Phys. Rev. B*, Vol. 83, p. 172503, May 2011.

[14] J. M. Allred, K. M. Taddei, D. E. Bugaris, S. Avci, D. Y. Chung, H. Claus, C. dela Cruz, M. G. Kanatzidis, S. Rosenkranz, R. Osborn, and O. Chmaissem. Coincident structural and magnetic order in $BaFe_2(As_{1-x}P_x)_2$ revealed by high-resolution neutron diffraction. *Phys. Rev. B*, Vol. 90, p. 104513, Sep 2014.

[15] Lijun Zhang and D. J. Singh. Electronic structure of $Ba(Fe,Ru)_2As_2$ and $Sr(Fe,Ir)_2As_2$ alloys. *Phys. Rev. B*, Vol. 79, p. 174530, May 2009.

[16] II Mazin and J Schmalian. Pairing symmetry and pairing state in ferropnictides: Theoretical overview. *Physica C: Superconductivity*, Vol. 469, No. 9, pp. 614–627, 2009.

[17] P Richard, T Qian, and H Ding. ARPES measurements of the superconducting gap of Fe-based superconductors and their implications to the pairing mechanism. *Journal of Physics: Condensed Matter*, Vol. 27, No. 29, p. 293203, 2015.

[18] A Carrington. Quantum oscillation studies of the Fermi surface of iron-pnictide superconductors. *Reports on Progress in Physics*, Vol. 74, No. 12, p. 124507, 2011.

[19] Ming Yi, Donghui Lu, Jiun-Haw Chu, James G Analytis, Adam P Sorini, Alexander F Kemper, Brian Moritz, Sung-Kwan Mo, Rob G Moore, Makoto Hashimoto, et al. Symmetry-breaking orbital anisotropy observed for detwinned $Ba(Fe_{1-x}Co_x)_2As_2$ above the spin density wave transition. *Proceedings of the National Academy of Sciences*, Vol. 108, No. 17, pp. 6878–6883, 2011.

[20] D. J. Scalapino. A common thread: The pairing interaction for unconventional superconductors. *Rev. Mod. Phys.*, Vol. 84, pp. 1383–1417, Oct 2012.

[21] M. G. Kim, D. K. Pratt, G. E. Rustan, W. Tian, J. L. Zarestky, A. Thaler, S. L. Bud'ko, P. C. Canfield, R. J. McQueeney, A. Kreyssig, and A. I. Goldman. Magnetic ordering and structural distortion in Ru-doped $BaFe_2As_2$ single crystals studied by neutron and x-ray diffraction. *Phys. Rev. B*, Vol. 83, p. 054514, Feb 2011.

[22] E. Colombier, S. L. Bud'ko, N. Ni, and P. C. Canfield. Complete pressure-dependent phase diagrams for $SrFe_2As_2$ and $BaFe_2As_2$. *Phys. Rev. B*, Vol. 79, p. 224518, Jun 2009.

[23] S. Kasahara, T. Shibauchi, K. Hashimoto, K. Ikada, S. Tonegawa, R. Okazaki, H. Shishido, H. Ikeda, H. Takeya, K. Hirata, T. Terashima, and Y. Matsuda. Evolution from non-Fermi- to Fermi-liquid transport via isovalent doping in $BaFe_2(As_{1-x}P_x)_2$ superconductors. *Phys. Rev. B*, Vol. 81, p. 184519, May 2010.

[24] K. Marty, A. D. Christianson, C. H. Wang, M. Matsuda, H. Cao, L. H. VanBebber, J. L. Zarestky, D. J. Singh, A. S. Sefat, and M. D. Lumsden. Competing magnetic ground states in nonsuperconducting $Ba(Fe_{1-x}Cr_x)_2As_2$ as seen via neutron diffraction. *Phys. Rev. B*, Vol. 83, p. 060509, Feb 2011.

[25] M. G. Kim, A. Kreyssig, A. Thaler, D. K. Pratt, W. Tian, J. L. Zarestky, M. A. Green, S. L. Bud'ko, P. C. Canfield, R. J. McQueeney, and A. I. Goldman. Antiferromagnetic ordering in the absence of structural distortion in $Ba(Fe_{1-x}Mn_x)_2As_2$. *Phys. Rev. B*, Vol. 82, p. 220503, Dec 2010.

[26] Hiroshi Kontani and Seiichiro Onari. Orbital-Fluctuation-Mediated Superconductivity in Iron Pnictides: Analysis of the Five-Orbital Hubbard-Holstein Model. *Phys. Rev. Lett.*, Vol. 104, p. 157001, Apr 2010.

[27] Mitsuharu Yashima, Hideaki Nishimura, Hidekazu Mukuda, Yoshio Kitaoka, Kiichi Miyazawa, Parasharam M. Shirage, Kunihiro Kihou, Hijiri Kito, Hiroshi Eisaki, and Akira Iyo. Strong-coupling spin-singlet superconductivity with multiple full gaps in hole-doped $Ba_{0.6}K_{0.4}Fe_2As_2$ probed by ^{57}Fe-NMR. *Journal of the Physical Society of Japan*, Vol. 78, No. 10, p. 103702, 2009.

[28] P. Popovich, A. V. Boris, O. V. Dolgov, A. A. Golubov, D. L. Sun, C. T. Lin, R. K. Kremer, and B. Keimer. Specific Heat Measurements of $Ba_{0.68}\mathbf{K}_{0.32}Fe_2As_2$ Single Crystals: Evidence for a Multiband Strong-Coupling Superconducting State. *Phys. Rev. Lett.*, Vol. 105, p. 027003, Jul 2010.

[29] X. G. Luo, M. A. Tanatar, J.-Ph. Reid, H. Shakeripour, N. Doiron-Leyraud, N. Ni, S. L. Bud'ko, P. C. Canfield, Huiqian Luo, Zhaosheng Wang, Hai-Hu Wen, R. Prozorov, and Louis Taillefer. Quasiparticle heat transport in single-crystalline $Ba_{1-x}K_xFe_2As_2$: Evidence for a k-dependent superconducting gap without nodes. *Phys. Rev. B*, Vol. 80, p. 140503, Oct 2009.

[30] K. Hashimoto, T. Shibauchi, S. Kasahara, K. Ikada, S. Tonegawa, T. Kato, R. Okazaki, C. J. van der Beek, M. Konczykowski, H. Takeya, K. Hirata, T. Terashima, and Y. Matsuda. Microwave Surface-Impedance Measurements of the Magnetic Penetration Depth in Single Crystal $Ba_{1-x}\mathbf{K}_xFe_2As_2$ Superconductors: Evidence for a Disorder-Dependent Superfluid Density. *Phys. Rev. Lett.*, Vol. 102, p. 207001, May 2009.

[31] G. Li, W. Z. Hu, J. Dong, Z. Li, P. Zheng, G. F. Chen, J. L. Luo, and N. L. Wang. Probing the Superconducting Energy Gap from Infrared Spectroscopy on a $Ba_{0.6}K_{0.4}Fe_2As_2$ Single Crystal with $T_c = 37$ K. *Phys. Rev. Lett.*, Vol. 101, p. 107004, Sep 2008.

[32] T Hanaguri, S Niitaka, K Kuroki, and H Takagi. Unconventional s-wave superconductivity in Fe (Se, Te). *Science*, Vol. 328, No. 5977, pp. 474–476, 2010.

[33] AD Christianson, EA Goremychkin, R Osborn, S Rosenkranz, MD Lumsden, CD Malliakas, IS Todorov, H Claus, DY Chung, MG Kanatzidis, et al. Unconventional superconductivity in $Ba_{0.6}K_0.4Fe_2As_2$ from inelastic neutron scattering. *Nature*, Vol. 456, No. 7224, pp. 930–932, 2008.

[34] K Nakayama, T Sato, P Richard, Y-M Xu, Y Sekiba, S Souma, GF Chen, JL Luo, NL Wang, H Ding, et al. Superconducting gap symmetry of $Ba_{0.6}K_{0.4}Fe_2As_2$ studied by angle-resolved photoemission spectroscopy. *EPL (Europhysics Letters)*, Vol. 85, No. 6, p. 67002, 2009.

[35] K. Hashimoto, M. Yamashita, S. Kasahara, Y. Senshu, N. Nakata, S. Tonegawa, K. Ikada, A. Serafin, A. Carrington, T. Terashima, H. Ikeda, T. Shibauchi, and Y. Matsuda. Line nodes in the energy gap of superconducting $BaFe_2(As_{1-x}P_x)_2$ single crystals as seen via penetration depth and thermal conductivity. *Phys. Rev. B*, Vol. 81, p. 220501, Jun 2010.

[36] X. Qiu, S. Y. Zhou, H. Zhang, B. Y. Pan, X. C. Hong, Y. F. Dai, Man Jin Eom, Jun Sung Kim, Z. R. Ye, Y. Zhang, D. L. Feng, and S. Y. Li. Robust Nodal Superconductivity Induced by Isovalent Doping in $Ba(Fe_{1-x}Ru_x)_2As_2$ and $BaFe_2(As_{1-x}P_x)_2$. *Phys. Rev. X*, Vol. 2, p. 011010, Feb 2012.

[37] K. Hashimoto, A. Serafin, S. Tonegawa, R. Katsumata, R. Okazaki, T. Saito, H. Fukazawa, Y. Kohori, K. Kihou, C. H. Lee, A. Iyo, H. Eisaki, H. Ikeda, Y. Matsuda, A. Carrington, and T. Shibauchi. Evidence for superconducting gap nodes in the zone-centered hole bands of KFe_2As_2 from magnetic penetration-depth measurements. *Phys. Rev. B*, Vol. 82, p. 014526, Jul 2010.

[38] CH Lee, K Kihou, A Iyo, H Kito, PM Shirage, and H Eisaki. Relationship between crystal structure and superconductivity in iron-based superconductors. *Solid State Communications*, Vol. 152, No. 8, pp. 644–648, 2012.

[39] Y Mizuguchi, Y Hara, K Deguchi, S Tsuda, T Yamaguchi, K Takeda, H Kotegawa, H Tou, and Y Takano. Anion height dependence of T_c for the Fe-based superconductor. *Superconductor Science and Technology*, Vol. 23, No. 5, p. 054013, 2010.

[40] K. Hashimoto, S. Kasahara, R. Katsumata, Y. Mizukami, M. Yamashita, H. Ikeda, T. Terashima, A. Carrington, Y. Matsuda, and T. Shibauchi. Nodal versus Nodeless Behaviors of the Order Parameters of LiFeP and LiFeAs Superconductors from Magnetic Penetration-Depth Measurements. *Phys. Rev. Lett.*, Vol. 108, p. 047003, Jan 2012.

[41] S. R. Saha, N. P. Butch, K. Kirshenbaum, and Johnpierre Paglione. Evolution of bulk superconductivity in $SrFe_2As_2$ with Ni substitution. *Phys. Rev. B*, Vol. 79, p. 224519, Jun 2009.

[42] Yasuyuki Nakajima, Toshihiro Taen, Yuji Tsuchiya, Tsuyoshi Tamegai, Hisashi Kitamura, and Takeshi Murakami. Suppression of the critical temperature of superconducting $Ba(Fe_{1-x}Co_x)_2As_2$ by point defects from proton irradiation. *Phys. Rev. B*, Vol. 82, p. 220504, Dec 2010.

[43] I R Fisher, L Degiorgi, and Z X Shen. In-plane electronic anisotropy of underdoped '122' Fe-arsenide superconductors revealed by measurements of detwinned single crystals. *Reports on Progress in Physics*, Vol. 74, No. 12, p. 124506, 2011.

[44] RM Fernandes, AV Chubukov, and J Schmalian. What drives nematic order in iron-based superconductors? *Nature physics*, Vol. 10, No. 2, pp. 97–104, 2014.

[45] Jiun-Haw Chu, James G Analytis, Kristiaan De Greve, Peter L McMahon, Zahirul Islam, Yoshihisa Yamamoto, and Ian R Fisher. In-plane resistivity anisotropy in an underdoped iron arsenide superconductor. *Science*, Vol. 329, No. 5993, pp. 824–826, 2010.

[46] Hsueh-Hui Kuo and Ian R. Fisher. Effect of Disorder on the Resistivity Anisotropy Near the Electronic Nematic Phase Transition in Pure and

Electron-Doped $BaFe_2As_2$. *Phys. Rev. Lett.*, Vol. 112, p. 227001, Jun 2014.

[47] Y. K. Kim, W. S. Jung, G. R. Han, K.-Y. Choi, C.-C. Chen, T. P. Devereaux, A. Chainani, J. Miyawaki, Y. Takata, Y. Tanaka, M. Oura, S. Shin, A. P. Singh, H. G. Lee, J.-Y. Kim, and C. Kim. Existence of Orbital Order and its Fluctuation in Superconducting $Ba(Fe_{1-x}Co_x)_2As_2$ Single Crystals Revealed by X-ray Absorption Spectroscopy. *Phys. Rev. Lett.*, Vol. 111, p. 217001, Nov 2013.

[48] M. Nakajima, S. Ishida, Y. Tomioka, K. Kihou, C. H. Lee, A. Iyo, T. Ito, T. Kakeshita, H. Eisaki, and S. Uchida. Effect of Co Doping on the In-Plane Anisotropy in the Optical Spectrum of Underdoped $Ba(Fe_{1-x}Co_x)_2As_2$. *Phys. Rev. Lett.*, Vol. 109, p. 217003, Nov 2012.

[49] Shuai Jiang, H. S. Jeevan, Jinkui Dong, and P. Gegenwart. Thermopower as a Sensitive Probe of Electronic Nematicity in Iron Pnictides. *Phys. Rev. Lett.*, Vol. 110, p. 067001, Feb 2013.

[50] T-M Chuang, MP Allan, Jinho Lee, Yang Xie, Ni Ni, SLBud'ko, GS Boebinger, PC Canfield, JC Davis. Nematic Electronic Structure in the "Parent" State of the Iron-Based Superconductor $Ca(Fe_{1-x}Co_x)_2As_2$. *Science*, Vol. 327, No. 5962, pp. 181–184, 2010.

[51] M. P. Allan, T-M. Chuang, F. Massee, Yang Xie, Ni Ni, S. L. Bud'ko, G. S. Boebinger, Q. Wang, D. S. Dessau, P. C. Canfield, M. S. Golden, and J. C. Davis. Anisotropic impurity states, quasiparticle scattering and nematic transport in underdoped $Ca(Fe_{1-x}Co_x)_2As_2$. *Nature Physics*, Vol. 9, No. 4, pp. 220–224, 2013.

[52] EP Rosenthal, EF Andrade, CJ Arguello, RM Fernandes, LY Xing, XC Wang, CQ Jin, AJ Millis, and AN Pasupathy. Visualization of electron nematicity and unidirectional antiferroic fluctuations at high temperatures in NaFeAs. *Nature Physics*, Vol. 10, No. 3, pp. 225–232, 2014.

[53] Xingye Lu, JT Park, Rui Zhang, Huiqian Luo, Andriy H Nevidomskyy, Qimiao Si, and Pengcheng Dai. Nematic spin correlations in the tetragonal state of uniaxial-strained $BaFe_{2-x}Ni_xAs_2$. *Science*, Vol. 345, No. 6197, pp. 657–660, 2014.

[54] N Murai, T Fukuda, T Kobayashi, M Nakajima, H Uchiyama, D Ishikawa, S Tsutsui, H Nakamura, M Machida, S Miyasaka, et al. Effect of magnetism on lattice dynamics in $SrFe_2As_2$ as seen via high resolution inelastic x-ray scattering. *arXiv preprint arXiv:1510.05487*, 2015.

[55] S Kasahara, HJ Shi, K Hashimoto, S Tonegawa, Y Mizukami, T Shibauchi, K Sugimoto, T Fukuda, T Terashima, Andriy H Nevidomskyy, et al. Electronic nematicity above the structural and superconducting transition in $BaFe_2(As_{1-x}P_x)_2$. *Nature*, Vol. 486, No. 7403, pp. 382–385, 2012.

[56] Rafael M Fernandes and Jörg Schmalian. Manifestations of nematic degrees of freedom in the magnetic, elastic, and superconducting properties of the iron pnictides. *Superconductor Science and Technology*, Vol. 25, No. 8, p. 084005, 2012.

[57] ZP Yin, K Haule, and G Kotliar. Magnetism and charge dynamics in iron pnictides. *Nature physics*, Vol. 7, No. 4, pp. 294–297, 2011.

[58] D. N. Basov and T. Timusk. Electrodynamics of high-T_c superconductors. *Rev. Mod. Phys.*, Vol. 77, pp. 721–779, Aug 2005.

[59] D. N. Basov, Richard D. Averitt, Dirk van der Marel, Martin Dressel, and Kristjan Haule. Electrodynamics of correlated electron materials. *Rev. Mod. Phys.*, Vol. 83, pp. 471–541, Jun 2011.

[60] M. Nakajima, S. Ishida, K. Kihou, Y. Tomioka, T. Ito, Y. Yoshida, C. H. Lee, H. Kito, A. Iyo, H. Eisaki, K. M. Kojima, and S. Uchida. Evolution of the optical spectrum with doping in $Ba(Fe_{1-x}Co_x)_2As_2$. *Phys. Rev. B*, Vol. 81, p. 104528, Mar 2010.

[61] S. J. Moon, J. H. Shin, D. Parker, W. S. Choi, I. I. Mazin, Y. S. Lee, J. Y. Kim, N. H. Sung, B. K. Cho, S. H. Khim, J. S. Kim, K. H. Kim, and T. W. Noh. Dual character of magnetism in $EuFe_2As_2$: Optical spectroscopic and density-functional calculation study. *Phys. Rev. B*, Vol. 81, p. 205114, May 2010.

[62] Masamichi Nakajima, Shin-ichi Uchida, Kunihiro Kihou, Chul-Ho Lee, Akira Iyo, and Hiroshi Eisaki. Growth of $BaFe_2(As_{1-x}P_x)_2$ Single Crys-

tals ($0 \leq x \leq 1$) by Ba_2As_3/Ba_2P_3-Flux Method. *Journal of the Physical Society of Japan*, Vol. 81, No. 10, p. 104710, 2012.

[63] Kazuhiko Kuroki, Seiichiro Onari, Ryotaro Arita, Hidetomo Usui, Yukio Tanaka, Hiroshi Kontani, and Hideo Aoki. Unconventional Pairing Originating from the Disconnected Fermi Surfaces of Superconducting $LaFeAsO_{1-x}F_x$. *Phys. Rev. Lett.*, Vol. 101, p. 087004, Aug 2008.

[64] H. S. Jeevan, Deepa Kasinathan, Helge Rosner, and Philipp Gegenwart. Interplay of antiferromagnetism, ferromagnetism, and superconductivity in $EuFe_2(As_{1-x}P_x)_2$ single crystals. *Phys. Rev. B*, Vol. 83, p. 054511, Feb 2011.

[65] S. Kasahara, T. Shibauchi, K. Hashimoto, Y. Nakai, H. Ikeda, T. Terashima, and Y. Matsuda. Abrupt recovery of Fermi-liquid transport following the collapse of the c axis in $CaFe_2(As_{1-x}P_x)_2$ single crystals. *Phys. Rev. B*, Vol. 83, p. 060505, Feb 2011.

[66] H. Suzuki, T. Yoshida, S. Ideta, G. Shibata, K. Ishigami, T. Kadono, A. Fujimori, M. Hashimoto, D. H. Lu, Z.-X. Shen, K. Ono, E. Sakai, H. Kumigashira, M. Matsuo, and T. Sasagawa. Absence of superconductivity in the hole-doped Fe pnictide $Ba(Fe_{1-x}Mn_x)_2As_2$: Photoemissionand x-ray absorption spectroscopy studies. *Phys. Rev. B*, Vol. 88, p. 100501, Sep 2013.

[67] HL Shi, HX Yang, HF Tian, JB Lu, ZW Wang, YB Qin, YJ Song, and JQ Li. Structural properties and superconductivity of $SrFe_2As_{2-x}P_x$ ($0.0 \leqq x \leqq 1.0$) and $CaFe_2As_{2-y}P_y$ ($0.0 \leqq y \leqq 0.3$). *Journal of Physics: Condensed Matter*, Vol. 22, No. 12, p. 125702, 2010.

[68] S. Ishida, T. Liang, M. Nakajima, K. Kihou, C. H. Lee, A. Iyo, H. Eisaki, T. Kakeshita, T. Kida, M. Hagiwara, Y. Tomioka, T. Ito, and S. Uchida. Manifestations of multiple-carrier charge transport in the magnetostructurally ordered phase of $BaFe_2As_2$. *Phys. Rev. B*, Vol. 84, p. 184514, Nov 2011.

[69] R. M. Fernandes, M. G. Vavilov, and A. V. Chubukov. Enhancement of T_c by disorder in underdoped iron pnictide superconductors. *Phys. Rev. B*, Vol. 85, p. 140512, Apr 2012.

[70] M. Miyamoto, H. Mukuda, T. Kobayashi, M. Yashima, Y. Kitaoka, S. Miyasaka, and S. Tajima. NMR evidence for an intimate relationship between antiferromagnetic spin fluctuations and extended s-wave superconductivity in monocrystalline $SrFe_2(As_{1-x}P_x)_2$. *Phys. Rev. B*, Vol. 92, p. 125154, Sep 2015.

[71] T. Dulguun, H. Mukuda, T. Kobayashi, F. Engetsu, H. Kinouchi, M. Yashima, Y. Kitaoka, S. Miyasaka, and S. Tajima. Unconventional multiband superconductivity with nodes in single-crystalline $SrFe_2(As_{0.65}P_{0.35})_2$ as seen via ^{31}P NMR and specific heat. *Phys. Rev. B*, Vol. 85, p. 144515, Apr 2012.

[72] Lei Fang, Huiqian Luo, Peng Cheng, Zhaosheng Wang, Ying Jia, Gang Mu, Bing Shen, I. I. Mazin, Lei Shan, Cong Ren, and Hai-Hu Wen. Roles of multiband effects and electron-hole asymmetry in the superconductivity and normal-state properties of $Ba(Fe_{1-x}Co_x)_2As_2$. *Phys. Rev. B*, Vol. 80, p. 140508, Oct 2009.

[73] Marcin Matusiak, Zbigniew Bukowski, and Janusz Karpinski. Doping dependence of the Nernst effect in $Eu(Fe_{1-x}Co_x)_2As_2$: Departure from Dirac-fermion physics. *Phys. Rev. B*, Vol. 83, p. 224505, Jun 2011.

[74] Marcin Matusiak, Zbigniew Bukowski, and Janusz Karpinski. Nernst effect in single crystals of the pnictide superconductor $CaFe_{1.92}Co_{0.08}As_2$ and parent compound $CaFe_2As_2$. *Phys. Rev. B*, Vol. 81, p. 020510, Jan 2010.

[75] Takao Morinari, Eiji Kaneshita, and Takami Tohyama. Topological and Transport Properties of Dirac Fermions in an Antiferromagnetic Metallic Phase of Iron-Based Superconductors. *Phys. Rev. Lett.*, Vol. 105, p. 037203, Jul 2010.

[76] Mike Sutherland, D. J. Hills, B. S. Tan, M. M. Altarawneh, N. Harrison, J. Gillett, E. C. T. O'Farrell, T. M. Benseman, I. Kokanovic, P. Syers, J. R. Cooper, and Suchitra E. Sebastian. Evidence for Dirac nodes from quantum oscillations in $SrFe_2As_2$. *Phys. Rev. B*, Vol. 84, p. 180506, Nov 2011.

[77] L. Fanfarillo, E. Cappelluti, C. Castellani, and L. Benfatto. Unconventional Hall Effect in Pnictides from Interband Interactions. *Phys. Rev. Lett.*, Vol. 109, p. 096402, Aug 2012.

[78] J.-Q. Yan, A. Kreyssig, S. Nandi, N. Ni, S. L. Bud'ko, A. Kracher, R. J. McQueeney, R. W. McCallum, T. A. Lograsso, A. I. Goldman, and P. C. Canfield. Structural transition and anisotropic properties of single-crystalline $SrFe_2As_2$. *Phys. Rev. B*, Vol. 78, p. 024516, Jul 2008.

[79] Hisashi Kotegawa, Hitoshi Sugawara, and Hideki Tou. Abrupt emergence of pressure-induced superconductivity of 34 K in $SrFe_2As_2$: A resistivity study under pressure. *Journal of the Physical Society of Japan*, Vol. 78, No. 1, p. 013709, 2008.

[80] Kazuhiko Kuroki, Hidetomo Usui, Seiichiro Onari, Ryotaro Arita, and Hideo Aoki. Pnictogen height as a possible switch between high-T_c nodeless and low-T_c nodal pairings in the iron-based superconductors. *Phys. Rev. B*, Vol. 79, p. 224511, Jun 2009.

[81] K. Gofryk, A. B. Vorontsov, I. Vekhter, A. S. Sefat, T. Imai, E. D. Bauer, J. D. Thompson, and F. Ronning. Effect of annealing on the specific heat of $Ba(Fe_{1-x}Co_x)_2As_2$. *Phys. Rev. B*, Vol. 83, p. 064513, Feb 2011.

[82] Sergey L. Bud'ko, Ni Ni, and Paul C. Canfield. Jump in specific heat at the superconducting transition temperature in $Ba(Fe_{1-x}Co_x)_2As_2$ and $Ba(Fe_{1-x}Ni_x)_2As_2$ single crystals. *Phys. Rev. B*, Vol. 79, p. 220516, Jun 2009.

[83] Yuxing Wang, Bernard Revaz, Andreas Erb, and Alain Junod. Direct observation and anisotropy of the contribution of gap nodes in the low-temperature specific heat of $YBa_2Cu_3O_7$. *Phys. Rev. B*, Vol. 63, p. 094508, Feb 2001.

[84] J. S. Kim, P. J. Hirschfeld, G. R. Stewart, S. Kasahara, T. Shibauchi, T. Terashima, and Y. Matsuda. Specific heat versus field in the 30 K superconductor $BaFe_2(As_{0.7}P_{0.3})_2$. *Phys. Rev. B*, Vol. 81, p. 214507, Jun 2010.

[85] Yunkyu Bang. Volovik Effect in the $\pm s$-Wave State for the Iron-Based Superconductors. *Phys. Rev. Lett.*, Vol. 104, p. 217001, May 2010.

[86] J. Murphy, C. P. Strehlow, K. Cho, M. A. Tanatar, N. Salovich, R. W. Giannetta, T. Kobayashi, S. Miyasaka, S. Tajima, and R. Prozorov.

Nodal superconductivity in isovalently substituted $SrFe_2(As_{1-x}P_x)_2$ pnictide superconductor at the optimal doping $x = 0.35$. *Phys. Rev. B*, Vol. 87, p. 140505, Apr 2013.

[87] E. C. Blomberg, A. Kreyssig, M. A. Tanatar, R. M. Fernandes, M. G. Kim, A. Thaler, J. Schmalian, S. L. Bud'ko, P. C. Canfield, A. I. Goldman, and R. Prozorov. Effect of tensile stress on the in-plane resistivity anisotropy in $BaFe_2As_2$. *Phys. Rev. B*, Vol. 85, p. 144509, Apr 2012.

[88] M Yi, D H Lu, R G Moore, K Kihou, C-H Lee, A Iyo, H Eisaki, T Yoshida, A Fujimori, and Z-X Shen. Electronic reconstruction through the structural and magnetic transitions in detwinned NaFeAs. *New Journal of Physics*, Vol. 14, No. 7, p. 073019, 2012.

[89] Shuhua Liang, Gonzalo Alvarez, Cengiz Şen, Adriana Moreo, and Elbio Dagotto. Anisotropy of Electrical Transport in Pnictide Superconductors Studied Using Monte Carlo Simulations of the Spin-Fermion Model. *Phys. Rev. Lett.*, Vol. 109, p. 047001, Jul 2012.

[90] C.-C. Chen, J. Maciejko, A. P. Sorini, B. Moritz, R. R. P. Singh, and T. P. Devereaux. Orbital order and spontaneous orthorhombicity in iron pnictides. *Phys. Rev. B*, Vol. 82, p. 100504, Sep 2010.

[91] Xiaotian Zhang and Elbio Dagotto. Anisotropy of the optical conductivity of a pnictide superconductor from the undoped three-orbital Hubbard model. *Phys. Rev. B*, Vol. 84, p. 132505, Oct 2011.

[92] Weicheng Lv and Philip Phillips. Orbitally and magnetically induced anisotropy in iron-based superconductors. *Phys. Rev. B*, Vol. 84, p. 174512, Nov 2011.

[93] M. S. Laad and L. Craco. Theory of the unusual high-temperature anisotropic resistivity of underdoped iron arsenide superconductors: Evidence for an orbital nematic order. *Phys. Rev. B*, Vol. 84, p. 054530, Aug 2011.

[94] Shuhua Liang, Adriana Moreo, and Elbio Dagotto. Nematic State of Pnictides Stabilized by Interplay between Spin, Orbital, and Lattice Degrees of Freedom. *Phys. Rev. Lett.*, Vol. 111, p. 047004, Jul 2013.

[95] Hsueh-Hui Kuo, Jiun-Haw Chu, Scott C. Riggs, Leo Yu, Peter L. McMahon, Kristiaan De Greve, Yoshihisa Yamamoto, James G. Analytis, and Ian R. Fisher. Possible origin of the nonmonotonic doping dependence of the in-plane resistivity anisotropy of $Ba(Fe_{1-x}T_x)_2As_2$ (T = Co, Ni and Cu). *Phys. Rev. B*, Vol. 84, p. 054540, Aug 2011.

[96] S. Ishida, M. Nakajima, T. Liang, K. Kihou, C. H. Lee, A. Iyo, H. Eisaki, T. Kakeshita, Y. Tomioka, T. Ito, and S. Uchida. Anisotropy of the In-Plane Resistivity of Underdoped $Ba(Fe_{1-x}Co_x)_2As_2$ Superconductors Induced by Impurity Scattering in the Antiferromagnetic Orthorhombic Phase. *Phys. Rev. Lett.*, Vol. 110, p. 207001, May 2013.

[97] Shigeyuki Ishida, Masamichi Nakajima, Tian Liang, Kunihiro Kihou, Chul-Ho Lee, Akira Iyo, Hiroshi Eisaki, Teruhisa Kakeshita, Yasuhide Tomioka, Toshimitsu Ito, et al. Effect of Doping on the Magnetostructural Ordered Phase of Iron Arsenides: A Comparative Study of the Resistivity Anisotropy in Doped $BaFe_2As_2$ with Doping into Three Different Sites. *Journal of the American Chemical Society*, Vol. 135, No. 8, pp. 3158–3163, 2013.

[98] M Nakajima, T Liang, S Ishida, Y Tomioka, K Kihou, CH Lee, A Iyo, H Eisaki, T Kakeshita, T Ito, et al. Unprecedented anisotropic metallic state in undoped iron arsenide $BaFe_2As_2$ revealed by optical spectroscopy. *Proceedings of the National Academy of Sciences*, Vol. 108, No. 30, pp. 12238–12242, 2011.

[99] Maria N. Gastiasoro, P. J. Hirschfeld, and Brian M. Andersen. Origin of electronic dimers in the spin-density wave phase of Fe-based superconductors. *Phys. Rev. B*, Vol. 89, p. 100502, Mar 2014.

[100] Jian Kang and Zlatko Tešanović. Dimer impurity scattering, reconstructed Fermi-surface nesting, and density-wave diagnostics in iron pnictides. *Phys. Rev. B*, Vol. 85, p. 220507, Jun 2012.

[101] Yoshio Inoue, Youichi Yamakawa, and Hiroshi Kontani. Impurity-induced electronic nematic state and C_2-symmetric nanostructures in iron pnictide superconductors. *Phys. Rev. B*, Vol. 85, p. 224506, Jun 2012.

[102] J. J. Ying, X. F. Wang, T. Wu, Z. J. Xiang, R. H. Liu, Y. J. Yan, A. F. Wang, M. Zhang, G. J. Ye, P. Cheng, J. P. Hu, and X. H. Chen. Measurements of the Anisotropic In-Plane Resistivity of Underdoped FeAs-Based Pnictide Superconductors. *Phys. Rev. Lett.*, Vol. 107, p. 067001, Aug 2011.

[103] EC Blomberg, MA Tanatar, RM Fernandes, II Mazin, Bing Shen, Hai-Hu Wen, MD Johannes, J Schmalian, and R Prozorov. Sign-reversal of the in-plane resistivity anisotropy in hole-doped iron pnictides. *Nature communications*, Vol. 4, p. 1914, 2013.

[104] B. Valenzuela, E. Bascones, and M. J. Calderón. Conductivity Anisotropy in the Antiferromagnetic State of Iron Pnictides. *Phys. Rev. Lett.*, Vol. 105, p. 207202, Nov 2010.

[105] Koudai Sugimoto, Peter Prelovšek, Eiji Kaneshita, and Takami Tohyama. Memory function approach to in-plane anisotropic resistivity in the antiferromagnetic phase of iron arsenide superconductors. *Phys. Rev. B*, Vol. 90, p. 125157, Sep 2014.

[106] Rafael M. Fernandes, Elihu Abrahams, and Jörg Schmalian. Anisotropic In-Plane Resistivity in the Nematic Phase of the Iron Pnictides. *Phys. Rev. Lett.*, Vol. 107, p. 217002, Nov 2011.

[107] Maxim Breitkreiz, P. M. R. Brydon, and Carsten Timm. Resistive anisotropy due to spin-fluctuation scattering in the nematic phase of iron pnictides. *Phys. Rev. B*, Vol. 90, p. 121104, Sep 2014.

[108] Bing Shen, Huan Yang, Zhao-Sheng Wang, Fei Han, Bin Zeng, Lei Shan, Cong Ren, and Hai-Hu Wen. Transport properties and asymmetric scattering in $Ba_{1-x}K_xFe_2As_2$ single crystals. *Phys. Rev. B*, Vol. 84, p. 184512, Nov 2011.

[109] Kenya Ohgushi and Yoko Kiuchi. Doping dependence of hall coefficient and evolution of coherent electronic state in the normal state of the Fe-based superconductor $Ba_{1-x}K_xFe_2As_2$. *Phys. Rev. B*, Vol. 85, p. 064522, Feb 2012.

[110] F. Rullier-Albenque, D. Colson, A. Forget, and H. Alloul. Hall Effect and Resistivity Study of the Magnetic Transition, Carrier Content, and

Fermi-Liquid Behavior in $Ba(Fe_{1-x}Co_x)_2As_2$. *Phys. Rev. Lett.*, Vol. 103, p. 057001, Jul 2009.

[111] Maxim Breitkreiz, P. M. R. Brydon, and Carsten Timm. Transport anomalies due to anisotropic interband scattering. *Phys. Rev. B*, Vol. 88, p. 085103, Aug 2013.

[112] Y Texier, Y Laplace, P Mendels, JT Park, G Friemel, DL Sun, DS Inosov, CT Lin, and J Bobroff. Mn local moments prevent superconductivity in iron pnictides $Ba(Fe_{1-x}Mn_x)_2As_2$. *EPL (Europhysics Letters)*, Vol. 99, No. 1, p. 17002, 2012.

[113] Athena S. Sefat, David J. Singh, Lindsay H. VanBebber, Yurij Mozharivskyj, Michael A. McGuire, Rongying Jin, Brian C. Sales, Veerle Keppens, and David Mandrus. Absence of superconductivity in hole-doped $BaFe_{2-x}Cr_xAs_2$ single crystals. *Phys. Rev. B*, Vol. 79, p. 224524, Jun 2009.

[114] A. Thaler, H. Hodovanets, M. S. Torikachvili, S. Ran, A. Kracher, W. Straszheim, J. Q. Yan, E. Mun, and P. C. Canfield. Physical and magnetic properties of $Ba(Fe_{1-x}Mn_x)_2As_2$ single crystals. *Phys. Rev. B*, Vol. 84, p. 144528, Oct 2011.

[115] N. Ni, M. E. Tillman, J.-Q. Yan, A. Kracher, S. T. Hannahs, S. L. Bud'ko, and P. C. Canfield. Effects of Co substitution on thermodynamic and transport properties and anisotropic H_{c2} in $Ba(Fe_{1-x}Co_x)_2As_2$ single crystals. *Phys. Rev. B*, Vol. 78, p. 214515, Dec 2008.

[116] J. Q. Ma, X. G. Luo, P. Cheng, N. Zhu, D. Y. Liu, F. Chen, J. J. Ying, A. F. Wang, X. F. Lu, B. Lei, and X. H. Chen. Evolution of anisotropic in-plane resistivity with doping level in $Ca_{1-x}Na_xFe_2As_2$ single crystals. *Phys. Rev. B*, Vol. 89, p. 174512, May 2014.

[117] Maria N. Gastiasoro, I. Paul, Y. Wang, P. J. Hirschfeld, and Brian M. Andersen. Emergent Defect States as a Source of Resistivity Anisotropy in the Nematic Phase of Iron Pnictides. *Phys. Rev. Lett.*, Vol. 113, p. 127001, Sep 2014.

[118] A Charnukha. Optical conductivity of iron-based superconductors. *Journal of Physics: Condensed Matter*, Vol. 26, No. 25, p. 253203, 2014.

[119] W. Z. Hu, J. Dong, G. Li, Z. Li, P. Zheng, G. F. Chen, J. L. Luo, and N. L. Wang. Origin of the Spin Density Wave Instability in $A\mathrm{Fe_2As_2}$ ($A = \mathrm{Ba, Sr}$) as Revealed by Optical Spectroscopy. *Phys. Rev. Lett.*, Vol. 101, p. 257005, Dec 2008.

[120] M Nakajima, S Ishida, T Tanaka, K Kihou, Y Tomioka, T Saito, CH Lee, H Fukazawa, Y Kohori, T Kakeshita, et al. Normal-state charge dynamics in doped $\mathrm{BaFe_2As_2}$: Roles of doping and necessary ingredients for superconductivity. *Scientific reports*, Vol. 4, , 2014.

[121] A Charnukha, P Popovich, Y Matiks, DL Sun, CT Lin, AN Yaresko, B Keimer, and AV Boris. Superconductivity-induced optical anomaly in an iron arsenide. *Nature communications*, Vol. 2, p. 219, 2011.

[122] Y. M. Dai, B. Xu, B. Shen, H. H. Wen, J. P. Hu, X. G. Qiu, and R. P. S. M. Lobo. Pseudogap in underdoped $\mathrm{Ba_{1-x}K_xFe_2As_2}$ as seen via optical conductivity. *Phys. Rev. B*, Vol. 86, p. 100501, Sep 2012.

[123] G Grüner. The dynamics of charge-density waves. *Reviews of Modern Physics*, Vol. 60, No. 4, p. 1129, 1988.

[124] G Grüner. The dynamics of spin-density waves. *Reviews of modern physics*, Vol. 66, No. 1, p. 1, 1994.

[125] T. Dong, Z. G. Chen, R. H. Yuan, B. F. Hu, B. Cheng, and N. L. Wang. Formation of partial energy gap below the structural phase transition and the rare-earth element-substitution effect on infrared phonons in ReFeAsO (Re = La, Nd, and Sm). *Phys. Rev. B*, Vol. 82, p. 054522, Aug 2010.

[126] B. Valenzuela, M. J. Calderón, G. León, and E. Bascones. Optical conductivity and Raman scattering of iron superconductors. *Phys. Rev. B*, Vol. 87, p. 075136, Feb 2013.

[127] Takami Tohyama, Eiji Kaneshita, and Takao Morinari. Charge and spin dynamics in antiferromagnetic metallic phase of iron-based superconductors. *Journal of Physics and Chemistry of Solids*, Vol. 72, No. 5, pp. 315–318, 2011.

[128] S. Avci, O. Chmaissem, D. Y. Chung, S. Rosenkranz, E. A. Goremychkin, J. P. Castellan, I. S. Todorov, J. A. Schlueter, H. Claus, A. Daoud-Aladine, D. D. Khalyavin, M. G. Kanatzidis, and R. Osborn. Phase diagram of $Ba_{1-x}K_xFe_2As_2$. *Phys. Rev. B*, Vol. 85, p. 184507, May 2012.

[129] Ying Ran, Fa Wang, Hui Zhai, Ashvin Vishwanath, and Dung-Hai Lee. Nodal spin density wave and band topology of the FeAs-based materials. *Phys. Rev. B*, Vol. 79, p. 014505, Jan 2009.

[130] Vladimir Cvetkovic and Zlatko Tesanovic. Multiband magnetism and superconductivity in Fe-based compounds. *EPL (Europhysics Letters)*, Vol. 85, No. 3, p. 37002, 2009.

[131] Qimiao Si and Elihu Abrahams. Strong Correlations and Magnetic Frustration in the High T_c Iron Pnictides. *Phys. Rev. Lett.*, Vol. 101, p. 076401, Aug 2008.

[132] T. Yildirim. Origin of the 150-K Anomaly in LaFeAsO: Competing Antiferromagnetic Interactions, Frustration, and a Structural Phase Transition. *Phys. Rev. Lett.*, Vol. 101, p. 057010, Aug 2008.

[133] ZP Yin, K Haule, and G Kotliar. Kinetic frustration and the nature of the magnetic and paramagnetic states in iron pnictides and iron chalcogenides. *Nature materials*, Vol. 10, No. 12, pp. 932–935, 2011.

[134] I. Eremin and A. V. Chubukov. Magnetic degeneracy and hidden metallicity of the spin-density-wave state in ferropnictides. *Phys. Rev. B*, Vol. 81, p. 024511, Jan 2010.

[135] Xiaoyu Wang and Rafael M. Fernandes. Impact of local-moment fluctuations on the magnetic degeneracy of iron arsenide superconductors. *Phys. Rev. B*, Vol. 89, p. 144502, Apr 2014.

[136] Maria N. Gastiasoro and Brian M. Andersen. Enhancement of Magnetic Stripe Order in Iron-Pnictide Superconductors from the Interaction between Conduction Electrons and Magnetic Impurities. *Phys. Rev. Lett.*, Vol. 113, p. 067002, Aug 2014.

[137] A. Antal, T. Knoblauch, Y. Singh, P. Gegenwart, D. Wu, and M. Dressel. Optical properties of the iron-pnictide analog $BaMn_2As_2$. *Phys. Rev. B*, Vol. 86, p. 014506, Jul 2012.

[138] M. J. Calderón, L. de' Medici, B. Valenzuela, and E. Bascones. Correlation, doping, and interband effects on the optical conductivity of iron superconductors. *Phys. Rev. B*, Vol. 90, p. 115128, Sep 2014.

[139] Masamichi Nakajima, Shigeyuki Ishida, Takahide Tanaka, Kunihiro Kihou, Yasuhide Tomioka, Taku Saito, Chul-Ho Lee, Hideto Fukazawa, Yoh Kohori, Teruhisa Kakeshita, et al. Strong Electronic Correlations in Iron Pnictides: Comparison of Optical Spectra for $BaFe_2As_2$-Related Compounds. *Journal of the Physical Society of Japan*, Vol. 83, No. 10, p. 104703, 2014.

[140] Tae Wan Kim, S Donovan, G Grüner, and A Philipp. Charge-density-wave dynamics in $(Ta_{1-x}Nb_xSe_4)_2I$ alloys. *Physical Review B*, Vol. 43, No. 8, p. 6315, 1991.

[141] DN Basov, B Dabrowski, and T Timusk. Infrared probe of transition from superconductor to nonmetal in $YBa_2(Cu_{1-x}Zn_x)_4O_8$. *Physical review letters*, Vol. 81, No. 10, p. 2132, 1998.

[142] D. N. Basov, A. V. Puchkov, R. A. Hughes, T. Strach, J. Preston, T. Timusk, D. A. Bonn, R. Liang, and W. N. Hardy. Disorder and superconducting-state conductivity of single crystals of $YBa_2Cu_3O_{6.95}$. *Phys. Rev. B*, Vol. 49, pp. 12165–12169, May 1994.

[143] Jun Kondo. Resistance minimum in dilute magnetic alloys. *Progress of theoretical physics*, Vol. 32, No. 1, pp. 37–49, 1964.

[144] H. Okamura, M. Matsunami, T. Inaoka, T. Nanba, S. Kimura, F. Iga, S. Hiura, J. Klijn, and T. Takabatake. Optical conductivity of $Yb_{1-x}Lu_xB_{12}$: Energy gap and mid-infrared peak in diluted Kondo semiconductors. *Phys. Rev. B*, Vol. 62, pp. R13265–R13269, Nov 2000.

[145] J Sichelschmidt, A Herzog, H S Jeevan, C Geibel, F Steglich, T Iizuka, and S Kimura. Far-infrared optical conductivity of $CeCu_2Si_2$. *Journal of Physics: Condensed Matter*, Vol. 25, No. 6, p. 065602, 2013.

[146] Antoine Georges, Luca de' Medici, and Jernej Mravlje. *Strong Correlations from Hund's Coupling*, Vol. 4 of *Annual Review of Condensed Matter Physics*. 2013.

[147] Rafael M. Fernandes and Andrew J. Millis. Suppression of Superconductivity by Néel-Type Magnetic Fluctuations in the Iron Pnictides. *Phys. Rev. Lett.*, Vol. 110, p. 117004, Mar 2013.

Publication list

1. Jasmin Jandke, Petra Wild, Michael Schackert, Shigemasa Suga, **Tatsuya Kobayashi**, Shigeki Miyasaka, Setsuko Tajima, Wulf Wulfhekel, **Scanning Tunneling Spectroscopy on $SrFe_2(As_{1-x}P_x)_2$**, arxiv:1512.05254.

2. E. Uykur, **T. Kobayashi**, W. Hirata, S. Miyasaka, S. Tajima, C. A. Kuntscher, **Optical Study of $BaFe_2As_2$ under pressure: Coexistence of spin-density-wave gap and superconductivity**, *Phys. Rev. B* 92, 245133 (2015).

3. N. Murai, T. Fukuda, **T. Kobayashi**, M. Nakajima, H. Uchiyama, D. Ishikawa, S. Tsutsui, H. Nakamura, M. Machida, S. Miyasaka, S. Tajima, A. Q. R. Baron, **Effect of magnetism on lattice dynamics in $SrFe_2As_2$ using high-resolution inelastic x-ray scattering**, *Phys. Rev. B* 93, 020301(R) (2016) (Editors' Suggestion).

4. M. Miyamoto, H. Mukuda, **T. Kobayashi**, M. Yashima, Y. Kitaoka, S. Miyasaka, S. Tajima, **NMR evidence for an intimate relationship between antiferromagnetic spin fluctuations and extended s-wave superconductivity in mono-crystalline $SrFe_2(As_{1-x}P_x)_2$**, *Physical Review B* 92, 125154 (2015).

5. **Tatsuya Kobayashi**, Kiyohisa Tanaka, Shigeki Miyasaka, Setsuko Tajima, **Importance of Fermi Surface Topology for In-Plane Resistivity Anisotropy in Hole- and Electron-Doped $Ba(Fe_{1-x}TM_x)_2As_2$ (TM=Cr, Mn and Co)**, *Journal of the Physical Society of Japan* 84, 094707 (2015).

6. C. P. Strehlow, M. Kończykowski, J. A. Murphy, S. Teknowijoyo, K. Cho, M. A. Tanatar, **T. Kobayashi**, S. Miyasaka, S. Tajima, and R. Prozorov, **Comparative study of the effects of electron irradiation and natural disorder in single crystals of $SrFe_2(As_{1-x}P_x)_2$ superconductor (x=0.35)**, *Physical Review B* 90, 020508(R) (2014).

7. H. Suzuki, **T. Kobayashi**, S. Miyasaka, T. Yoshida, K. Okazaki, L. C. C. Ambolode, II, S. Ideta, M. Yi, M. Hashimoto, D. H. Lu, Z.-X. Shen, K. Ono, H. Kumigashira, S. Tajima, and A. Fujimori, **Strongly three-dimensional electronic structure and Fermi surfaces of $SrFe_2(As_{0.65}P_{0.35})_2$: Comparison with $BaFe_2(As_{1-x}P_x)_2$**, *Physical Review B* 89, 184513 (2014).

8. **T. Kobayashi**, S. Miyasaka, S. Tajima, and N. Chikumoto, **Electronic Phase Diagram of $SrFe_2(As_{1-x}P_x)_2$: Effect of Structural Dimensionality**, *Journal of the Physical Society of Japan* 83 104702 (2014).

9. S. Miyasaka, A. Takemori, **T. Kobayashi**, S. Suzuki, S. Saijo, S. Tajima, **Two Fermi surface states and two T_c-rising mechanisms revealed by transport properties in $RFeP_{1-x}As_xO_{0.9}F_{0.1}$ (R=La, Pr and Nd)**, *Journal of the Physical Society of Japan* 82, 124706 (2013).

10. **T. Kobayashi**, S. Miyasaka, S. Tajima, T. Nakano, Y. Nozue, N. Chikumoto, H. Nakao, R. Kumai, and Y. Murakami, **Change of electronic state and crystal structure by postannealing in superconducting $SrFe_2(As_{0.65}P_{0.35})_2$**, *Physical Review B* 87, 174520 (2013).

11. J. Murphy, C. P. Strehlow, K. Cho, M. A. Tanatar, N. Salovich, R. W. Giannetta, **T. Kobayashi**, S. Miyasaka, S. Tajima, R. Prozorov, **Nodal superconductivity in isovalently substituted $SrFe_2(As_{1-x}P_x)_2$ pnictide superconductor at the optimal doping x=0.35**, *Physical Review B* 87, 140505(R) (2013).

12. M. Ikeda, M. Hagiwara, **T. Kobayashi**, W. Hirata, S. Miyasaka, S. Tajima, **Multi-frequency ESR in $EuFe_2As_2$**, *Journal of the Korean Physical Society* 62, 2007 (2013).

13. T. Kida, **T. Kobayashi**, S. Miyasaka, S. Tajima, M. Hagiwara, **Transport properties of the iron-based superconductor $SrFe_2(As,P)_2$ in high magnetic field**, *Journal of Low Temperature Physics* 170, 346 (2013).

14. S. Yeninas, M. A. Tanatar, C. Strehlow, J. Murphy, O. E. Ayala-Valenzucla, R. D. McDonald, U. Welp, W. K. Kwok, **T. Kobayashi**, S. Miyasaka, S. Tajima, R. Prozorov, **Upper critical field of isovalent substituted $SrFe_2(As_{1-x}P_x)_2$**, *Physical Review B*, 87, 094503 (2013).

15. T. Dulguun, H. Mukuda, **T. Kobayashi**, F. Engetsu, H. Kinouchi, M. Yashima, Y. Kitaoka, S. Miyasaka, S. Tajima, **Unconventional superconductivity with nodes in single-crystalline $SrFe_2(As_{0.65}P_{0.35})_2$**

as seen via ^{31}P-NMR study and specific heat, *Physical Review B* 85, 144515 (2012).

16. **T. Kobayashi**, S. Miyasaka, S. Tajima, **Single crystal growth and physical properties in $SrFe_2(As_{1-x}P_x)_2$**, *Journal of the Physical Society of Japan Supplement B* 81, SB045 (2012).

List of International Conferences

1. **T. Kobayashi**, M. Nakajima, S. Miyasaka, S. Tajima, **Doping Evolution of the Optical Spectrum in Ba($Fe_{1-x}TM_x$)$_2As_2$ (TM=Cr, Mn, and Co)**, The 28th International Superconductivity Symposium (ISS2015), Tokyo, Japan, Nov. 16-18, 2015 (Oral).

2. **T. Kobayashi**, K. Tanaka, S. Miyasaka, S. Tajima, **Reversal Anisotropy of In-plane Resistivity in Hole Doped Ba($Fe_{1-x}TM_x$)$_2As_2$ (TM=Mn, Cr)**, The 27th International Superconductivity Symposium (ISS2014), Tokyo, Japan, Nov. 25-27, 2014 (Poster).

3. **T. Kobayashi**, T. Yamada, K. Tanaka, S. Miyasaka, S. Tajima, **Anisotropy reversal of in-plane in hole doped iron pnictide Ba($Fe_{1-x}TM_x$)$_2As_2$ (TM=Mn, Cr)**, APS March Meeting 2014, Denver, USA, 3-7 March 2014 (Oral).

4. **T. Kobayashi**, T. Yamada, K. Tanaka, S. Miyasaka, S. Tajima, **Reversal Resistivity Anisotropy in Hole Doped Iron Pnictide Ba($Fe_{1-x}TM_x$)$_2As_2$ (TM=Mn, Cr)**, 1st KANSAI Nanoscience and Nanotechnology International Symposium, Osaka, Japan, 3-4 Feb. 2014 (Poster).

5. **T. Kobayashi**, S. Miyasaka, S. Tajima, N. Chikumoto, H. Nakao, R. Kumai, Y. Murakami, **The annealing effect on electronic state and crystal structure in $SrFe_2(As_{1-x}P_x)_2$ ($0 \leq x \leq 1$)**, The International Conference on Strongly Correlated Electron Systems, Tokyo, Japan, Aug. 5-9, 2013 (Poster).

6. **T. Kobayashi**, S. Miyasaka, S. Tajima, N. Chikumoto, H. Nakao, R. Kumai, Y. Murakami, **Annealing effect on $SrFe_2(As_{1-x}P_x)_2$**, A3 Foresight Program of "Joint Research on Novel Properties of Complex Oxides", Tokyo, Japan, March 14-16, 2013 (Poster).

7. **T. Kobayashi**, S. Miyasaka, S. Tajima, N. Chikumoto, H. Nakao, R. Kumai, Y. Murakami, **Electronic and crystal change by post annealing in the superconducting $SrFe_2(As_{0.65}P_{0.35})_2$**, IRON-SEA third meeting, Osaka, Japan, March 5-6, 2013 (Poster).

8. **T. Kobayashi**, S. Miyasaka, S. Tajima, **Nodal superconducting gap behavior in $SrFe_2$(As,P)$_2$ revealed by specific heat measurement**, 25th International Symposium on Superconductivity (ISS2012), Tokyo, Japan, Dec. 3-5, 2012, (Poster).

9. **T. Kobayashi**, S. Miyasaka, S. Tajima, **Nodal superconducting gap behavior of specific heat in $SrFe_2(As,P)_2$ single crystal**, The 2nd Osaka University and University of Groningen collaboration symposium "Particle & condensed matter physics: New challenges and opportunities", Osaka, Japan, Nov. 26-28, 2012 (Poster).

10. **T. Kobayashi**, S. Miyasaka and S. Tajima, **Single crystal growth and physical properties of $SrFe_2(As_{1-x}P_x)_2$**, Int. Workshop on Heavy Fermions, Nov.23-26, 2011, Osaka (Poster).

Acknowledgement

First and foremost, I would like to express my sincerest gratitude to Professor S. Tajima, for her guidance, discussion, suggesstion, support, and patience throughout this research.

I thank Professor S. Miyasaka for his guidence, discussion, suggetion, and encouragemnet in the couse of this work.

I also want to thank Professor T. Masui, Professor K. Tanaka, and Professor M. Nakajima for their experimental support and discussion.

I would like to appreciate the following people: Professor N. Chikumoto (EPMA measurement), Professor H. Mukuda and Professor Y. Kitaoka (NMR measurement), Professor T. Nakano and Professor Y. Nozue (Specific heat measurement), Professor T. Kida and Professor M. Hagiwara (High magnetic field measurement), Professor A. Fujimori and Mr. H. Suzuki (Photoemission measurement), Professor Y. Murakami, Professor R. Kumai, Professor H. Nakao, and Professor Y. Wakabayashi (X-ray diffraction measurement), Professor S. Suga (STM measurement), Professor T. Tohyama and Dr. K. Sugimoto (Theoretical discussion), Professor M. Ashida and Professor M. Ichimiya (SEM-EDX measurement), Professor R. Prozorov (Penetration depth measurement),

I thank all the the member of Tajima group for miscellaneous things. Particularly, I am grateful to W. Hirata who taught me everything from the basics.

Finally, I would like to express special gratitude to my dear family for their full trusts on my decisions and support for years.